UC Berkeley
UC Berkeley Previously Published Works

Title

Precipitation Estimates and Orographic Gradients Using Snow, Temperature, and Humidity Measurements From a Wireless-Sensor Network

Permalink

https://escholarship.org/uc/item/53f2s348

Journal

Water Resources Research, 58(5)

ISSN

0043-1397

Authors

Cui, Guotao
Rice, Robert
Avanzi, Francesco
et al.

Publication Date

2022-05-01

DOI

10.1029/2021wr029954

Peer reviewed

Precipitation estimates and orographic gradients using snow, temperature, and humidity measurements from a wireless-sensor network

Guotao Cui[1,*], Robert Rice[1], Francesco Avanzi[2,3], Peter Hartsough[4], Weichao Guo[1],
Michael Anderson[5], Martha Conklin[1], Roger Bales[1,2]

1 Sierra Nevada Research Institute and School of Engineering, University of California, Merced, Merced, California, USA
2 Department of Civil and Environmental Engineering, University of California, Berkeley, Berkeley, California, USA
3 CIMA Research Foundation, Savona, Italy
4 Department of Land, Air, and Water Resources, University of California Davis, Davis, California, USA
5 California Department of Water Resources, Sacramento, California, USA
* Corresponding author: gcui3@ucmerced.edu

Key Points

- Blending spatial snow data from a ground network with gauge precipitation and atmospheric moisture improves mountain rain and snow estimates.
- The blending approach better represented orographic precipitation gradients, compared to gauge-based results.
- The blending approach performed well in snow-dominated elevations during heavy events related to atmospheric rivers and Sierra barrier jets.

Abstract

This study reports on a blending approach using snowpack measurements from a wireless-sensor network, gauge precipitation, and atmospheric-moisture data to estimate mountain precipitation amount and phase. We applied the approach in California's American River basin, using dense measurements from a network consisting of over 130 sensor nodes distributed across the upper, more snow-dominated part of the basin ($\geq$ 1500 m elevation). Analysis of 60 precipitation events in water years 2014-2017 showed that the approach provides estimates of precipitation and orographic enhancement that reduce uncertainty from apparent snow undercatch by limited gauges. This approach also infers total precipitation based on snow measurements during rain-on-snow events. The sensor network and blending approach yielded median upper-basin Orographic Precipitation Gradients (OPGs) of 0.57 km^{-1}, smaller than the also-positive lower-basin (< 1500 m) medians OPGs from precipitation gauges and a gauge-based gridded dataset of 1.23 and 1.00 km^{-1}, respectively. However, during 73% of the events, both gauges and the gridded product showed negative OPGs in the upper basin, inconsistent with typically positive values from the distributed sensor network. Upper-basin OPGs from gauges and the gridded product were more negative (p-values < 0.03) during heavy events related to atmospheric rivers and Sierra barrier jets than during milder events, revealing the challenges for gauges to reliably measure precipitation from large moisture transport by strong winds. In snow-dominated headwater areas, precipitation from the blending approach is recommended as being more accurate for decision support, providing critical rain-versus-snow amounts and complementing precipitation-gauge data.

Keywords: Orographic Precipitation; Wireless-Sensor Network; Snow; Precipitation Phase; Rain-Snow-Transition Zone

1 Introduction

Mixed-phase precipitation in mountainous regions has large temporal and spatial variability (Buytaert et al., 2006; Costa-Cabral et al., 2013); and in comparatively warm environments like the Sierra Nevada, solid precipitation amounts (i.e. snowfall) are sensitive to small elevation-dependent temperature changes. Accurate estimates of precipitation partitioning into rain and snow are crucial as a primary input for hydrologic predictions and process studies (Henn et al., 2018; Morin et al., 2006; Sharma et al., 2012). This is because the amount and spatial pattern of mixed-phase winter precipitation in mountainous regions, where snowfall can account for a considerable portion of annual precipitation, play a crucial role in determining local-to-regional water supply and flood risk. For example, winter precipitation combined with snowpack storage in the Sierra Nevada provides the major water source for urban, irrigation, hydroelectric, and ecosystem uses in California (Bales et al., 2006; Pandey et al., 1999), where its Mediterranean climate leads to wet winters and dry summers. Besides the sparse

availability (Avanzi et al., 2021), maintenance, and representativeness issues of precipitation gauges in high-elevation regions, the systematic bias introduced by wind-induced undercatch is also a considerable source of uncertainty (Bales et al., 2009; Grossi et al., 2017; Stisen et al., 2012; Strangeways, 1996; Yang et al., 1999). Snowfall is particularly challenging to measure (Yang et al., 2005), with bias frequently ranging from 20% to 50% (Rasmussen et al., 2012). More accurate, reliable estimates of mixed-phase precipitation in mountainous regions are needed at the scale of water-resources decision making and management – the watershed scale.

Gridded precipitation datasets at various spatial and temporal resolutions are currently available, such as the Parameter-elevation Relationships on Independent Slopes Model (PRISM, 800-m spatial resolution and daily temporal resolution; Daly et al., 2008), the Daymet (1-km daily resolution; Thornton et al., 1997), and the North American Land Data Assimilation System project, Phase 2 (NLDAS-2, ~12-km hourly resolution; Cosgrove et al., 2003). Gridded reanalysis datasets are typically derived through spatial

interpolation of gauge measurements. These gridded precipitation data often include elevation adjustments and corrections for complex orographic effects (Henn et al., 2018). However, the interpolation and extrapolation to high elevations come with uncertainty in the gridded data, as gauge density and thus accuracy decreases in higher-elevation mountain areas with complex terrain (Hofstra et al., 2009). Moreover, the systematic bias from undercatch in precipitation gauges is generally not accounted for before interpolating to gridded products (Adam & Lettenmaier, 2003), and these biases can be carried through to hydrologic studies using gridded products as model inputs.

As direct measurements of precipitation in complex terrain remain problematic, mountain precipitation can be more comprehensively assessed using multiple types of measurements such as radar, streamflow, and snow (Lundquist et al., 2019). Much effort has been devoted to applying ground-based observations to indirectly estimate precipitation. Doppler radars in the U.S. have been upgraded to dual-polarization radars and provide improved Quantitative Precipitation Estimates (QPEs) based on reflectivity, differential reflectivity, and specific differential phase, compared to conventional radars (Cifelli et al., 2011; Cocks et al., 2019; Gourley et al., 2009; Seo et al., 2015; J. Zhang et al., 2020). However, radar observations suffer from gaps in reflectivity data at the near-surface, and terrain "gaps" due to line-of-sight restrictions, and does not provide direct precipitation at ground level (Cocks et al., 2019; Dai et al., 2019; Krajewski et al., 2010; Vignal et al., 2000; Westrick et al., 1999).

Ground snow measurements are valuable for assessing precipitation. Winter solid precipitation can be estimated based on snow-depth increment, avoiding the undercatch problem from precipitation gauges (e.g. Mair et al., 2016). However, single-site investigations in complex topography do not provide a basin-scale assessment of precipitation. Building upon Snow Water Equivalent (SWE) measurements, Lundquist et al. (2015) compared precipitation estimates from 125 snow pillows in California's Sierra Nevada to a gridded dataset based on gauge data and PRISM climatology, and reported reasonable agreement, with a median difference of ±10% on an annual scale. However, underestimates from the gridded dataset could exceed 50% for individual storms.

Airborne lidar has been used to examine precipitation patterns both for individual events (Behrangi et al., 2018a; Brandt et al., 2020) and seasonal accumulation (Kirchner et al., 2014). The Airborne Snow Observatory (ASO) provides gridded (50 m) snow depth and SWE using scanning lidar, imaging spectrometer, and modeled snow density (Painter et al., 2016). Using the ASO data in the Tuolumne basin, Brandt et al. (2020) quantified the spatial variability of solid precipitation during a snow storm before and after lidar flights, and Behrangi et al. (2018a) evaluated precipitation products in a cold month bracketed by two flights. A high-resolution (90 m) snow product from SWE reanalysis (Margulis et al., 2016) was used to investigate the orographic gradients of cumulative snowfall in the Sierra Nevada (Huning & Margulis, 2017, 2018). Although snow-product-based solid precipitation is

valuable and provides insight, it does not directly address the pressing challenge of estimating total or liquid precipitation.

The precipitation gradient along elevation in mountains, i.e. Orographic Precipitation Gradient (OPG), is of great importance for hydrologic modeling and forecasting. For example, it is required as a key input for the Precipitation-Runoff Modeling System (PRMS), the Soil Water Assessment Tool (SWAT), and glacio-hydrologic models (Fontaine et al., 2002; Immerzeel et al., 2014; MacDougall et al., 2011; Markstrom et al., 2015; Wang et al., 2018). Avanzi et al. (2021) also showed that OPGs from snow-course data in the Western European Alps can improve snow-hydrologic predictions. However, the OPGs in model settings are often treated as constant parameters at annual or monthly timescales (Fontaine et al., 2002; Immerzeel et al., 2014; Markstrom et al., 2015), which may not represent precipitation changes along elevation for extreme-precipitation events. This will likely result in biased runoff forecasts.

Precipitation is dominated and modified by a number of atmospheric processes. For the complex terrain of California's northern Sierra Nevada, Atmospheric Rivers (ARs) and Sierra Barrier Jets (SBJs) can lead to extreme orographic precipitation when landfalling ARs are forced atop of a south-southeasterly SBJ (Ralph et al., 2016). The water-vapor flux transported by wintertime ARs towards west-facing slopes of the northern Sierra Nevada leads to more orographic precipitation (Smith et al., 2010). By investigating average water-year precipitation, Lundquist et al. (2010) found that the OPG is greater with lower SBJ heights and stronger westerly winds. Moisture and wind are the two basic drivers of orographic precipitation (Smith & Barstad, 2004). Using a snow reanalysis dataset (Margulis et al., 2016), Integrated water-Vapor Transport (IVT), and zonal winds at 700hPa, Huning & Margulis (2018) investigated the OPG climatology of solid precipitation across the Sierra Nevada. Yet from a hydrologic perspective, the critical OPGs of solid, liquid, and total precipitation during events associated with the ARs and SBJs have not been studied.

Spatially distributed clusters of wireless-sensor nodes in the Sierra Nevada have been shown to reliably and cost-effectively provide dense, spatially representative, hydrologic measurements that can inform real-time decision making (Brun-Laguna et al., 2016; Cui et al., 2020; Malek et al., 2017, 2019; Welch et al., 2013; Zhang et al., 2017a, 2017b; Z. Zhang et al., 2020). Previous work (Zhang et al., 2017a) using sensor clusters in the American River basin tested precipitation estimates for Water Year 2014 (WY, October 1, 2013-September 30, 2014) based on snow-depth increments from the sensors plus estimated snowpack density, and found positive precipitation lapse rates (i.e. the rate of precipitation change with elevation) above 1500-m elevation. The spatial heterogeneity of precipitation was better represented by the wireless sensors than by the limited operational observations (Zhang et al., 2017a; Zheng et al., 2018). While the potential of precipitation inferred from wireless-sensor snow measurements was shown, liquid precipitation during rainfall days was not included in the previous study. Total and

partitioned precipitation (i.e. solid and liquid precipitation) remained uncertain in extensive, mixed rain-snow regions.

In this study, we estimated precipitation amounts (including partitioned solid and liquid precipitation) in mixed rain-snow mountain regions, using rich snow measurements and other on-the-ground data from a basin-scale wireless-sensor network. The specific objectives of this study were to: i) develop a method that blends snowpack measurements from a distributed-sensor network, gauge precipitation, and atmospheric-moisture data to estimate precipitation in a mountain basin, ii) investigate OPGs across the basin at both precipitation-event and annual time scales, with specific attention given to heavy events associated with Atmospheric Rivers and Sierra Barrier Jets, and iii) evaluate the consistency and uncertainty of precipitation estimates and OPGs from wireless-sensor data, precipitation gauges, gridded gauge-based precipitation data, snow reanalysis data, and radar-precipitation data. Here we tested the hypothesis that blending snow data with gauge-precipitation data in mountains with a fluctuating rain-snow transition zone can improve both event and annual precipitation estimates, with OPGs different from those based on gauges.

2 Data and methods

Our WY 2014-17 study period corresponds to the years of operation of a dense research network of wireless sensors, which included two drought years that for the northern Sierra Nevada had 62% (2014) and 74% (2015) of the 100-year average precipitation, a near-average year that had 115% of average precipitation (2016), and the wettest year on record (2017) that saw 189% of average precipitation. WY2015 was also especially warm as well as dry, with only 5% of the historical April 1 average snowpack. The other 3 years were also relatively warm, with the wet WY2017 having 159% of the historical April 1 average snowpack. In addition to data from the research network, we used in situ snow and precipitation from operational networks, two gridded precipitation datasets, a snow reanalysis dataset, and atmospheric data.

This study developed a new method to estimate total and solid versus liquid precipitation based on the ground measurements from the wireless sensor network, as well as incorporating gauge data and atmospheric moisture through a random-forest model. Precipitation in the American River basin was estimated for 60 individual events in WY2014-2017 (Table S1). Each was classified based on the occurrence of AR and SBJ, and we also investigated precipitation amounts and OPGs at an aggregated-event scale.

2.1 Study area

The study area is the American River basin located on the western slope of the Sierra Nevada (i.e. west of the Sierra Nevada crest, Figure 1). This basin has an area of 6710 km^2, and an elevation high of 3090 m. Basin headwaters flow through three river forks to Folsom reservoir – key for municipal water supplies, downstream agriculture, power generation, aquatic ecosystems, and flood protection (Woldemichael et al., 2012). Its Mediterranean-type climate is

characterized by a wet winter and early spring with little precipitation during summer. The average historical snow line is 1500 m elevation (Raleigh & Lundquist, 2012; Welch et al., 2013). This study refers to the upper American River basin as the area with elevation $\geq$ 1500 m (2120 km^2), and the lower basin as that below 1500 m (4590 km^2).

2.2 Wireless sensor network

The research network consists of 13 wireless sensor clusters (Figure 1 and Table 1), which were deployed across the upper, seasonally snow-covered part of the American River basin. The network covers the basin from 1510 to 2723 m elevation. Above the highest SCN cluster, there is 0.6% of the basin area with an average slope of 17.6° (Figure S1). Each cluster comprises 10 wirelessly connected sensor nodes strategically placed within a 1-km^2 area (Zhang et al., 2017b). The sensors were optimized to represent basin-wide snowpack and to encompass the variability of landscape attributes, e.g. elevation, canopy cover, slope, and aspect, that affect snow accumulation and melt (Welch et al., 2013; Zhang et al., 2017a, 2017b).

These spatially distributed nodes (Figure S2) measured air temperature & relative humidity (Sensirion SHT-15), snow depth (Judd ultrasonic depth sensor), soil moisture (Decagon GS3), and solar radiation (Hukseflux LP02) at 15-min intervals (Zhang et al., 2017b). The 15-min distance-to-ground raw data (data processing Level 0) from Judd ultrasonic sensors had noisy jumps and missing values (Figure S3), which averaged 20% of the entire data across all nodes in WY2017, but can be up to 70% for damaged nodes (e.g. Judd sensor at node 8 of Schneiders buried by snow, Figure S3b). Raw data were then processed to Level 1 snow-depth data (Bales et al., 2018, 2020; Roche et al., 2019; Zhang et al., 2017a), providing relatively reliable measurements with an average of 15% missing data during precipitation days (8%, 19%, 18%, and 13% for WY2014-2017, respectively; Figure S4). After further processing and gap filling, the continuous, daily snow-depth data (Level 2) offered dense, valuable ground information for precipitation estimation. For example, within-cluster snow-depth variations (Figure S5) were shown by the sensor-network data. The maximum difference of snow depth across the 10 sensor nodes in the CAP cluster was as much as 162 cm in WY2017 (Figure S5d). The sensor data used in this study can be obtained at https://doi.org/10.6071/M39Q2V (Bales et al., 2020).

2.3 In situ precipitation and snow data

Precipitation and snow data from in situ operational stations within the American River basin or nearby (Figure 1 and Table 2) were acquired from the California Data Exchange Center (CDEC, http://cdec.water.ca.gov). SWE was observed by 14 snow pillows at operational stations in the upper basin. Solid precipitation from each pillow was estimated by daily SWE increment. Precipitation data were collected from 41 gauges ranging from 8 to 2546 m elevation, including 23 gauges in the lower and 18 in the upper basin. All SWE and precipitation data were subjected to quality control to remove anomalies and spurious fluctuations by applying a moving-median-based method and manual check. Daily precipitation was calculated

as the difference between the last hourly accumulated precipitation on consecutive days. At 15 sites precipitation was recorded by tipping-bucket rain gauges (Table 2). Ten out of 41 sites had measurements of wind speed and direction, and we adjusted daily precipitation from these gauges for wind-induced undercatch following the procedure of Yang et al. (1998). However, undercatch may also occur due to solid precipitation removed by wind and blockage of gauge orifice (Kochendorfer et al., 2020; Rasmussen et al., 2012). The wind-induced undercatch was more significant during snowfall (Figure S6), as also indicated by the cumulative solid precipitation from snow pillows being greater than or close to cumulative precipitation from the four gauges at higher-elevation sites, after accounting for early season rainfall (Figure S7). The annual undercatch amounts of precipitation from gauges were estimated by the difference from raw precipitation data to either wind-adjusted precipitation or solid precipitation from nearby snow pillows. Precipitation undercatch is more noticeable at higher-elevation sites during wet years (Figure S8).

2.4 Gridded precipitation and snow datasets

The 800-m gridded daily PRISM precipitation dataset (http://www.prism.oregostate.edu) was used to compare precipitation estimates and OPGs from the blending approach described below. The data are interpolated based on precipitation from 13,000 gauges, and make use of snow-course measurements (Henn et al., 2015), with a climate-elevation regression that accounts for many influences, such as topographic aspect and position, coastal proximity, and orographic effectiveness of terrain (Daly et al., 1994, 2008). The spatial climatology from PRISM is used in other gridded precipitation data (e.g. NLDAS-2, Xia et al., 2012). PRISM data are also actively used as inputs for hydrologic models (e.g. Avanzi et al., 2020a). This study averaged PRISM data by 100-m elevation bands in the American River basin for our analyses.

We also collected WSR-88D radar-based precipitation data, which have sufficient spatial coverage and resolution in complex terrain (Gourley et al., 2009; Matrosov et al., 2007; Zhang et al., 2016). The Multi-Radar Multi-Sensor (MRMS) precipitation data at 1-km resolution include a correction for the vertical profile of radar reflectivity (Qi et al., 2013; Zhang et al., 2012) and also incorporate gauges, plus atmospheric environmental and climatological data (Zhang et al., 2016). We retrieved hourly gauge-corrected MRMS precipitation data (https://mtarchive.geol.iastate.edu) for WY2016-2017, and then aggregated them to daily resolution. The daily MRMS data in the American River basin were averaged to 100-m elevation bands.

The 90-m daily SWE reanalysis data (Margulis et al., 2016) are available for the Sierra Nevada above 1500 m for WY1985-2016. The data were generated using a Bayesian data-assimilation framework with Landsat fractional snow cover and a snow model driven by NLDAS-2 forcing (Huning & Margulis, 2018). The daily SWE increase at each pixel was calculated as daily solid precipitation, which was then averaged to 100-m elevation bands to estimate OPGs. The

solid precipitation and OPGs from the SWE reanalysis data were used to compare the results from our blending approach, described below.

2.5 Atmospheric data

We augmented our analyses of ground-based precipitation using atmospheric data, including vertically Integrated water-Vapor Transport (IVT, vector with a unit of kg m^{-1} s^{-1}). IVT describes the direction and intensity of moisture flux in an atmospheric column. It is calculated by integrating wind speed and specific humidity from 1000 to 300 hPa. The IVT is widely used to define and categorize atmospheric rivers (Pan & Lu, 2019; Ralph et al., 2019), which contribute 20-40% of annual precipitation on the west coast of the U.S., and up to 50% for California (Dettinger et al., 2011; Lavers & Villarini, 2015). We used hourly IVT data from the Modern-Era Retrospective analysis for Research and Applications, Version 2 (MERRA-2 with a resolution of 0.5° lat × 0.625° lon, ~ 50 km in latitudinal direction), produced by the National Aeronautics and Space Administration's (NASA's) Global Modeling and Assimilation Office (http://gmao.gsfc.nasa.gov, Gelaro et al., 2017).

The Sierra Barrier Jet (SBJ) is a low-level, dynamic barrier jet along the windward slope of California's northern Sierra Nevada that strongly affects the magnitude and distribution of orographic precipitation (Hughes et al., 2012; Lundquist et al., 2010; Marwitz, 1983; Neiman et al., 2010, 2013; Ralph et al., 2016). Here we include the 915-MHz wind profiler (Carter et al., 1995) data at Chico (CCO, 39.699° N, 121.907° W, 42 m elevation, https://psl.noaa.gov/data/obs/sites/view_site_details.php?siteID=cco) to determine the SBJ occurrence and height. The CCO profiler data were retrieved from NOAA's Physical Sciences Laboratory (https://psl.noaa.gov/data/obs/data). Following the Neiman et al. (2010) method, SBJs are identified based on hourly averaged Sierra-parallel (directed from 160° to 340°) wind speed (V). The SBJ requires that: i) a relative maximum V ≥ 12 m s^{-1} at an elevation located between profiler's second range gate (200 m above ground) and the Sierra crest (3000 m), and ii) V decreases by more than 2 m s^{-1} between the height of maximum V and 3000 m. The SBJ height is the elevation where the maximum V is presented.

We also used the atmospheric-snow-level data at Colfax (39.080° N, 120.938° W, 644 m elevation, Figure 1) in the American River basin. The snow-level data indicate the elevation at which the probability of precipitation falling as snow is 50%, with an assumption of uniform snow level across the basin. They are determined based on the Frequency-Modulated Continuous Wave (FMCW) radar-detected reflectivity (Johnston et al., 2017; White et al., 2002, 2010). We retrieved the snow-level data from NOAA's Physical Sciences Laboratory (https://psl.noaa.gov/data/obs/data) and averaged them to hourly resolution. Although radar snow levels tend to be higher than the rain-snow transition elevation from ground measurements in mountain areas (Cui et al., 2020; Lundquist et al., 2008), the FMCW radars provide valuable, near-real-time snow-level information to forecasters for operational use.

2.6 Precipitation estimation

Our blending approach parses rain versus snow using a combination of sensors, measurement thresholds, and models (Figure 2) to arrive at an estimate of the liquid content for both rain and snow at each wireless sensor. Precipitation days (defined as days with average PRISM precipitation in the upper basin larger than 0.254 mm, i.e. the measurable precipitation 0.01 inch by the National Weather Service (Sumargo et al., 2020)) were used to identify precipitation events. An event was defined as consecutive precipitation days with cumulative precipitation greater than 2 cm. We also manually checked each event by visually examining monthly data (e.g. Figure S9), including radar snow level, SBJ height, gauge precipitation, averaged PRISM precipitation in the upper basin, and IVT at Folsom Dam. Table S1 lists the 60 precipitation events identified during WY2014-2017. Events were classified as AR-related and/or SBJ-related according to the occurrences of AR and SBJ. As an example illustrated in Figure S10, an AR-related event was classified by visually checking (Cui et al., 2020) and automatically detecting (Goldenson et al., 2018) whether an IVT pattern (≥ 250 kg m^{-1} s^{-1}) with a long (> 2000 km) and narrow (< 1000 km) corridor intersected the northern Sierra Nevada during the event (Demaria et al., 2017). We also classified precipitation events as SBJ-related if at least 8 consecutive hourly SBJ heights occurred during the event; see Figure S11 as an example. Event-averaged SBJ heights were calculated and listed for all SBJ-related events in Table S1.

For each sensor node, we first classified each precipitation day as a snowfall or rainfall day (Figure 2) based on its daily snow-depth change, meaning that the precipitation-day classification can vary across sensors on the same day. A positive snow-depth change indicated a snowfall day, and a precipitation day with unchanged or decreased snow depth was termed a rainfall day. Note that snow-depth change is also subject to localized processes (Elder et al., 1991, 1998; Winstral & Marks, 2002), e.g. wind redistribution (Dadic et al., 2010), sublimation (Stigter et al., 2018), and compaction by metamorphism and overburden (Ryan et al., 2008). We recognize that these processes could introduce uncertainties, but it is beyond the scope of the paper to investigate these potential error sources. However, the wireless-sensor network was specifically designed as a set of sensor clusters, with nodes strategically placed to encompass the variability of attributes that influence snow distribution (Zhang et al., 2017b). Precipitation during both snowfall and rainfall days can consist of both liquid and solid precipitation (i.e. rain-snow mixed; purple box in Figure 2), which was partitioned using snow fraction (i.e. the ratio of daily solid precipitation over daily total precipitation) based on wet-bulb temperature (T_{wet}). We assumed that precipitation with T_{wet} below 0 °C (above 1 °C) is all snow (rain). During snowfall days we first estimated solid precipitation using accumulated snow depth and new-snow density (blue box in Figure 2). Then if precipitation is determined as all snow, total precipitation equals solid precipitation. Otherwise, total precipitation is the sum of solid and liquid precipitation estimated using snow fraction (purple box). During rainfall days total precipitation was first estimated by a machine-learning random-forest model (red box). Then if precipitation is determined as all rain, total precipitation equals liquid precipitation. Otherwise, solid and liquid precipitation is partitioned using snow fraction and total precipitation (purple box in Figure 2). Details of the methods for estimating precipitation during snowfall and rainfall days at each sensor node are described below.

2.6.1 Snowfall days.
Assuming that daily snow-depth increments were mainly caused by new-fallen snow, the amount of solid precipitation (i.e. SWE increment) received on the ground was computed as the snow-depth increment multiplied by new-snow density. The daily new-snow density (ρ_{new}, kg m^{-3}, Equation 1) was estimated based on the daily SWE and snow-depth increments from co-located snow pillows and snow-depth sensors at 13 operational sites in the American River and nearby basins (Table S2).

$$\rho_{new} = \frac{\rho_w}{n} \sum_{i=1}^{n} \frac{\Delta SWE_i}{\Delta SD_i} \qquad (1)$$

where ΔSWE_i (mm) and ΔSD_i (mm) are daily SWE and snow-depth increments at site i, respectively, n is the number of sites that recorded increments in both SWE and snow depth on a given day, and water density ρ_w is 1000 kg m^{-3}. The averaged ρ_{new} across sites was used to construct a daily time series of new-snow density (Figure S12), which was gap-filled using a nearest-neighbor interpolation for the days without ρ_{new} estimates.

During snowfall, the wet-bulb temperature (T_{wet}) can sometimes be above 0 °C. In this case, we used snow fraction to estimate liquid precipitation (i.e. rainfall) and total precipitation (summation of liquid and solid precipitation). Snow fraction was estimated based on T_{wet} (Behrangi et al., 2018b; Casellas et al., 2020; Cleave et al., 2019; Cui et al., 2020; Ding et al., 2014; Olsen, 2003; Sims & Liu, 2015; Tamang et al., 2020; Wang et al., 2019; Zhong et al., 2018). We first calculated hourly dew-point temperature using air temperature and relative humidity by an empirical equation (Lawrence, 2005; Zhang et al., 2017a). Then, we iteratively derived hourly wet-bulb temperature at each sensor node using air and dew-point temperatures in the psychrometric equation (Marks et al., 2013). The rain-snow-transition in Utah (Cleave et al., 2019) and Sierra Nevada (Cui et al., 2020) mountains was found at the elevation at which T_{wet} was 0.5 °C. The dominant precipitation phase is snow above the rain-snow-transition, and precipitation is rain-dominated below the transition. We used a function with daily T_{wet} (averaged from hourly data) to calculate daily snow fraction (SF) at each sensor node (Cui et al., 2020; Susong et al., 1999; Zhang et al., 2017a). In general, we assumed a linear relation between T_{wet} and snow fraction.

$$SF = \begin{cases} 0, & T_{wet} \geq 1°C \\ \max(0.4, 1 - T_{wet}), & 0 < T_{wet} < 1°C \\ 1, & T_{wet} \leq 0°C \end{cases} \qquad (2)$$

Daily total precipitation during snowfall days was estimated by solid precipitation divided by snow fraction, and

liquid precipitation was calculated as total precipitation minus solid precipitation. To avoid unrealistic large total precipitation resulting from solid precipitation dividing by a small snow-fraction value, we set the minimum value of snow fraction to 0.4 when T_{wet} is in between 0 and 1 °C, similar to the approach of assigning a minimum value of snow fraction in Jordan's rain-snow-partitioning scheme (Jordan, 1991; Wang et al., 2019). The minimum value of snow fraction was selected according to model performance evaluated in Section 3.2.

The rain-snow-transition zone, where mixed-phase precipitation occurs, was determined as the elevation range with T_{wet} between 0 and 1 °C using hourly data from wireless-sensor nodes. This hourly time series tracks the elevation where precipitation transitions from rain to snow during a precipitation event, as also indicated by the atmospheric snow level from the FMCW radar.

2.6.2 Rainfall days.
Total precipitation during rainfall days was estimated by a random-forest model, which can capture non-linear dependencies based on regression trees (Breiman, 2001; Denisko & Hoffman, 2018; Koch et al., 2019). Since snow depth decreases during rain-on-snow (McCabe et al., 2007), we assumed that decreasing snow depth during rainfall days is primarily caused by rain-on-snow process and driven by liquid precipitation. Daily snow-depth change at wireless-sensor nodes is used as one candidate predictor variable. Since the atmospheric-moisture variable IVT is closely associated with precipitation (Pandey et al., 1999), but is more predictable than precipitation (Lavers et al., 2016, 2017, 2018), daily averaged IVT intensity and direction are used as two candidate predictor variables. Together with other variables, i.e. T_{wet}, air temperature, relative humidity, snow depth, and water-year day (days after October 1), we initially had eight candidate predictor variables. Then we used Boruta feature-selection method (Kursa & Rudnicki, 2010) to select input variables from the eight candidates. Based on the ranking of features, five variables (IVT intensity, relative humidity, daily snow-depth change, and IVT direction) were finally selected and used in the random-forest model.

The wireless-sensor clusters at six sites (BTP, OWC, DUN, ALP, CAP, and ECP, Table S3) had precipitation gauges. Four sites (OWC, ALP, CAP, and ECP) provided continuous daily precipitation. Gauge data from BTP and DUN appear to be missing or undercatching multiple events (Figures S13a, c). To ensure that our model was trained with quality data, we only included consistent precipitation data at BTP and DUN by comparing them to daily precipitation extracted from PRISM (Figures S13b, d). We selected data from the sensor node nearest the operational gauge to train the model for predicting total precipitation. Note that precipitation at ECP was not wind-adjusted, as an anemometer was not co-located at this site, while precipitation data at the other five sites were wind adjusted. Using the trained random-forest model, total precipitation at all wireless-sensor nodes was estimated. For daily T_{wet} < 1°C, solid precipitation was estimated as total precipitation multiplied by snow fraction.

To indicate dominant precipitation days (i.e. snowfall and rainfall days) within the sensor network during a precipitation event (Table S1), we further classified events into three types according to the rain-snow transition elevation: cold ($\geq$ 50% hourly transition elevation during the event is lower than 1500 m), mixed-phased ($\geq$ 50% transition elevation in between 1500 and 2700 m), and warm ($\geq$ 50% transition elevation higher than 2700 m).

2.7 Orographic precipitation gradient
To investigate the hydrologically important precipitation gradient with elevation, we used the Orographic Precipitation Gradient (OPG, α unit of km^{-1}) following Lundquist et al. (2010), instead of the precipitation lapse rate (β, cm km^{-1}) that varies with precipitation totals (Bohne et al., 2020) and event duration, thus hindering the comparison of orographic enhancement across different events. We defined the OPGs for the lower and upper basins separately. The α denotes the precipitation at a specific elevation z (km) relative to the reference precipitation at a lower elevation. To reduce the impact of potential outliers on OPG estimates, we first fitted linear models of precipitation data with elevation, for the upper and lower basins separately, using the robust Huber regression (Huber, 1973), which is less sensitive to outliers (Vetter et al., 2015).

$$\hat{P}(z) = \beta z + \gamma \quad (3)$$

Here β (cm km^{-1}) is the fitted slope, the same as the precipitation lapse rate used in Zhang et al. (2017a), γ (cm) is the fitted intercept, and $\hat{P}(z)$ with a unit of cm is the regression-predicted precipitation at elevation z.

Then OPG α was calculated using the fitted precipitation data $\hat{P}(z)$ by Equations 4 and 5.

$$\text{Lower basin (z < 1.5 km)}: \frac{\hat{P}(z)}{\hat{P}_0} = 1 + \alpha_{lower}(z - z_0) \quad (4)$$

$$\text{Upper basin (z} \geq \text{1.5 km)}: \frac{\hat{P}(z)}{\hat{P}_1} = 1 + \alpha_{upper}(z - z_1) \quad (5)$$

For calculating the lower-basin α_{lower}, $\hat{P}_0$ is the fitted precipitation at the lower reference elevation z_0 of 0.2 km. For calculating the upper-basin α_{upper}, $\hat{P}_1$ is the fitted precipitation at the upper reference elevation z_1 of 1.7 km. By computing the least-squares solutions of linear equations 4 and 5, the OPGs α_{lower} and α_{upper} were obtained for total, solid, and liquid precipitation with either point estimates or 100-m-banded gridded data. For the upper-basin α_{upper} from the sensor network, OPGs were calculated using precipitation estimates at all sensor nodes, which may have a blend of snowfall days and rainfall days during an event.

3 Results

3.1 Precipitation events
Data from two wireless-sensor clusters, SBJ height, two precipitation gauges, and the IVT at Folsom Dam for WY2017 illustrate the range of measurements for a wet water year (Figure 3). The higher-elevation CAP site (2440 m) had deeper snow, longer snow-cover duration, and 46-cm more annual precipitation than did OWC (1566 m). Annual air temperature at CAP (4.2 °C) was lower than at OWC (8.8 °C), while no apparent difference in relative humidity between the

two clusters emerged (mean annual values of ~67% for both CAP and OWC). The atmospheric IVT at Folsom Dam from the MERRA-2 dataset was positively correlated with precipitation amount, with correlation coefficients of 0.69 for CAP and 0.70 for OWC. As the CCO wind profiler had a failure from April to July 2017, the SBJ height was not identified during the outage (Figure 3d), and three precipitation events in April were assumed to not be related to SBJ (Figures 3d, e, f). Note that the SBJ heights showed hourly variability (Figure S11). Of the 20 precipitation events in WY2017, 15 were AR-related, and 12 were SBJ-related. Among all 60 events in WY2014-2017, 15 were cold, 41 mixed-phased, and four warm events (Table S1).

3.2 Model evaluation

New-snow density and snow fraction for snowfall days. We evaluated our new-snow density by comparing with those estimated from two other methods (Figure S14). One was daily manual measurements of new-snow density collected by Mammoth Mountain Ski Patrol at Sesame in the eastern Sierra Nevada (37.650° N, 119.042° W, 2743 m elevation, Figure S12) from Bair et al. (2018), and the other was an air-temperature-based new-snow density used in the Noah-MP land surface model (Hedstrom & Pomeroy, 1998; Niu et al., 2011). Using the data on cold, snowy days when the daily rain-snow-transition elevation was lower than the lowest elevation of the 13 snow pillows, results show that estimated SWE increments using the new-snow density in this study had the best agreement (R^2 of 0.56; Root Mean Square Error (RMSE) of 1.13 cm) with measured SWE increments, compared to those from Bair et al. (2018) and the air-temperature-based method, which had R^2 values of 0.14 and 0.29, and RMSEs of 2.21 and 1.52 cm, respectively.

We compared total precipitation estimated from snow fraction and SWE increments versus gauge-measured total precipitation (Figures S15a,b), to examine our snow-fraction method (Equation 2) and select the minimum value of snow fraction. Another snow-fraction method based on a sigmoid function of T_{wet} used in the Noah-MP model (Wang et al., 2019) was included for comparison. Model results from both snow-fraction methods showed that RMSE decreases substantially when the minimum value of snow fraction increases from 0.05 to 0.2, but remains relatively stable for the minimum value of snow fraction ≥ 0.4 (Figure S15c). The R^2 value from our snow-fraction method increases with the minimum value of snow fraction (Figure S15d). However, R^2 value from the Noah-MP model continuously decreases when the minimum value of snow fraction is ≥0.4. Therefore, we set the minimum value of snow fraction=0.4, which can result in reasonable performances for both our snow-fraction method and the sigmoid-function method of the Noah-MP model (Figures S15a,b). Both explained 31% of the variance of gauge-measured total precipitation. The RMSEs were 2.38 and 2.44 cm for our snow-fraction method and the sigmoid-function-based method, respectively. Results from both methods show that 46% of gauge-measured total precipitation was lower than estimated total precipitation, reflecting

uncertainties from gauge measurements during snowfall, as well as uncertainties from snow-fraction estimates.

Random-forest model for rainfall days. As part of the rainfall-day calculation, a random-forest model was established using ~1300 daily precipitation values from six gauges (Table S3 including data distribution across gauges). We applied a grid-search method to tune model hyperparameters that maximize the mean of R^2 values of training and testing, e.g. number of trees in the forest (ranging from 50 to 450), maximum tree depth (5-35), minimum number of samples at a leaf node (1-6), and proportion of the dataset used in training (60%-90%). Finally, we used the tuned hyperparameters (number of trees in the forest = 200, maximum tree depth = 25, and minimum number of samples at a leaf node = 1, proportion of the dataset used in training = 85%) to train the random-forest model using shuffled data with a loss function of mean squared error.

Results indicate that the random-forest model could account for precipitation variability, with R^2 values of 0.94 and 0.75, and RMSEs of 0.54 and 1.00 cm for training and testing, respectively (Figure 4a). The larger difference in R^2 between training and testing suggests that there was some overfitting. The random-forest model tended to underestimate daily precipitation above about 10 cm, which applied to only 1.1 % of daily values. Overall, the model captured the non-linear dependency of precipitation on predictor variables. Three variables — IVT intensity, relative humidity, and daily snow-depth change — together contributed 87% of the relative feature importance in the predictive model, as suggested by normalized-permutation-feature importance calculated using the Python package rfpimp (Figure 4b).

To evaluate the random-forest model's effectiveness, we also trained the model with a larger amount of data (~5100) from PRISM precipitation at all 13 wireless-sensor clusters, using the same tuned hyperparameters. As illustrated by Figure S16, with more data the model's prediction performance for testing was better (R^2 of 0.89, RMSE of 0.77 cm). This indicates that more training data from gauges spread across the basin would improve precipitation estimates, and that our random-forest model is applicable for this study. We used the gauge-based random-forest model for the rest of the analysis.

3.3 Precipitation estimates

3.3.1 Event-scale precipitation totals and phase.
Five precipitation events are used to illustrate precipitation estimates from the sensor network and comparisons to snow pillows, precipitation gauges, and gridded data. Two cold events with low rain-snow-transition elevations include an extreme precipitation event on January 18-23, 2017 (cumulative PRISM precipitation 6th highest of the 60 events, Table S1) and an average event on January 4-9, 2016 (ranked 34th). The largest precipitation event on February 2-10, 2017 and a small summer event on September 20-23, 2017 (57th) are used to demonstrate precipitation estimates during mixed-phased events. A summer warm event on September 11-13, 2017 (smallest event) illustrates rain-only precipitation

estimates. Results for all 60 events can be found in the supporting information.

Cold events. The wireless-sensor network captured the occurrence of snowfall and estimated solid precipitation, as demonstrated by the AR&SBJ-related cold-storm event on January 18-23, 2017 (Figures 5a-g). Mean air temperature at all sensor nodes was below 0 °C, and those of the lowest node at BTP and the highest node at SCN were –0.5 and –7.2 °C, respectively. The rain-snow-transition zone was mostly below the lowest sensor node at 1510-m elevation (80% of snowfall time), which was in line with snow-level radar observations (89% of the radar-detected snow-level data were lower than the lowest sensor node, Figure 5a). Snow pillows at three sites (EP5, CAP, and FRN) recorded SWE increase during the event (Figure 5d). The maximum daily SWE increment was 9.3 cm d^{-1} observed at FRN on January 22. However, the precipitation from the gauge at CAP was 75% of accumulation on the co-located snow pillow, while the other two gauges captured much less of the solid precipitation during the event (38% for FRN and 5% for EP5). The mean snow-depth increment from sensor clusters was 107 cm (Figure 5c). Estimated snowfall precipitation from the sensor network (Figure 5f) is consistent with operational data (Figure 5d), with the peak precipitation (mean 5.7 and maximum 10.8 cm d^{-1}) on January 22. Note that few sensor nodes (at OWC, MTL, and SCN) recorded decreasing snow depth on 20-22 January, likely caused by snow settling and redistribution. These sensor nodes were originally classified as experiencing rainfall days, and thus the total precipitation at these sensors was first automatically estimated by the random-forest model with their snow-depth loss (red box in Figure 2). However, the T_{wet}-based snow fraction algorithm caught the error and corrected it to snowfall, by automatically partitioning total precipitation to solid precipitation, since their T_{wet} values were below 1°C (purple box in Figure 2). Thus, all the precipitation from the wireless-sensor nodes was in the form of snow (Figure 5f), meaning that none of the sensor nodes experienced rainfall (Figure 5g).

During the cold event in January 2017, positive OPGs of lower-basin total precipitation were 1.6 and 1.3 km^{-1} from the gauges and PRISM data, respectively (Figure 6b). For solid precipitation in the upper basin (Figure 6a), the sensor network observed a positive OPG of 0.2 km^{-1}, and snow pillows showed a slightly negative value of –0.1 km^{-1}. The average cumulative solid precipitation from the sensor network (23 cm) agreed with that from snow pillows (25 cm). For the upper-basin total precipitation, both the sensor network and the banded PRISM data had an OPG of 0.1 km^{-1}. The average cumulative total precipitation from the sensor network (23 cm) agreed with that from PRISM (24 cm). Although gauges showed a positive upper-basin OPG of 0.5 km^{-1}, the cumulative total precipitation estimates from gauges were quite scattered and underestimated, with a mean value of 12 cm, reflecting precipitation measurement issues from upper-basin gauges during snowfall.

Another snow-only event in January 2016 (Figure S17) was chosen to compare upper-basin solid precipitation between the senor network and the gridded SWE reanalysis data, since liquid precipitation could not be inferred using only SWE reanalysis data. The mean solid precipitation (5.1 cm) from the sensor network was close to that (5.6 cm) from the SWE reanalysis (Figure S18a). At a basin scale, the sensor network represented the solid-precipitation variabilities from the SWE reanalysis, as indicated by the similar coefficient of variation (CV) of 0.35. On a 100-m-elevation-band scale, banded-solid-precipitation CVs from the sensor network typically accounted for 75% of those from the SWE reanalysis (Figure S18b). The SWE reanalysis included larger precipitation above 2400-m elevation, which was not shown in the sensor network, resulting in a larger positive OPG from SWE reanalysis (0.3 km^{-1}) than that from the sensor network (0.1 km^{-1}). This was expected given that the spatial coverage of the wireless-sensor nodes was much smaller than the ~2,160,000 grided points represented by the SWE reanalysis. The general agreement of solid precipitation estimates indicates that the blending approach based on snow-depth change and new-snow density is applicable during snow events.

Mixed-phased events. The largest precipitation event on February 2-10, 2017 was related to both an AR (Category 4, Ralph et al., 2019) and an SBJ, with intense moisture flux (peak of IVT > 750 kg m^{-1} s^{-1}, Figure 5i) from the Pacific Ocean affecting the American River basin. During the first five days (Feb. 2-6), the rain-snow-transition zone was relatively low (1820 m, Figure 5h). Most sensor nodes (76%) continuously received snowfall (Figure 5m), while some sensors below 1830 m occasionally experienced rainfall (Figure 5n). Snow pillows and precipitation gauges at three operational sites (> 2300 m elevation) recorded precipitation as snow (Figures 5k, l). In the following two days (Feb. 7-8), the warm atmospheric-river core came across the basin, resulting in an elevated rain-snow-transition zone (2470 m), as shown by both the sensor network and radar (Figure 5h). The high rain-snow-transition zone and intense atmospheric-moisture flux caused heavy rainfall at most sensor nodes, except for the highest-elevation sensor nodes at SCN (2673 m), which experienced snowfall (Figure 5m). The rain-on-snow event resulted in snow-depth decreases at all sensor clusters, as much as 52 cm, again except for SCN (Figure 5j). The snow pillow and gauge at EP5 also showed SWE loss due to rain-on-snow. After Feb. 9, as the atmospheric-river core passed and moisture flux started to diminish (Figure 5i), the rain-snow-transition zone dropped in elevation (Figure 5h). On Feb. 9, with still relatively large IVT, sensor nodes at higher elevations (> 2100 m) received as much as 17 cm of solid precipitation and showed increased snow depths, as much as 51 cm (Figures 5j, m).

During the largest February 2017 event, lower-basin total precipitation from gauges and PRISM showed positive OPGs of 1.7 and 1.0 km^{-1}, respectively (Figure 6d). In the upper basin (Figure 6c), both the sensor network and snow pillows showed a similar elevational trend of solid precipitation, with large OPGs of 5.0 and 3.2 km^{-1}, respectively. The upper-basin OPG of total precipitation from the sensor network was 0.4 km^{-1}, however those from gauge and PRISM data were negative, –0.1 and –0.2 km^{-1}, respectively (Figure 6d).

Average upper-basin cumulative-precipitation estimates from three sources were comparable (37, 37, and 39 cm for the sensor network, gauges, and PRISM, respectively). Above 2300 m, gauge and PRISM data tended to show less total precipitation than did the sensor network.

During another mixed-phased event (September 20-23, 2017), the upper-basin-average T_{wet} was 0.78 °C, and the mean transition elevation was 2100 m (Figure S19a). Mean solid precipitation was ~1 cm estimated by the blending approach (Figure 6e). The small snow accumulation during this summer event was not represented by the cleaned daily data from the sensor network and snow pillow, though there were some fluctuations in raw hourly and daily data (Figure S20). The snowfall occurrence was reported in the news (e.g. CBS News, https://www.cbsnews.com/news/snow-last-day-of-summer-sierra-nevada-turns-deadly/). Positive OPGs of total precipitation in the upper and lower basins were captured by all three sources (Figure 6f). Figure 6e reflects an advantage of the blending approach using the sensor network and the random-forest model, since solid precipitation with a positive OPG was estimated using total precipitation multiplied by snow fraction, even when cleaned snow data from ground sensors did not represent small snow accumulation.

Warm event. During the summer rain-only event on September 11-13, 2017 (Figures 6g, h), the upper-basin-average T_{wet} was 10.7 °C, and the rain-snow transition elevation was above 3000 m (Figure S21a). Upper-basin liquid presentation from gauges and PRISM was expected to be less affected by gauge undercatch. Thus, positive OPGs of upper-basin precipitation due to orographic enhancement (Dawdy & Langbein, 1960; Dettinger et al., 2004) were represented by all three sources. Both the sensor network and gauges estimated a precipitation amount of 2.0 cm, slightly larger than 1.2 cm from PRISM.

3.3.2 Annual precipitation. For the lower basin, both gauges and PRISM yielded positive annual total-precipitation OPGs (0.67-1.68 km^{-1}, Table S4) for WY2014-2017 (Figure 7). For the upper basin, total-precipitation values from the senor network were positive (0.09-0.58 km^{-1}), while those from gauges and PRISM were negative (−0.33 to −0.09 km^{-1}). The sensor network and snow pillows captured positive upper-basin solid-precipitation OPGs (0.95-3.64 km^{-1}, Figure 8). Due to decreasing T_{air} and T_{wet} with elevation, snow ratio (annual solid precipitation over total precipitation) increases (Figure S22). An increasing snow ratio with elevation results in less liquid precipitation in higher elevations (i.e. negative upper-basin liquid-precipitation OPGs, Figure 8). Although gauge-precipitation undercatch in high elevations may contribute to the negative OPGs for liquid precipitation, their undercatch amounts (Figure S8) were considerably smaller than the liquid precipitation decrements with elevation (Figure 8). Therefore, the negative OPGs for liquid precipitation in the upper basin were dominated by the increased snow ratio caused by temperature decrease. Note that Huning & Margulis (2018) found that the southwest basins in the Sierra Nevada exhibited negative elevational trends of solid precipitation above 3000 m; but solid precipitation in the American River basin monotonically increased along elevation. Kirchner et al.

(2014) observed the declining precipitation over 3300-m elevation (very small area) in the southern Sierra Nevada, likely due to exhaustion of atmospheric moisture and reduced orographic lifting. While this could be the case for smaller storms, larger storms that possess large amounts of consistent IVT will likely not experience moisture exhaustion in the American River basin. For example, the Category-4 AR during the event in February 2017 provided sufficient atmospheric moisture for orographic precipitation in the upper American River basin (Figure 5i), yet gauges and PRISM did not show the positive OPG of total precipitation shown by the sensor network (Figure 6d). Further, since the American River basin is principally below 3000 m, solid-precipitation OPGs in the upper basin were positive, suggesting that upper basin values for total precipitation should also be generally positive (Figures 6b, d, f, h). However, the upper-basin total-precipitation OPGs from the sensor network were smaller than those in the lower basin (Figure 7). The unusual negative OPGs of upper-basin total precipitation from gauges were likely due to uncertainty in gauge measurements of precipitation, particularly solid precipitation. As PRISM data are based on both gauge data and snow-course measurements (Henn et al., 2015), PRISM showed less-negative values (Figure 7). Note that physical mechanisms, e.g. thermodynamics, wind redistribution, microphysics, and terrain slope can change mountain precipitation patterns and may result in precipitation decrease at high elevations (Huning & Margulis, 2018; Lundquist et al., 2019; Siler & Roe, 2014), which were not investigated in this study. For radar-based precipitation (Figures 7c, d), MRMS data had positive lower-basin OPGs of 0.57 and 0.54 km^{-1} for WY2016 and 2017, respectively. MRMS precipitation agreed with PRISM data at lower elevations below 1000 m. However, MRMS data showed noticeable underestimates of precipitation above 1500-m elevation, compared to other sources, reflecting the challenges to obtaining accurate radar-based precipitation in mountains (Zhang et al., 2012).

The sensor network typically estimated higher total precipitation amounts than did gauges and PRISM at elevations over 2000 m (Figure 7), except in the dry year WY2015, with its exceptionally low snowpack. This is because more than half of the total precipitation above 2000 m was snow (Figure S22). The total precipiation between 1500 and 2000 m elevation from the sensor network was generally lower than that from the gauges and PRISM. Taking wet WY2017 as an example (Figure 7d), total precipitation above 2000 m from the sensor network averaged 21 and 37 cm more than those from PRISM and gauges, respectively. For elevations between 1500 and 2000 m, the sensor network underestimated precipitation by 50 and 38 cm compared to PRISM and gauges, respectively. This underestimation likely reflects sensor clusters having limited spatial coverage in that elevation range. Note that total precipitation from a sensor cluster matched the co-located-gauge values (e.g. OWC at 1586 m in the South Fork American River; Figure 7c). However, for the higher precipitation at BLC (1609 m, Figure 7c) in the North Fork American River, total precipitation was not well represented by the sensor network due to spatial

variability of precipitation (relatively higher in the North Fork American River), although the elevation difference between OWC and BLC is small. The gauge values from both OWC and BLC compared well to those from PRISM (Figure S23). A caveat here is that the relatively low precipitation at OWC was used as training data in the random-forest model, which possibly resulted in the larger upper-basin total-precipitation OPGs from the blending approach. Smaller upper-basin OPGs would likely be obtained if BLC or a different gauge at low elevation were used as a training gauge. It is apparent that a precipitation gauge may not record well. For example, the training gauge at FRN (2318 m) measured anomalously low precipitation in WY2016 (Figure 7c). The blending approach using the sensor network showed a robust performance with the ability to handle the isolated unusual observation at FRN, since no significant deficiency of precipitation estimates was found near FRN's elevation, compared to other gauges and PRISM.

For annual solid precipitation in the upper basin, the sensor network showed good agreement with snow pillows in WY2014-2016, with a difference of mean values less than 12 cm. In wet WY2017, the solid precipitation from the sensor network averaged 33 cm lower than the snow pillows (Figure 8d). The sensor network averaged 22, 23, and 23 cm higher than values from the SWE reanalysis for WY2014-2016, respectively (Figures S24a, c, e). This is plausibly due to the fact that solid precipitation during rain-on-snow could not be easily obtained from the SWE reanalysis. Although the gridded SWE reanalysis dataset could not estimate total and liquid precipitation, it captured a larger spatial variability of solid precipitation than did the sensor network (Figures S24b, d, f).

3.4 Orographic precipitation during different events

For all precipitation events in WY2014-2017 (Figure 9), the sensor network and snow pillow yielded positive OPGs for upper-basin solid precipitation for 98% and 64% of the events, respectively; and respective median values were 0.89 and 0.58 km^{-1}. For partitioned liquid precipitation in the upper basin, most sensor-network OPGs (90%) were negative, with a median of –0.96 km^{-1}. Combining positive solid-precipitation OPGs and negative liquid-precipitation values, the sensor network showed positive OPGs of upper-basin total precipitation for 77% of the events, with a median of 0.57 km^{-1}. However, the values from gauges and PRISM were negative for 73% of events, with medians of –0.35 and –0.13 km^{-1}, respectively. As there was less snow in the lower basin, both gauges and PRISM observed positive lower-basin total-precipitation OPGs, with medians of 1.23 and 1.00 km^{-1}, respectively. For total precipitation, the sensor-network results demonstrate that the upper-basin values are generally positive but smaller than those in the lower basin.

ARs produced higher positive event-aggregated OPGs for lower-basin total-precipitation and upper-basin solid-precipitation, compared to those for aggregated Non-AR events (Table 3). However, the upper-basin total-precipitation values from gauges and PRISM during aggregated AR (SBJ) events were more negative, compared to those during Non-AR

(Non-SBJ) events. Compared to aggregated low-SBJ events, high-SBJ events had smaller lower-basin total-precipitation OPGs from gauges and PRISM, and had larger upper-basin total-precipitation values from the sensor network but more-negative upper-basin total-precipitation values from gauges and PRISM. Since a low SBJ allows more low-level airmass flow across the lower mountain (Lundquist et al. 2010), the OPG is larger during low-SBJ than during high-SBJ events. As such, the largest OPGs of lower-basin total precipitation were found in the aggregated events with AR and Non-SBJ, as AR provides mountain-perpendicular moisture that is not blocked by SBJ.

Across the 60 events, 21 events were associated with both an AR and an SBJ (Figure 10 and Table 3); however, these aggregated heavy AR&SBJ events contributed 62% (289 cm) of upper-basin total precipitation (467 cm) and 61% (195 cm) of upper-basin solid precipitation (322 cm). In the lower basin, the positive OPGs of total precipitation did not show a statistically significant difference between mild Non-AR&Non-SBJ events and heavy AR&SBJ events (Figures S25a, c). However, the upper-basin OPGs for total precipitation from gauges and PRISM were more negative (p-values <0.03 from two-tailed student's t-tests, Figures S25b, d) during the AR&SBJ events than during the Non-AR&Non-SBJ events. As AR and SBJ transport a large amount of moisture together with strong wind, we expect that the OPGs of total precipitation in the upper basin should be positive, as indicated by the sensor network. Again, negative OPGs for total precipitation in the upper basin from gauges and PRISM should be viewed cautiously, likely caused by relatively few measurements and potential gauge undercatch during heavy AR&SBJ events.

4 Discussion

With dense measurements, particularly for snow, our blending approach provides additional precipitation information in high-elevation mountain terrain, complementing precipitation from less-dense operational gauges and gridded datasets. Here, we discuss the use of distributed-sensor measurements to assist precipitation estimation, and the potential for real-time application, and finally the limitations of the method.

4.1 The use of distributed-sensor measurements for precipitation estimation

In rain-snow mixed mountain areas, precipitation undercatch is a concern for gauge measurements. Snow pillows are one of the few high-elevation gauge networks, and so offer useful insight into precipitation-accumulation totals in higher-elevation snow-dominated areas. This study found that gauges and gridded data may underestimate precipitation and infer negative OPGs at higher elevations during cold storms. Blending in more snow measurements can contribute to more accurate precipitation estimates, with wireless-sensor networks providing a convenient way to incorporate more high-elevation data.

Compared to common operational observations, the wireless-sensor network can provide value-added measurements of snow depth, temperature, and humidity,

reflecting spatial variability and reducing hydrologic uncertainty (Zhang et al., 2017b). The blending approach uses snow depth plus new-snow density to estimate partitioned precipitation during snowfall, increasing the certainty of precipitation through more distributed measurements. In terms of solid precipitation, estimates from the sensor network showed a relative difference of –7% (i.e. lower) compared to those from snow pillows during WY2014-2017 (Figure S26). One plausible uncertainty may be the new-snow density (Figure S12), used to convert snow-depth increment to solid precipitation. This study's new-snow density ranged from 98 to 343 kg m^{-3}, with a mean value of 166 kg m^{-3}. The measured new-snow density from Bair et al. (2018) presented a similar distribution (Figure S12a), but with a smaller mean value of 129 kg m^{-3} compared to the density used in this study. Note that the large daily densities in both this study and Bair et al. (2018) often resulted from declining snow depth due to rain-on-snow, e.g. the 343 kg m^{-3} in this study was estimated during the event on Feb. 7-9, 2017 (Figures 5j, k). Thus, this study used new-snow density slightly higher than the measurements from earlier studies, for example, 120 kg m^{-3} in the central Sierra Nevada (McGurk et al., 1988) and measurements ranging from 10 to 257 kg m^{-3}, and modes (peaks) of six individual-site histograms from 60 to 100 kg m^{-3} in the central Rockies (Judson & Doesken, 2000). However, using the eastern Sierra values from Bair et al. (2018), the relative difference of solid-precipitation estimates compared to snow pillows was –27%, which is about four times that using our derived new-snow density in this study (Figure S26). Together with the comparison between different new-snow densities (Figure S14), we assess that the new-snow density used in this study is more suitable for solid-precipitation estimation at our nodes. One reason for the smaller solid precipitation from the sensor network is that snow pillows may overestimate solid precipitation, since rain can be retained in the snowpack overlaying the pillow, and melting snow can lead to more water being stored (Langham et al., 1974).

4.2 Potential for near-real-time applications

The blending approach for estimating precipitation based on snow measurements can be further adopted and incorporated in near-real-time applications. The U.S. National Weather Service California-Nevada River Forecast Center (CNRFC) and the California Department of Water Resources jointly issue the streamflow forecasts for basins in the CNRFC region, including the American River basin (He et al., 2018). Quantitative Precipitation Forecasts (QPFs) from weather-forecast models, surface and upper-air observations, radar and satellite data (Ralph et al., 2010) and Quantitative Precipitation Estimates (QPEs) from on-the-ground rain gauge data (Willie et al., 2017) are used together with the PRISM precipitation climatology to produce the sub-basin-scale Mean Areal Precipitation (MAP), which is a key input for hydrologic modeling. For the American River basin, it is recommended to incorporate additional precipitation estimates from the blending approach in the upper basin, particularly in the snow-dominated areas above 2000 m. Once

the random-forest model of the blending approach is well trained using historical quality-controlled gauge-precipitation data, the precipitation at snow-observation sites during rainfall days can be estimated in near-real-time by the model using IVT, relative humidity, and snow-depth data (not requiring gauge data at prediction time; Figure 2). The proposed approach can be applied and evaluated in other operational snow-observation sites, further enlarging spatial coverage of additional precipitation estimates in high elevations.

From the perspective of forecasters, one practical way for benefitting near-real-time applications is to use the additional precipitation estimates at high elevations to update the PRISM climatology for the American River basin. This often requires long-time records of precipitation estimates from the research wireless-sensor network, which are currently not available. Since operational snow-observation sites often have longer-term measurements, the proposed approach can be applied to operational sites to generate long-term precipitation estimates, which can help update the PRISM climatology product. Another practical way is to treat these additional precipitation estimates as ground "precipitation measurements", supplementing the relatively sparse precipitation gauges in high elevations. These additional precipitation estimates can be easily included as near-real-time inputs for producing QPE and MAP.

There is also a need to broaden our use of observation information beyond inputs into a formal forecasting process. Near-real-time situational awareness of how the rain-snow-transition elevation is evolving and how orographic precipitation is enhanced and partitioned across mountains can help provide advance information on runoff-response changes during storms and help enable more-nimble water management. The blending approach incorporates multiple types of measurements, leveraging information less apparent in single-type observations to help provide reliable precipitation estimates in near-real-time for both flood forecasting and water-resource decision making. Further, since the same data can inform both flood-response and water-supply decisions, synergy may deliver important efficiency gains. This is particularly important to regions like California, where heavy AR&SBJ events often occur in wet winters and contribute a substantial amount of water supply.

4.3 Limitations of the study

Although the blending approach using snow measurements provides an alternative way to estimate mountain precipitation, some limitations still exist. First, the spatial coverage of precipitation estimates using snow measurements is somewhat limited, compared to gridded products, which can provide data at fine spatial-temporal resolutions.

Second, the blending approach used precipitation data from six gauges near our sensor network to train the random-forest model. Due to the high variability of weather-dependent precipitation in mountains, precipitation amounts in areas out of sensor-network coverage may not be well estimated. For example, precipitation at OWC (in the South Fork American River, Figure 7c) cannot represent the higher precipitation at BLC (in the North Fork American River) at a similar elevation

due to spatial precipitation variability other than elevation. Since precipitation at OWC is relatively low compared to other sites of a similar elevation, which might bias OPG estimates, we re-computed OPGs without OWC data (Figures S27 and S28). As expected, the OPGs from the sensor network were less positive, compared to corresponding results with OWC data (Figures 7 and 10). However, the main finding remains unchanged, which is that upper-basin OPGs from gauges and PRISM are lower than those from the sensor network. The sensor-network-based OPGs are sensitive to the limited spatial area and the limited number of training gauges used, whereas PRISM uses a much larger network of gauges over a wider area. This may explain their OPG differences. Thus, additional data from well-maintained precipitation gauges co-located with snow observatories across the entire basin could further improve the blending approach's predictive ability and OPG estimates.

Third, for estimating precipitation, there exists some uncertainties using daily changes of snow depth or SWE. For example, rainwater may enter and drain through a snowpack during warm precipitation events (Lundquist et al., 2015), while rain can also be frozen and retained in the snowpack (Langham et al., 1974). For AR events, the rain-snow-transition zone escalates quickly (e.g. Figure 5h), resulting in sub-daily-precipitation-phase changes at different elevations. Together with intense precipitation during AR events, ground snow depth or SWE changes considerably at a sub-daily time scale, either through accumulation or melting. If using net daily change of snow depth or SWE to estimate daily precipitation, sub-daily processes (e.g. warm storm melting snow at a short time) are not accounted for. Using snow changes at a sub-daily scale would improve precipitation estimates by capturing the alternating precipitation phase details between snow and rain. However, raw hourly gauge-precipitation and snow-depth data are not always available and can be quite noisy (Avanzi et al., 2014). This is an area of future work on many fronts (Avanzi et al., 2020b).

Fourth, this study assumed that decreasing snow depth during rainfall days is primarily caused by rain-on-snow process and driven by liquid precipitation. In fact, snow depth can also decline due to other processes during a precipitation event, e.g. wind redistribution, sublimation, and compaction, which all could distort snow depth (Brandt et al., 2020) and introduce uncertainty in estimating precipitation amounts. For example, the wireless-sensor networks at higher elevations (e.g. MTL site with less canopy cover) may be exposed to a large amount of wind redistribution, particularly during big storms associated with large amounts of moisture and wind. Stronger wind can also increase sublimation rate (Pomeroy & Goodison, 1997). However, during snowfall and rainfall, high atmospheric humidity substantially reduces sublimation (Stigter et al., 2018). Additionally, all wireless-sensor networks may experience snow compaction, that can be mainly driven by snow overburden during snowfall (Wayand et al., 2017), liquid precipitation during rainfall (Marshall et al., 1999), and metamorphism after a storm (Arthern et al., 2010; Wiese & Schneebeli, 2017).

Fifth, this study explored the OPGs during precipitation events that were classified by two important atmospheric processes, i.e. AR and SBJ for the northern Sierra Nevada. However, synoptic-scale storms and orographic lifting of moist air generate mountain precipitation, which is also modified by other atmospheric dynamic and physical processes (Lundquist et al., 2019). Although further investigation on atmospheric dynamics is beyond the scope of this study, performing meso- or synoptic-scale storm analysis can help distinguish strong versus weak orographic storms and explain orographic precipitation across the basin.

5 Conclusions

This study developed a new blending approach to estimate precipitation using snowpack measurements from a spatially dense wireless-sensor network, gauge precipitation, and atmospheric-moisture data. The blending approach provides partitioned solid snow and liquid rain in the upper, more snow-dominated basin, where precipitation gauges may significantly undercatch snowfall. Analysis of total and partitioned precipitation amounts in the lower and upper American River basin over 60 precipitation events classified by atmospheric-river and Sierra-barrier-jet influences leads to three main conclusions.

First, the blending approach overcomes potential precipitation biases from gauge undercatch during snowfall, and the inability to infer precipitation based on snow measurements during rain-on-snow events. As the blending approach incorporates ground snow measurements, its precipitation estimates are more reliable in the snow-dominated areas above 2000 m.

Second, as it is challenging for gauges to measure precipitation in the upper American River basin, negative OPGs of total precipitation derived from these gauges should be viewed cautiously, reflecting the urgency to incorporate snow measurements for more accurate precipitation estimation. In particular, the OPGs from gauges and PRISM are more negative during heavy AR&SBJ events with vast moisture and strong wind, compared to milder events. Since these heavy AR&SBJ events contribute substantial precipitation and are critical for water-resource and flood management, precipitation estimates and OPGs from the blending approach can add value for decision support.

Third, it is recommended to incorporate additional precipitation estimates from the blending approach in snow-dominated areas to reduce precipitation uncertainty in hydrologic applications. Given the importance of precipitation partitioning under climate warming and atmospheric rivers, the blending approach using the basin-scale wireless-sensor network and multiple types of measurements can complement the precipitation from operational gauges and gridded datasets, with a potential of providing alternative near-real-time data.

Supporting Information

The Supporting Information for this article can be found below.

References

Adam, J. C., & Lettenmaier, D. P. (2003). Adjustment of global gridded precipitation for systematic bias. *Journal of Geophysical Research: Atmospheres*, *108*(D9). https://doi.org/10.1029/2002JD002499

Arthern, R. J., Vaughan, D. G., Rankin, A. M., Mulvaney, R., & Thomas, E. R. (2010). In situ measurements of Antarctic snow compaction compared with predictions of models. *Journal of Geophysical Research: Earth Surface*, *115*(3), 1–12. https://doi.org/10.1029/2009JF001306

Avanzi, F., De Michele, C., Ghezzi, A., Jommi, C., & Pepe, M. (2014). A processing-modeling routine to use SNOTEL hourly data in snowpack dynamic models. *Advances in Water Resources*, *73*, 16–29. https://doi.org/10.1016/j.advwatres.2014.06.011

Avanzi, F., Rungee, J., Maurer, T., Bales, R., Ma, Q., Glaser, S., & Conklin, M. (2020a). Climate elasticity of evapotranspiration shifts the water balance of Mediterranean climates during multi-year droughts. *Hydrology and Earth System Sciences*, *24*(9), 4317–4337. https://doi.org/10.5194/hess-24-4317-2020

Avanzi, F., Zheng, Z., Coogan, A., Rice, R., Akella, R., & Conklin, M. H. (2020b). Gap-filling snow-depth time-series with Kalman Filtering-Smoothing and Expectation Maximization: Proof of concept using spatially dense wireless-sensor-network data. *Cold Regions Science and Technology*, *175*(July 2019), 103066. https://doi.org/10.1016/j.coldregions.2020.103066

Avanzi, F., Ercolani, G., Gabellani, S., Cremonese, E., Pogliotti, P., Filippa, G., et al. (2021). Learning about precipitation lapse rates from snow course data improves water balance modeling. *Hydrology and Earth System Sciences*, *25*(4), 2109–2131. https://doi.org/10.5194/hess-25-2109-2021

Bair, E. H., Davis, R. E., & Dozier, J. (2018). Hourly mass and snow energy balance measurements from Mammoth Mountain, CA USA, 2011-2017. *Earth System Science Data*, *10*(1), 549–563. https://doi.org/10.5194/essd-10-549-2018

Bales, R. C., Molotch, N. P., Painter, T. H., Dettinger, M. D., Rice, R., & Dozier, J. (2006). Mountain hydrology of the western United States. *Water Resources Research*, *42*(8), 1–13. https://doi.org/10.1029/2005WR004387

Bales, R. C., Guo, Q., Shen, D., McConnell, J. R., Du, G., Burkhart, J. F., et al. (2009). Annual accumulation for Greenland updated using ice core data developed during 2000-2006 and analysis of daily coastal meteorological data. *Journal of Geophysical Research Atmospheres*, *114*(6). https://doi.org/10.1029/2008JD011208

Bales, R. C., Stacy, E., Safeeq, M., Meng, X., Meadows, M., Oroza, C., et al. (2018). Spatially distributed water-balance and meteorological data from the rain–snow transition, southern Sierra Nevada, California. *Earth System Science Data*, *10*(4), 1795–1805. https://doi.org/10.5194/essd-10-1795-2018

Bales, R. C., Cui, G., Rice, R. R., Meng, X., Zhang, Z., Hartsough, P., et al. (2020). Snow depth, air temperature, humidity, soil moisture and temperature, and solar radiation data from the basin-scale wireless-sensor network in American River Hydrologic Observatory (ARHO). *UC Merced, Dataset*. https://doi.org/10.6071/M39Q2V

Behrangi, A., Bormann, K. J., & Painter, T. H. (2018a). Using the Airborne Snow Observatory to assess remotely sensed snowfall products in the California Sierra Nevada. *Water Resources Research*, *54*(10), 7331–7346. https://doi.org/10.1029/2018WR023108

Behrangi, A., Yin, X., Rajagopal, S., Stampoulis, D., & Ye, H. (2018b). On distinguishing snowfall from rainfall using near-surface atmospheric information: Comparative analysis, uncertainties and hydrologic importance. *Quarterly Journal of the Royal Meteorological Society*, *144*(S1), 89–102. https://doi.org/10.1002/qj.3240

Bohne, L., Strong, C., & Steenburgh, W. J. (2020). Climatology of orographic precipitation gradients in the contiguous western united states. *Journal of Hydrometeorology*, *21*(8), 1723–1740. https://doi.org/10.1175/JHM-D-19-0229.1

Brandt, W. T., Bormann, K. J., Cannon, F., Deems, J. S., Painter, T. H., Steinhoff, D. F., & Dozier, J. (2020). Quantifying the spatial variability of a snowstorm using differential airborne lidar. *Water Resources Research*, *56*(3), 1–22. https://doi.org/10.1029/2019WR025331

Breiman, L. (2001). Random forests. *Machine Learning*, *45*(1), 5–32. https://doi.org/10.1023/A:1010933404324

Brun-Laguna, K., Oroza, C., Zhang, Z., Malek, S., Watteyne, T., & Glaser, S. (2016). Sierranet: monitoring the snowpack in the Sierra Nevada: demo. In *Proceedings of the Eleventh ACM Workshop on Challenged Networks* (pp. 33–34). New York, New York, USA: ACM Press. https://doi.org/10.1145/2979683.2979698

Buytaert, W., Celleri, R., Willems, P., Bièvre, B. De, & Wyseure, G. (2006). Spatial and temporal rainfall variability in mountainous areas: A case study from the south Ecuadorian Andes. *Journal of Hydrology*, *329*(3–4), 413–421. https://doi.org/10.1016/j.jhydrol.2006.02.031

Carter, D. A., Gage, K. S., Ecklund, W. L., Angevine, W. M., Johnston, P. E., Riddle, A. C., et al. (1995). Developments in UHF lower tropospheric wind profiling at NOAA's Aeronomy Laboratory. *Radio Science*, *30*(4), 977–1001. https://doi.org/10.1029/95RS00649

Casellas, E., Bech, J., Veciana, R., Pineda, N., Rigo, T., Miró, J. R., & Sairouni, A. (2020). Surface precipitation phase discrimination in complex terrain. *Journal of Hydrology*, *592*, 125780. https://doi.org/10.1016/j.jhydrol.2020.125780

Cifelli, R., Chandrasekar, V., Lim, S., Kennedy, P. C., Wang, Y., & Rutledge, S. A. (2011). A new dual-polarization radar rainfall algorithm: Application in Colorado precipitation events. *Journal of Atmospheric and Oceanic Technology*, *28*(3), 352–364. https://doi.org/10.1175/2010JTECHA1488.1

Cleave, D. Van, Graham, R., Myrick, D., & Nordquist, M. (2019). *Snow Level in the NWS Western Region : Definition and Calculation Methodology*. Salt Lake City. Retrieved from https://www.weather.gov/media/wrh/online_publications/TAs/TA1901.pdf

Cocks, S. B., Tang, L., Zhang, P., Ryzhkov, A., Kaney, B., Elmore, K. L., et al. (2019). A prototype quantitative precipitation estimation algorithm for operational S-band polarimetric radar utilizing specific attenuation and specific differential phase. Part Ii: Performance verification and case study analysis. *Journal of Hydrometeorology*, *20*(5), 999–1014. https://doi.org/10.1175/JHM-D-18-0070.1

Cosgrove, B. A., Lohmann, D., Mitchell, K. E., Houser, P. R., Wood, E. F., Schaake, J. C., et al. (2003). Real-time and retrospective forcing in the North American Land Data Assimilation System (NLDAS) project. *Journal of Geophysical Research: Atmospheres*, *108*(D22). https://doi.org/10.1029/2002jd003118

Costa-Cabral, M., Coats, R., Reuter, J., Riverson, J., Sahoo, G., Schladow, G., et al. (2013). Climate variability and change in mountain environments: Some implications for water resources and water quality in the Sierra Nevada (USA). *Climatic Change*, *116*(1), 1–14. https://doi.org/10.1007/s10584-012-0630-2

Cui, G., Bales, R., Rice, R., Anderson, M., Avanzi, F., Hartsough, P., & Conklin, M. (2020). Detecting rain–snow-transition elevations in mountain basins using wireless sensor networks. *Journal of Hydrometeorology*, *21*(9), 2061–2081. https://doi.org/10.1175/JHM-D-20-0028.1

Dadic, R., Mott, R., Lehning, M., & Burlando, P. (2010). Wind influence on snow depth distribution and accumulation over glaciers. *Journal of Geophysical Research: Earth Surface*, *115*(1), 1–8. https://doi.org/10.1029/2009JF001261

Dai, Q., Yang, Q., Han, D., Rico-Ramirez, M. A., & Zhang, S. (2019). Adjustment of radar-gauge rainfall discrepancy due to raindrop drift and evaporation using the Weather Research and Forecasting model and dual-polarization radar. *Water Resources Research*, *55*(11), 9211–9233. https://doi.org/10.1029/2019WR025517

Daly, C., Neilson, R. P., & Phillips, D. L. (1994). A Statistical-Topographic Model for Mapping Climatological Precipitation over Mountainous Terrain. *Journal of Applied Meteorology*, *33*(2), 140–158. https://doi.org/10.1175/1520-0450(1994)033<0140:ASTMFM>2.0.CO;2

Daly, C., Halbleib, M., Smith, J. I., Gibson, W. P., Doggett, M. K., Taylor, G. H., et al. (2008). Physiographically sensitive mapping of climatological temperature and precipitation across the conterminous United States. *International Journal of Climatology*, *28*(15), 2031–2064. https://doi.org/10.1002/joc.1688

Dawdy, D. R., & Langbein, W. B. (1960). Mapping mean areal precipitation. *International Association of Scientific Hydrology. Bulletin*, *5*(3), 16–23. https://doi.org/10.1080/02626666009493176

Demaria, E. M. C., Dominguez, F., Hu, H., von Glinski, G., Robles, M., Skindlov, J., & Walter, J. (2017). Observed hydrologic impacts of landfalling atmospheric rivers in the Salt and Verde river basins of Arizona, United States. *Water Resources Research*, *53*(12), 10025–10042. https://doi.org/10.1002/2017WR020778

Denisko, D., & Hoffman, M. M. (2018). Classification and interaction in random forests. *Proceedings of the National Academy of Sciences*, *115*(8), 1690–1692. https://doi.org/10.1073/pnas.1800256115

Dettinger, M., Redmond, K., & Cayan, D. (2004). Winter orographic precipitation ratios in the Sierra Nevada—large-scale atmospheric circulations and hydrologic consequences. *Journal of Hydrometeorology*, *5*(6), 1102–1116. https://doi.org/10.1175/JHM-390.1

Dettinger, M. D., Ralph, F. M., Das, T., Neiman, P. J., & Cayan, D. R. (2011). Atmospheric rivers, floods and the water resources of California. *Water*, *3*(2), 445–478. https://doi.org/10.3390/w3020445

Ding, B., Yang, K., Qin, J., Wang, L., Chen, Y., & He, X. (2014). The dependence of precipitation types on surface elevation and meteorological conditions and its parameterization. *Journal of Hydrology*, *513*, 154–163. https://doi.org/10.1016/j.jhydrol.2014.03.038

Elder, K., Dozier, J., & Michaelsen, J. (1991). Snow accumulation and distribution in an Alpine Watershed. *Water Resources Research*, *27*(7), 1541–1552. https://doi.org/10.1029/91WR00506

Elder, K., Rosenthal, W., & Davis, R. E. (1998). Estimating the spatial distribution of snow water equivalence in a montane watershed. *Hydrological Processes*, *12*(10–11), 1793–1808. https://doi.org/10.1002/(SICI)1099-1085(199808/09)12:10/11<1793::AID-HYP695>3.0.CO;2-K

Fontaine, T. A., Cruickshank, T. S., Arnold, J. G., & Hotchkiss, R. H. (2002). Development of a snowfall-snowmelt routine for mountainous terrain for the soil water assessment tool (SWAT). *Journal of Hydrology*, *262*(1–4), 209–223. https://doi.org/10.1016/S0022-1694(02)00029-X

Gelaro, R., McCarty, W., Suárez, M. J., Todling, R., Molod, A., Takacs, L., et al. (2017). The modern-era retrospective analysis for research and applications, version 2 (MERRA-2). *Journal of Climate*, *30*(14), 5419–5454. https://doi.org/10.1175/JCLI-D-16-0758.1

Goldenson, N., Leung, L. R. R., Bitz, C. M. M., & Blanchard-Wrigglesworth, E. (2018). Influence of Atmospheric Rivers on mountain snowpack in the Western United States. *Journal of Climate*, *31*(24), 9921–9940. https://doi.org/10.1175/JCLI-D-18-0268.1

Gourley, J. J., Jorgensen, D. P., Matrosov, S. Y., & Flamig, Z. L. (2009). Evaluation of incremental improvements to quantitative precipitation estimates in complex terrain. *Journal of Hydrometeorology*, *10*(6), 1507–1520. https://doi.org/10.1175/2009JHM1125.1

Grossi, G., Lendvai, A., Peretti, G., & Ranzi, R. (2017). Snow Precipitation Measured by Gauges: Systematic Error Estimation and Data Series Correction in the Central Italian Alps. *Water*, *9*(7), 461. https://doi.org/10.3390/w9070461

He, M., Russo, M., Anderson, M., Fickenscher, P., Whitin, B., Schwarz, A., & Lynn, E. (2018). Changes in extremes of temperature, precipitation, and Runoff in California's Central Valley During 1949-2010. *Hydrology*, *5*(1), 1–26. https://doi.org/10.3390/hydrology5010001

Hedstrom, N. R., & Pomeroy, J. W. (1998). Measurements and modelling of snow interception in the boreal forest. *Hydrological Processes*, *12*(10–11), 1611–1625. https://doi.org/10.1002/(SICI)1099-1085(199808/09)12:10/11<1611::AID-HYP684>3.0.CO;2-4

Henn, B., Clark, M. P., Kavetski, D., & Lundquist, J. D. (2015). Estimating mountain basin-mean precipitation from streamflow using Bayesian inference. *Water Resources Research*, *51*(10), 8012–8033. https://doi.org/10.1002/2014WR016736

Henn, B., Newman, A. J., Livneh, B., Daly, C., & Lundquist, J. D. (2018). An assessment of differences in gridded precipitation datasets in complex terrain. *Journal of Hydrology*, *556*, 1205–1219. https://doi.org/10.1016/j.jhydrol.2017.03.008

Hofstra, N., Haylock, M., New, M., & Jones, P. D. (2009). Testing E-OBS European high-resolution gridded data set of daily precipitation and surface temperature. *Journal of Geophysical*

Research Atmospheres, *114*(21). https://doi.org/10.1029/2009JD011799

Huber, P. J. (1973). Robust Regression: Asymptotics, Conjectures and Monte Carlo. *The Annals of Statistics*, *1*(5), 799–821. https://doi.org/10.1214/aos/1176342503

Hughes, M., Neiman, P. J., Sukovich, E., & Ralph, M. (2012). Representation of the Sierra Barrier Jet in 11 years of a high-resolution dynamical reanalysis downscaling compared with long-term wind profiler observations. *Journal of Geophysical Research Atmospheres*, *117*(17), 1–18. https://doi.org/10.1029/2012JD017869

Huning, L. S., & Margulis, S. A. (2017). Climatology of seasonal snowfall accumulation across the Sierra Nevada (USA): Accumulation rates, distributions, and variability. *Water Resources Research*, *53*(7), 6033–6049. https://doi.org/10.1002/2017WR020915

Huning, L. S., & Margulis, S. A. (2018). Investigating the variability of high-elevation seasonal orographic snowfall enhancement and its drivers across sierra nevada, California. *Journal of Hydrometeorology*, *19*(1), 47–67. https://doi.org/10.1175/JHM-D-16-0254.1

Immerzeel, W. W., Petersen, L., Ragettli, S., & Pellicciotti, F. (2014). The importance of observed gradients of air temperature and precipitation for modeling runoff from a glacierized watershed in the Nepalese Himalayas. *Water Resources Research*, *50*(3), 2212–2226. https://doi.org/10.1002/2013WR014506

Johnston, P. E., Jordan, J. R., White, A. B., Carter, D. A., Costa, D. M., & Ayers, T. E. (2017). The NOAA FM-CW snow-level radar. *Journal of Atmospheric and Oceanic Technology*, *34*(2), 249–267. https://doi.org/10.1175/JTECH-D-16-0063.1

Jordan, R. (1991). A One-Dimensional Temperature Model for a Snow Cover: Technical Documentation for SNTHERM.89. *U.S.Army Corps of Engineers, Cold Regions Research & Engineering Laboratory*, (Special Report 91-16), 49.

Judson Arthur, & Doesken Nolan. (2000). Density of freshly fallen snow in the central Rocky Mountains. *Bulletin of the American Meteorological Society*, *81*(7), 1577–1588. https://doi.org/10.1175/1520-0477(2000)081<1577:DOFFSI>2.3.CO;2

Kirchner, P. B., Bales, R. C., Molotch, N. P., Flanagan, J., & Guo, Q. (2014). LiDAR measurement of seasonal snow accumulation along an elevation gradient in the southern Sierra Nevada, California. *Hydrology and Earth System Sciences*, *18*(10), 4261–4275. https://doi.org/10.5194/hess-18-4261-2014

Koch, J., Stisen, S., Refsgaard, J. C., Ernstsen, V., Jakobsen, P. R., & Højberg, A. L. (2019). Modeling depth of the redox interface at high resolution at national scale using random forest and residual gaussian simulation. *Water Resources Research*, *55*(2), 1451–1469. https://doi.org/10.1029/2018WR023939

Kochendorfer, J., Earle, M. E., Hodyss, D., Reverdin, A., Roulet, Y. A., Nitu, R., et al. (2020). Undercatch adjustments for tipping-bucket gauge measurements of solid precipitation. *Journal of Hydrometeorology*, *21*(6), 1193–1205. https://doi.org/10.1175/JHM-D-19-0256.1

Krajewski, W. F., Villarini, G., & Smith, J. A. (2010). Radar-rainfall uncertainties:Where are we after thirty years of effort. *Bulletin of the American Meteorological Society*, *91*(1), 87–94. https://doi.org/10.1175/2009BAMS2747.1

Kursa, M. B., & Rudnicki, W. R. (2010). Feature selection with the boruta package. *Journal of Statistical Software*, *36*(11), 1–13. https://doi.org/10.18637/jss.v036.i11

Langham, E. J., Santeford, H. S., & Smith, J. L. (1974). The occurrence and movement of liquid water in the snowpack. In *Symposium on Advanced Concepts in the Study of Snow and Ice Resources, National Academy of Sciences*.

Lavers, D. A., & Villarini, G. (2015). The contribution of atmospheric rivers to precipitation in Europe and the United States. *Journal of Hydrology*, *522*, 382–390. https://doi.org/10.1016/j.jhydrol.2014.12.010

Lavers, D. A., Waliser, D. E., Ralph, F. M., & Dettinger, M. D. (2016). Predictability of horizontal water vapor transport relative to precipitation: Enhancing situational awareness for forecasting western U.S. extreme precipitation and flooding. *Geophysical Research Letters*, *43*(5), 2275–2282. https://doi.org/10.1002/2016GL067765

Lavers, D. A., Zsoter, E., Richardson, D. S., & Pappenberger, F. (2017). An assessment of the ECMWF extreme forecast index for water vapor transport during boreal winter. *Weather and Forecasting*, *32*(4), 1667–1674. https://doi.org/10.1175/WAF-D-17-0073.1

Lavers, D. A., Richardson, D. S., Ramos, A. M., Zsoter, E., Pappenberger, F., & Trigo, R. M. (2018). Earlier awareness of extreme winter precipitation across the western Iberian Peninsula. *Meteorological Applications*, *25*(4), 622–628. https://doi.org/10.1002/met.1727

Lawrence, M. G. (2005). The relationship between relative humidity and the dewpoint temperature in moist air: A simple conversion and applications. *Bulletin of the American Meteorological Society*, *86*(2), 225–234. https://doi.org/10.1175/BAMS-86-2-225

Lundquist, J. D., Neiman, P. J., Martner, B., White, A. B., Gottas, D. J., & Ralph, F. M. (2008). Rain versus snow in the Sierra Nevada, California: Comparing Doppler profiling radar and surface observations of melting level. *Journal of Hydrometeorology*, *9*(2), 194–211. https://doi.org/10.1175/2007JHM853.1

Lundquist, J. D., Minder, J. R., Neiman, P. J., & Sukovich, E. (2010). Relationships between Barrier Jet Heights, Orographic Precipitation Gradients, and Streamflow in the Northern Sierra Nevada. *Journal of Hydrometeorology*, *11*(5), 1141–1156. https://doi.org/10.1175/2010JHM1264.1

Lundquist, J. D., Hughes, M., Henn, B., Gutmann, E. D., Livneh, B., Dozier, J., & Neiman, P. (2015). High-elevation precipitation patterns: Using snow measurements to assess daily gridded datasets across the Sierra Nevada, California. *Journal of Hydrometeorology*, *16*(4), 1773–1792. https://doi.org/10.1175/JHM-D-15-0019.1

Lundquist, J. D., Hughes, M., Gutmann, E., & Kapnick, S. (2019). Our skill in modeling mountain rain and snow is bypassing the skill of our observational networks. *Bulletin of the American Meteorological Society*, *100*(12), 2473–2490. https://doi.org/10.1175/BAMS-D-19-0001.1

MacDougall, A. H., Wheler, B. A., & Flowers, G. E. (2011). A preliminary assessment of glacier melt-model parameter sensitivity and transferability in a dry subarctic environment. *Cryosphere*, *5*(4), 1011–1028. https://doi.org/10.5194/tc-5-1011-2011

Mair, E., Leitinger, G., Della Chiesa, S., Niedrist, G., Tappeiner, U., & Bertoldi, G. (2016). A simple method to combine snow height and meteorological observations to estimate winter precipitation at sub-daily resolution. *Hydrological Sciences Journal*, *61*(11), 2050–2060. https://doi.org/10.1080/02626667.2015.1081203

Malek, S. A., Avanzi, F., Brun-Laguna, K., Maurer, T., Oroza, C. A., Hartsough, P. C., et al. (2017). Real-time alpine measurement system using wireless sensor networks. *Sensors (Switzerland)*, *17*(11), 1–30. https://doi.org/10.3390/s17112583

Malek, S. A., Glaser, S. D., & Bales, R. C. (2019). Wireless Sensor Networks for improved snow water equivalent and runoff estimates. *IEEE Access*, *7*, 18420–18436. https://doi.org/10.1109/ACCESS.2019.2895397

Margulis, S. A., Cortés, G., Girotto, M., & Durand, M. (2016). A Landsat-era Sierra Nevada snow reanalysis (1985–2015). *Journal of Hydrometeorology*, *17*(4), 1203–1221. https://doi.org/10.1175/JHM-D-15-0177.1

Marks, D., Winstral, A., Reba, M., Pomeroy, J., & Kumar, M. (2013). An evaluation of methods for determining during-storm precipitation phase and the rain/snow transition elevation at the surface in a mountain basin. *Advances in Water Resources*, *55*, 98–110. https://doi.org/10.1016/j.advwatres.2012.11.012

Markstrom, S. L., Regan, R. S., Hay, L. E., Viger, R. J., Webb, R. M. T., Payn, R. A., & LaFontaine, J. H. (2015). *PRMS-IV, the precipitation-runoff modeling system, version 4*. *US Geological Survey Techniques and Methods*. https://doi.org/10.3133/tm6B7

Marshall, H. P., Conway, H., & Rasmussen, L. A. (1999). Snow densification during rain. *Cold Regions Science and Technology*, *30*(1–3), 35–41. https://doi.org/10.1016/S0165-232X(99)00011-7

Marwitz, J. D. (1983). The kinematics of orographic airflow during Sierra storms. *Journal of the Atmospheric Sciences*. https://doi.org/10.1175/1520-0469(1983)040<1218:TKOOAD>2.0.CO;2

Matrosov, S. Y., Clark, K. A., & Kingsmill, D. E. (2007). A polarimetric radar approach to identify rain, melting-layer, and snow regions for applying corrections to vertical profiles of reflectivity. *Journal of Applied Meteorology and Climatology*, *46*(2), 154–166. https://doi.org/10.1175/JAM2508.1

McCabe, G. J., Clark, M. P., & Hay, L. E. (2007). Rain-on-snow events in the western United States. *Bulletin of the American Meteorological Society*, *88*(3), 319–328. https://doi.org/10.1175/BAMS-88-3-319

McGurk, B., Azuma, D., & Kattelmann, R. (1988). Density of new snow in the central Sierra Nevada. In *Proceedings of the 56th Annual Western Snow Conference* (pp. 158–161). Retrieved from https://westernsnowconference.org/sites/westernsnowconference.org/PDFs/1988McGurk.pdf

Morin, E., Goodrich, D. C., Maddox, R. A., Gao, X., Gupta, H. V., & Sorooshian, S. (2006). Spatial patterns in thunderstorm rainfall events and their coupling with watershed hydrological response. *Advances in Water Resources*, *29*(6), 843–860. https://doi.org/10.1016/j.advwatres.2005.07.014

Neiman, P. J., Sukovich, E. M., Martin Ralph, F., & Hughes, M. (2010). A seven-year wind profiler-based climatology of the windward barrier jet along California's Northern Sierra Nevada. *Monthly Weather Review*, *138*(4), 1206–1233. https://doi.org/10.1175/2009MWR3170.1

Neiman, P. J., Hughes, M., Moore, B. J., Martin Ralph, F., & Sukovich, E. M. (2013). Sierra barrier jets, atmospheric rivers, and precipitation characteristics in northern California: A composite perspective based on a network of wind profilers. *Monthly Weather Review*, *141*(12), 4211–4233. https://doi.org/10.1175/MWR-D-13-00112.1

Niu, G. Y., Yang, Z. L., Mitchell, K. E., Chen, F., Ek, M. B., Barlage, M., et al. (2011). The community Noah land surface model with multiparameterization options (Noah-MP): 1. Model description and evaluation with local-scale measurements. *Journal of Geophysical Research Atmospheres*, *116*(12), 1–19. https://doi.org/10.1029/2010JD015139

Olsen, A. (2003). *Snow or rain ? - A matter of wet-bulb temperature*. Retrieved from https://www.diva-portal.org/smash/get/diva2:968860/FULLTEXT01.pdf

Painter, T. H., Berisford, D. F., Boardman, J. W., Bormann, K. J., Deems, J. S., Gehrke, F., et al. (2016). The Airborne Snow Observatory: Fusion of scanning lidar, imaging spectrometer, and physically-based modeling for mapping snow water equivalent and snow albedo. *Remote Sensing of Environment*, *184*, 139–152. https://doi.org/10.1016/j.rse.2016.06.018

Pan, M., & Lu, M. (2019). A novel Atmospheric River identification algorithm. *Water Resources Research*, *55*(7), 6069–6087. https://doi.org/10.1029/2018WR024407

Pandey, G. R., Cayan, D. R., & Georgakakos, K. P. (1999). Precipitation structure in the Sierra Nevada of California during winter. *Journal of Geophysical Research: Atmospheres*, *104*(D10), 12019–12030. https://doi.org/10.1029/1999JD900103

Pomeroy, J. W., & Goodison, B. E. (1997). *Winter and snow*. (T. R. Oke, W. R. Rouse, & W. G. Bailey, Eds.), *The surface climates of Canada*. McGill-Queen's University Press Montreal.

Qi, Y., Zhang, J., Zhang, P., & Cao, Q. (2013). VPR correction of bright band effects in radar QPEs using polarimetric radar observations. *Journal of Geophysical Research: Atmospheres*, *118*(9), 3627–3633. https://doi.org/10.1002/jgrd.50364

Raleigh, M. S., & Lundquist, J. D. (2012). Comparing and combining SWE estimates from the SNOW-17 model using PRISM and SWE reconstruction. *Water Resources Research*, *48*(1), 1–16. https://doi.org/10.1029/2011WR010542

Ralph, F. M., Sukovich, E., Reynolds, D., Dettinger, M., Weagle, S., Clark, W., & Neiman, P. J. (2010). Assessment of extreme quantitative precipitation forecasts and development of regional extreme event thresholds using data from HMT-2006 and COOP observers. *Journal of Hydrometeorology*, *11*(6), 1286–1304. https://doi.org/10.1175/2010JHM1232.1

Ralph, F Martin, Rutz, J. J., Cordeira, J. M., Dettinger, M., Anderson, M., Reynolds, D., et al. (2019). A Scale to Characterize the Strength and Impacts of Atmospheric Rivers. *Bulletin of the American Meteorological Society*, *100*(2), 269–289. https://doi.org/10.1175/BAMS-D-18-0023.1

Ralph, M., Cordeira, J. M., Neiman, P. J., & Hughes, M. (2016). Landfalling atmospheric rivers, the Sierra barrier jet, and extreme daily precipitation in Northern California's Upper Sacramento River watershed. *Journal of Hydrometeorology*, *17*(7), 1905–1914. https://doi.org/10.1175/JHM-D-15-0167.1

Rasmussen, R., Baker, B., Kochendorfer, J., Meyers, T., Landolt, S., Fischer, A. P., et al. (2012). How well are we measuring snow: The NOAA/FAA/NCAR winter precipitation test bed. *Bulletin of the American Meteorological Society*, *93*(6), 811–829. https://doi.org/10.1175/BAMS-D-11-00052.1

Roche, J. W., Rice, R., Meng, X., Cayan, D. R., Dettinger, M. D., Alden, D., et al. (2019). Climate, snow, and soil moisture data set for the Tuolumne and Merced river watersheds, California, USA. *Earth System Science Data*, *11*(1), 101–110. https://doi.org/10.5194/essd-11-101-2019

Ryan, W. A., Doesken, N. J., & Fassnacht, S. R. (2008). Evaluation of ultrasonic snow depth sensors for U.S. snow measurements. *Journal of Atmospheric and Oceanic Technology*, *25*(5), 667–684. https://doi.org/10.1175/2007JTECHA947.1

Seo, B. C., Dolan, B., Krajewski, W. F., Rutledge, S. A., & Petersen, W. (2015). Comparison of single- and dual-polarization-based rainfall estimates using NEXRAD data for the NASA Iowa flood studies project. *Journal of Hydrometeorology*, *16*(4), 1658–1675. https://doi.org/10.1175/JHM-D-14-0169.1

Sharma, S., Isik, S., Srivastava, P., & Kalin, L. (2012). Deriving spatially distributed precipitation data using the artificial neural network and multilinear regression models. *Journal of Hydrologic Engineering*, *18*(2), 194–205. https://doi.org/10.1061/(asce)he.1943-5584.0000617

Siler, N., & Roe, G. (2014). How will orographic precipitation respond to surface warming? An idealized thermodynamic perspective. *Geophysical Research Letters*, *41*(7), 2606–2613. https://doi.org/10.1002/2013GL059095

Sims, E. M., & Liu, G. (2015). A parameterization of the probability of snow–rain transition. *Journal of Hydrometeorology*, *16*(4), 1466–1477. https://doi.org/10.1175/JHM-D-14-0211.1

Smith, B. L., Yuter, S. E., Neiman, P. J., & Kingsmill, D. E. (2010). Water vapor fluxes and orographic precipitation over northern california associated with a landfalling atmospheric river. *Monthly Weather Review*, *138*(1), 74–100. https://doi.org/10.1175/2009MWR2939.1

Smith, R. B., & Barstad, I. (2004). A linear theory of orographic precipitation. *Journal of the Atmospheric Sciences*, *61*(12), 1377–1391. https://doi.org/10.1175/1520-0469(2004)061<1377:ALTOOP>2.0.CO;2

Stigter, E. E., Litt, M., Steiner, J. F., Bonekamp, P. N. J., Shea, J. M., Bierkens, M. F. P., & Immerzeel, W. W. (2018). The Importance of Snow Sublimation on a Himalayan Glacier. *Frontiers in Earth Science*, *6*(August), 1–16. https://doi.org/10.3389/feart.2018.00108

Stisen, S., Hojberg, A. L., Troldborg, L., Refsgaard, J. C., Christensen, B. S. B., Olsen, M., & Henriksen, H. J. (2012). On the importance of appropriate precipitation gauge catch correction for hydrological modelling at mid to high latitudes. *Hydrology and Earth System Sciences*, *16*(11), 4157–4176. https://doi.org/10.5194/hess-16-4157-2012

Strangeways, I. C. (1996). Back to basics: The 'met. enclosure': Part 2(b) - Raingauges, their errors. *Weather*, *51*(9), 298–303. https://doi.org/10.1002/j.1477-8696.1996.tb06230.x

Sumargo, E., Cannon, F., Ralph, F. M., & Henn, B. (2020). Freezing Level Forecast Error Can Consume Reservoir Flood Control Storage: Potentials for Lake Oroville and New Bullards Bar Reservoirs in California. *Water Resources Research*, *56*(8). https://doi.org/10.1029/2020WR027072

Susong, D., Marks, D., & Garen, D. (1999). Methods for developing time-series climate surfaces to drive topographically distributed energy- and water-balance models. *Hydrological Processes*, *13*(12–13), 2003–2021. https://doi.org/10.1002/(sici)1099-1085(199909)13:12/13<2003::aid-hyp884>3.0.co;2-k

Tamang, S. K., Ebtehaj, A. M., Prein, A. F., & Heymsfield, A. J. (2020). Linking global changes of snowfall and wet-bulb temperature. *Journal of Climate*, *33*(1), 39–59. https://doi.org/10.1175/jcli-d-19-0254.1

Thornton, P. E., Running, S. W., & White, M. A. (1997). Generating surfaces of daily meteorological variables over large regions of complex terrain. *Journal of Hydrology*, *190*(3–4), 214–251. https://doi.org/10.1016/S0022-1694(96)03128-9

Vetter, T., Huang, S., Aich, V., Yang, T., Wang, X., Krysanova, V., & Hattermann, F. (2015). Multi-model climate impact assessment and intercomparison for three large-scale river basins on three continents. *Earth System Dynamics*, *6*(1), 17–43. https://doi.org/10.5194/esd-6-17-2015

Vignal, B., Galli, G., Joss, J., & Germann, U. (2000). Three methods to determine profiles of reflectivity from volumetric radar data to correct precipitation estimates. *Journal of Applied Meteorology*, *39*(10), 1715–1726. https://doi.org/10.1175/1520-0450-39.10.1715

Wang, L., Zhang, F., Zhang, H., Scott, C. A., Zeng, C., & Shi, X. (2018). Intensive precipitation observation greatly improves hydrological modelling of the poorly gauged high mountain Mabengnong catchment in the Tibetan Plateau. *Journal of Hydrology*, *556*, 500–509. https://doi.org/10.1016/j.jhydrol.2017.11.039

Wang, Y. H., Broxton, P., Fang, Y., Behrangi, A., Barlage, M., Zeng, X., & Niu, G. Y. (2019). A wet-bulb temperature-based rain-snow partitioning scheme improves snowpack prediction over the drier western United States. *Geophysical Research Letters*, *46*(23), 13825–13835. https://doi.org/10.1029/2019GL085722

Wayand, N. E., Clark, M. P., & Lundquist, J. D. (2017). Diagnosing snow accumulation errors in a rain-snow transitional environment with snow board observations. *Hydrological Processes*, *31*(2), 349–363. https://doi.org/10.1002/hyp.11002

Welch, S. C., Kerkez, B., Bales, R. C., Glaser, S. D., Rittger, K., & Rice, R. R. (2013). Sensor placement strategies for snow water equivalent (SWE) estimation in the American River basin. *Water Resources Research*, *49*(2), 891–903. https://doi.org/10.1002/wrcr.20100

Westrick, K. J., Mass, C. F., & Colle, B. A. (1999). The limitations of the WSR-88D radar network for quantitative precipitation measurement over the coastal western United States. *Bulletin of the American Meteorological Society*, *80*(11), 2289–2298. https://doi.org/10.1175/1520-0477(1999)080<2289:TLOTWR>2.0.CO;2

White, A. B., Gottas, D. J., Strem, E. T., Ralph, F. M., & Neiman, P. J. (2002). An automated brightband height detection algorithm for use with Doppler radar spectral moments. *Journal of Atmospheric and Oceanic Technology*, *19*(5), 687–697. https://doi.org/10.1175/1520-0426(2002)019<0687:AABHDA>2.0.CO;2

White, A. B., Gottas, D. J., Henkel, A. F., Neiman, P. J., Ralph, F. M., & Gutman, S. I. (2010). Developing a performance measure for snow-level forecasts. *Journal of Hydrometeorology*, *11*(3), 739–753. https://doi.org/10.1175/2009JHM1181.1

Wiese, M., & Schneebeli, M. (2017). Early-stage interaction between settlement and temperature-gradient metamorphism. *Journal of Glaciology*, *63*(240), 652–662. https://doi.org/10.1017/jog.2017.31

Willie, D., Chen, H., Chandrasekar, V., Cifelli, R., Campbell, C., Reynolds, D., et al. (2017). Evaluation of multisensor quantitative precipitation estimation in Russian river basin. *Journal of Hydrologic Engineering*, *22*(5), 1–11. https://doi.org/10.1061/(ASCE)HE.1943-5584.0001422

Winstral, A., & Marks, D. (2002). Simulating wind fields and snow redistribution using terrain-based parameters to model snow accumulation and melt over a semi-arid mountain catchment. *Hydrological Processes*, *16*(18), 3585–3603. https://doi.org/10.1002/hyp.1238

Woldemichael, A. T., Hossain, F., Pielke, R., & Beltrán-Przekurat, A. (2012). Understanding the impact of dam-triggered land use/land cover change on the modification of extreme precipitation. *Water Resources Research*, *48*(9). https://doi.org/10.1029/2011WR011684

Xia, Y., Mitchell, K., Ek, M., Sheffield, J., Cosgrove, B., Wood, E., et al. (2012). Continental-scale water and energy flux analysis and validation for the North American Land Data Assimilation System project phase 2 (NLDAS-2): 1. Intercomparison and application of model products. *Journal of Geophysical Research Atmospheres*, *117*(3). https://doi.org/10.1029/2011JD016048

Yang, D., Goodison, B. E., Ishida, S., & Benson, C. S. (1998). Adjustment of daily precipitation data at 10 climate stations in Alaska: Application of World Meteorological Organization intercomparison results. *Water Resources Research*, *34*(2), 241–256. https://doi.org/10.1029/97WR02681

Yang, D., Ishida, S., Goodison, B. E., & Gunther, T. (1999). Bias correction of daily precipitation measurements for Greenland. *Journal of Geophysical Research: Atmospheres*, *104*(D6), 6171–6181. https://doi.org/10.1029/1998JD200110

Yang, D., Kane, D., Zhang, Z., Legates, D., & Goodison, B. (2005). Bias corrections of long-term (1973-2004) daily precipitation data over the northern regions. *Geophysical Research Letters*, *32*(19), 1–5. https://doi.org/10.1029/2005GL024057

Zhang, J., Qi, Y., Kingsmill, D., & Howard, K. (2012). Radar-based quantitative precipitation estimation for the cool season in complex terrain: Case studies from the NOAA hydrometeorology testbed. *Journal of Hydrometeorology*, *13*(6), 1836–1854. https://doi.org/10.1175/JHM-D-11-0145.1

Zhang, J., Howard, K., Langston, C., Kaney, B., Qi, Y., Tang, L., et al. (2016). Multi-Radar Multi-Sensor (MRMS) quantitative precipitation estimation: Initial operating capabilities. *Bulletin of the American Meteorological Society*, *97*(4), 621–638. https://doi.org/10.1175/BAMS-D-14-00174.1

Zhang, J., Tang, L., Cocks, S., Zhang, P., Ryzhkov, A., Howard, K., et al. (2020). A dual-polarization radar synthetic QPE for operations. *Journal of Hydrometeorology*, *21*(11), 2507–2521. https://doi.org/10.1175/JHM-D-19-0194.1

Zhang, Z., Glaser, S., Bales, R., Conklin, M., Rice, R., & Marks, D. (2017a). Insights into mountain precipitation and snowpack from a basin-scale wireless-sensor network. *Water Resources*

Research, *53*(8), 6626–6641. https://doi.org/10.1002/2016WR018825

Zhang, Z., Glaser, S. D., Bales, R. C., Conklin, M., Rice, R., & Marks, D. G. (2017b). Technical report: The design and evaluation of a basin-scale wireless sensor network for mountain hydrology. *Water Resources Research*, *53*(5), 4487–4498. https://doi.org/10.1002/2016WR019619

Zhang, Ziran, Glaser, S., Watteyne, T., & Malek, S. (2020). Long-term monitoring of the Sierra Nevada snowpack using Wireless Sensor Networks. *IEEE Internet of Things Journal*. https://doi.org/10.1109/JIOT.2020.2970596

Zheng, Z., Molotch, N. P., Oroza, C. A., Conklin, M. H., & Bales, R. C. (2018). Spatial snow water equivalent estimation for mountainous areas using wireless-sensor networks and remote-sensing products. *Remote Sensing of Environment*, *215*, 44–56. https://doi.org/10.1016/j.rse.2018.05.029

Zhong, K., Zheng, F., Xu, X., & Qin, C. (2018). Discriminating the precipitation phase based on different temperature thresholds in the Songhua River Basin, China. *Atmospheric Research*, *205*, 48–59. https://doi.org/10.1016/j.atmosres.2018.02.002

Tables and Figures

Table 1. Wireless-sensor clusters in the upper American River basin.

Wireless-sensor cluster	Abbr.	Lat, °	Lon, °	Elevation range, m	Slope, °	Aspect, °	Canopy cover, %
Schneiders	SCN	38.745	-120.068	2634-2723	11	207	36
Echo Peak	ECP	38.851	-120.075	2306-2607	16	179	22
Mt Lincoln	MTL	39.286	-120.325	2388-2544	17	160	11
Caples Lake	CAP	38.711	-120.042	2428-2446	6	214	50
Alpha	ALP	38.805	-120.214	2206-2317	13	229	37
Duncan Peak	DUN	39.152	-120.511	2049-2130	15	265	43
Van Vleck	VVL	38.943	-120.309	2046-2087	7	119	48
Dolly Rice	DOR	39.149	-120.371	1952-2003	9	281	55
Onion Creek	ONN	39.276	-120.358	1849-1939	11	234	49
Robbs Saddle	RBB	38.913	-120.379	1782-1834	7	141	48
Talbot Camp	TLC	39.191	-120.377	1723-1751	7	142	58
Owens Camp	OWC	38.736	-120.242	1566-1600	10	201	38
Bear Trap	BTP	39.093	-120.577	1510-1622	15	187	57

Note: Values of each cluster were averaged by all nodes within the cluster, except for the elevation column showing the elevation range of all nodes. Elevation, slope, and aspect were derived using Digital Elevation Model (DEM) with a spatial resolution of 30 m from the National Elevation Dataset (NED), and canopy cover was obtained from the National Land Cover Database (NLCD).

Table 2. Precipitation gauges and snow pillows from operational stations on CDEC.

Station ID	Gauge	Tipping bucket	Wind adjusted	Snow pillow	Lat, °	Lon, °	Elevation, m
LOS				x	38.921	-120.204	2621
CXS	x			x	38.692	-120.002	2546
SQV	x			x	39.194	-120.276	2499
EP5	x			x	38.849	-120.079	2473
FDC	x			x	38.682	-119.960	2444
CAP	x	x	x	x	38.710	-120.042	2438
FRN	x	x	x	x	38.805	-120.213	2316
RP2	x			x	39.001	-120.140	2286
MFT	x				38.894	-120.276	2167
SIL	x			x	38.678	-120.118	2164
DUN	x		x		39.144	-120.509	2164

CSL				x	39.325	-120.367	2103
WC3	x			x	39.136	-120.219	2057
HYS	x	x		x	39.282	-120.527	2012
LON	x				38.983	-120.323	1954
GKS	x	x		x	39.075	-120.558	1707
BLC	x	x		x	39.280	-120.709	1609
BTP	x		x		39.095	-120.577	1590
OWC	x		x		38.733	-120.245	1586
HLH	x		x		39.072	-120.422	1396
SOM	x				39.091	-120.732	1311
SGP	x	x			39.124	-120.761	1171
PFH	x	x			38.759	-120.508	1049
PCF	x				38.765	-120.500	1036
GTW	x	x			38.925	-120.790	991
PWS	x	x	x		38.695	-120.824	566
SLB	x				38.773	-120.699	564
PCV	x				38.700	-120.820	564
PIH	x		x		38.832	-121.009	366
ADR	x	x			38.882	-121.045	366
NCS	x	x			38.874	-121.135	271
FOL	x				38.683	-121.183	142
FLD	x		x		38.693	-121.130	107
PRC	x				38.592	-121.161	95
ORN	x				38.687	-121.219	72
CHG	x	x			38.652	-121.254	64
LCN	x		x		38.882	-121.272	61
RSV	x				38.760	-121.315	46
RNC	x	x			38.603	-121.312	22
RLN	x				38.698	-121.449	14
ARW	x	x			38.596	-121.413	11
HRY	x				38.587	-121.405	11
CSU	x	x			38.555	-121.416	8

Table 3. Orographic Precipitation Gradients (OPG α, unit km^{-1}) for aggregated precipitation events in WY2014-2017 based on the occurrences of Atmospheric River (AR) and Sierra Barrier Jet (SBJ). High SBJ event is defined as precipitation event with SBJ height ≥ 1000 m, and low SBJ event with SBJ height < 1000 m. Non-AR stands for the event that is not associated with AR, and Non-SBJ for the event not associated with SBJ.

Event Category (event count)	Upper Basin (≥1500 m)						Lower Basin (<1500 m)	
	Sensor liquid	Sensor solid	Pillow solid	Sensor total	Gauge total	PRISM total	Gauge total	PRISM total
AR & SBJ (21)	-0.94	1.58	1.20	0.17	-0.48	-0.20	1.09	0.80
Non-AR & Non-SBJ (20)	-0.56	1.58	1.40	0.24	-0.05	-0.06	1.09	0.73
AR & Non-SBJ (10)	-1.04	0.86	0.36	0.39	-0.47	-0.11	1.57	1.03
Non-AR & SBJ (6)	-1.26	0.59	0.57	0.29	-0.61	-0.28	0.76	0.53
AR (34)	-0.95	1.45	1.07	0.22	-0.48	-0.17	1.15	0.82
Non-AR (26)	-0.61	1.23	0.60	0.28	-0.22	-0.11	0.98	0.67
SBJ (27)	-0.94	1.46	0.61	0.17	-0.50	-0.20	1.09	0.77
Non-SBJ (30)	-0.70	1.18	0.58	0.29	-0.34	-0.09	1.25	0.88
High-SBJ (13)	-0.95	1.99	1.11	0.30	-0.60	-0.25	0.92	0.61
Low-SBJ (14)	-0.90	1.29	0.61	0.15	-0.42	-0.17	1.18	0.88
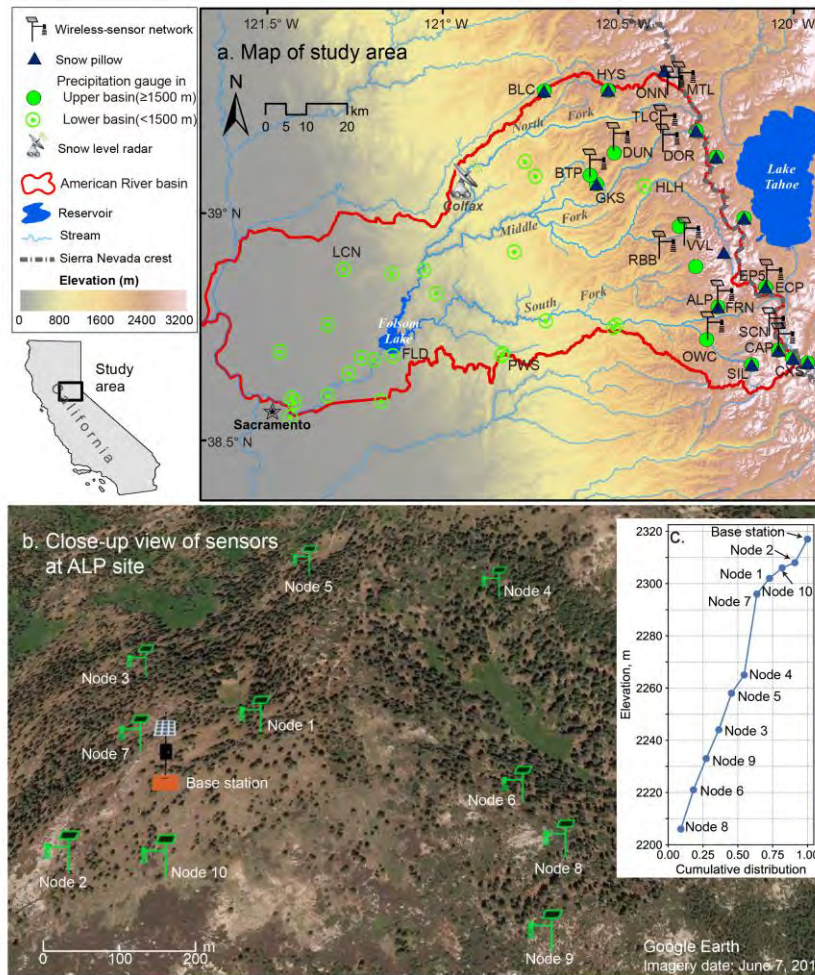
Figure 1. a) Map of the basin-scale distributed wireless-sensor network in the American River basin, operational precipitation gauges, and snow pillows; b) a close-up view of ten sensor nodes and one base station at ALP site shown on Google Earth imagery; and c) plots the elevation distribution of the sensor nodes and base station at ALP.
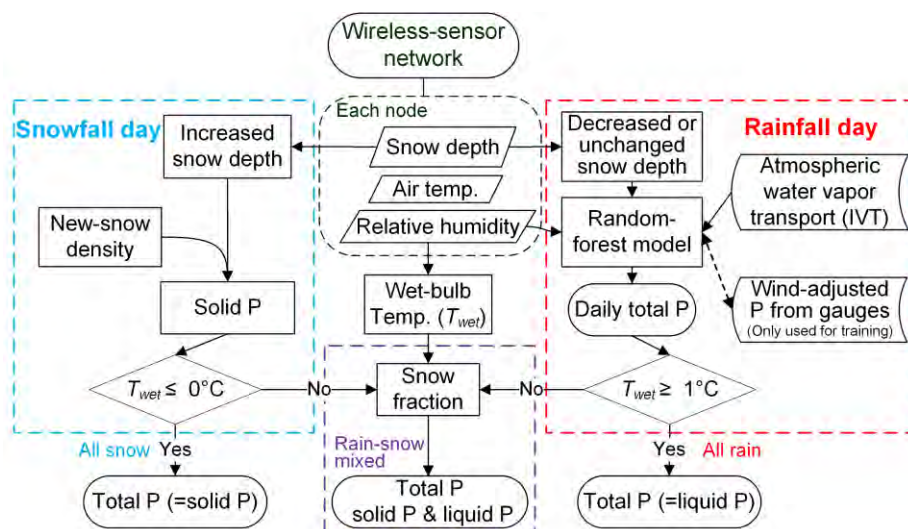
Figure 2. The blending approach for estimating precipitation (P) based on ground-snow-depth changes observed by the wireless-sensor network (blue box during snowfall day) and a random-forest model (red box during rainfall day). The purple box shows the estimation of rain-snow-mixed precipitation using snow fraction.
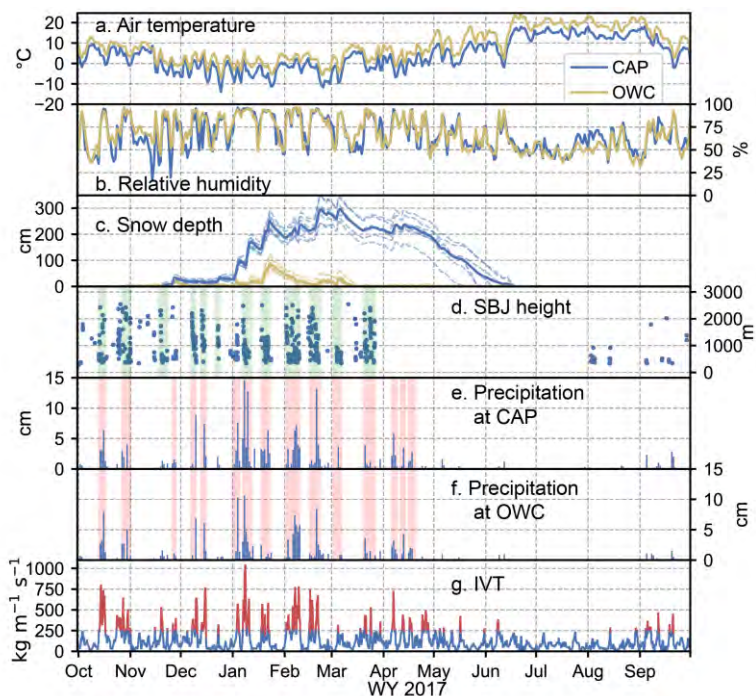
Figure 3. Measurements from two wireless-sensor clusters (CAP, 2440 m and OWC, 1566 m) in WY2017: a) averaged daily air temperature from sensor nodes, b) relative humidity, c) cluster-averaged snow depth (solid line) and snow depth from each sensor node within the cluster (dashed line), d) Sierra barrier jet (SBJ) height using wind profile data at CCO and SBJ-related precipitation events are shaded with green bands, e) daily wind-adjusted precipitation at CAP, and atmospheric-river-related precipitation events are shaded with red bands, f) daily wind-adjusted precipitation at OWC, and g) the Integrated water-Vapor Transport (IVT) at basin outlet, the Folsom Dam, from the MERRA-2 dataset. Values larger than 250 kg m–1 s–1 are marked as red.
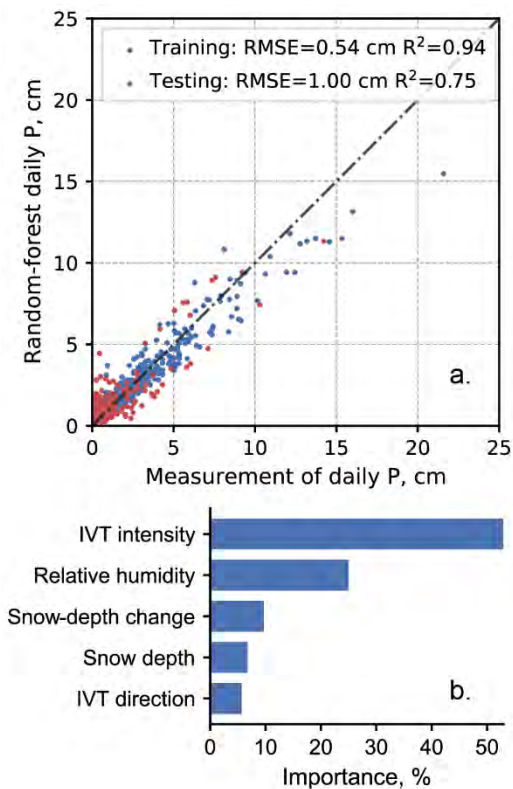
Figure 4. a) Results from the random-forest model to predict daily precipitation from gauges using data split into training (blue) and testing (red). The RMSE (Root Mean Square Error) and R2 (coefficient of determination) quantify model performance, and b) relative feature importance, i.e. normalized-permutation-feature importance from the random-forest model.
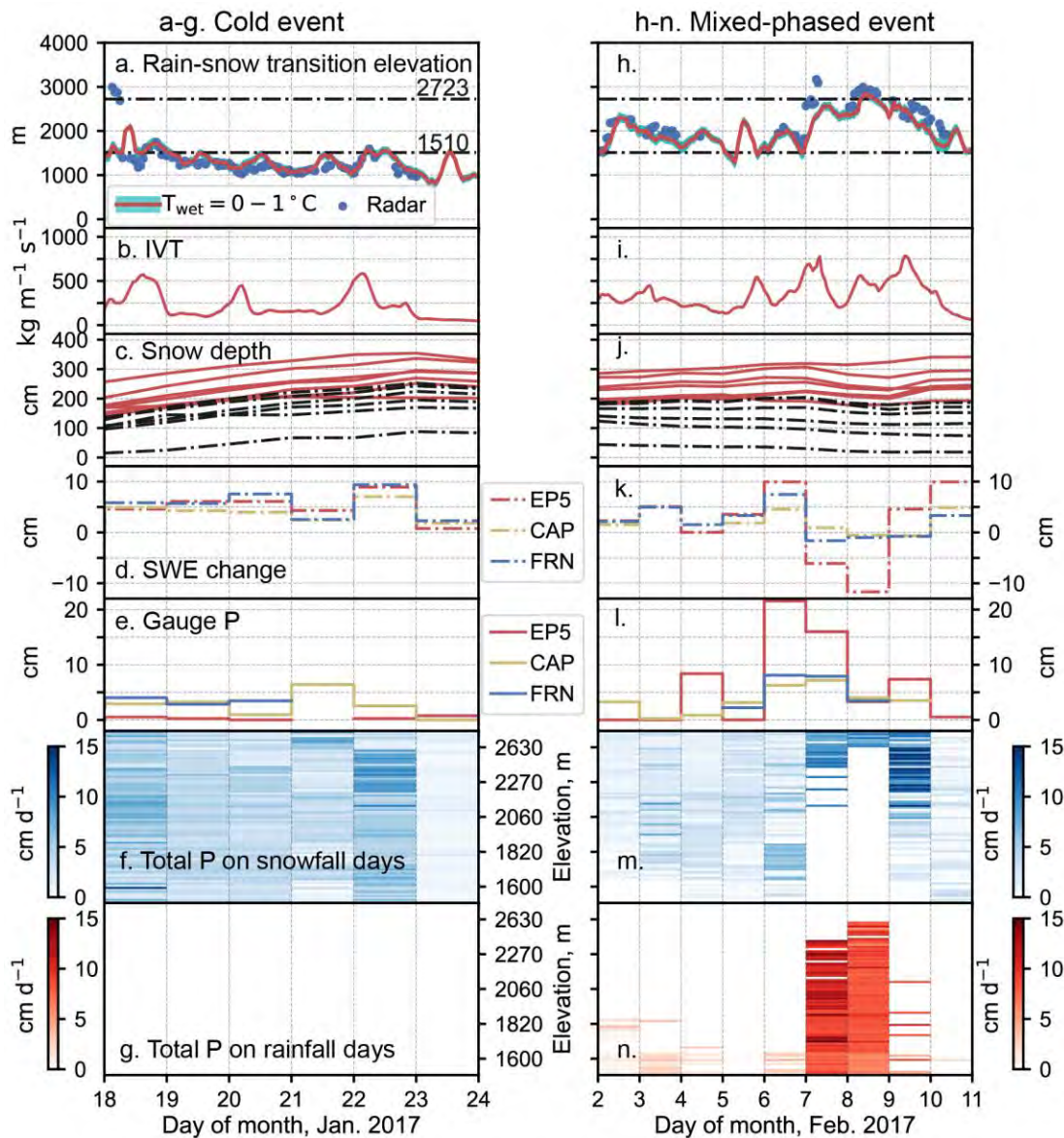
Figure 5. Characteristics of a cold event (left panel, a-g) in January 2017 and a mixed-phased event (right panel, h-n) in February 2017. a) rain-snow-transition zone (shaded area of wet-bulb temperature T_{wet} between 0 and 1 °C, transition elevation (red line of T_{wet} = 0.5 °C), and snow level from the radar at Colfax (blue dot). Black lines denote elevation coverage (1510-2723 m) of the wireless-sensor network, b) hourly integrated water-vapor transport (IVT) at Folsom Dam, c) daily average snow depth from sensor clusters, solid red lines denote higher elevation clusters (> 2000 m) and black dashed lines for lower clusters, d) daily SWE change from three snow pillows at EP5, CAP, and FRN on CDEC, e) daily precipitation (P) from three precipitation gauges, f) daily total precipitation from each sensor node (each row) during snowfall days, and the panel is stacked in order of increasing elevation, and g) daily total precipitation from each sensor node during rainfall days, and the panel is stacked in order of increasing elevation in a nonlinear scale representing elevations of sensor nodes. (h-n) on the right panel are the same as (a-g) but for the mixed-phased event.
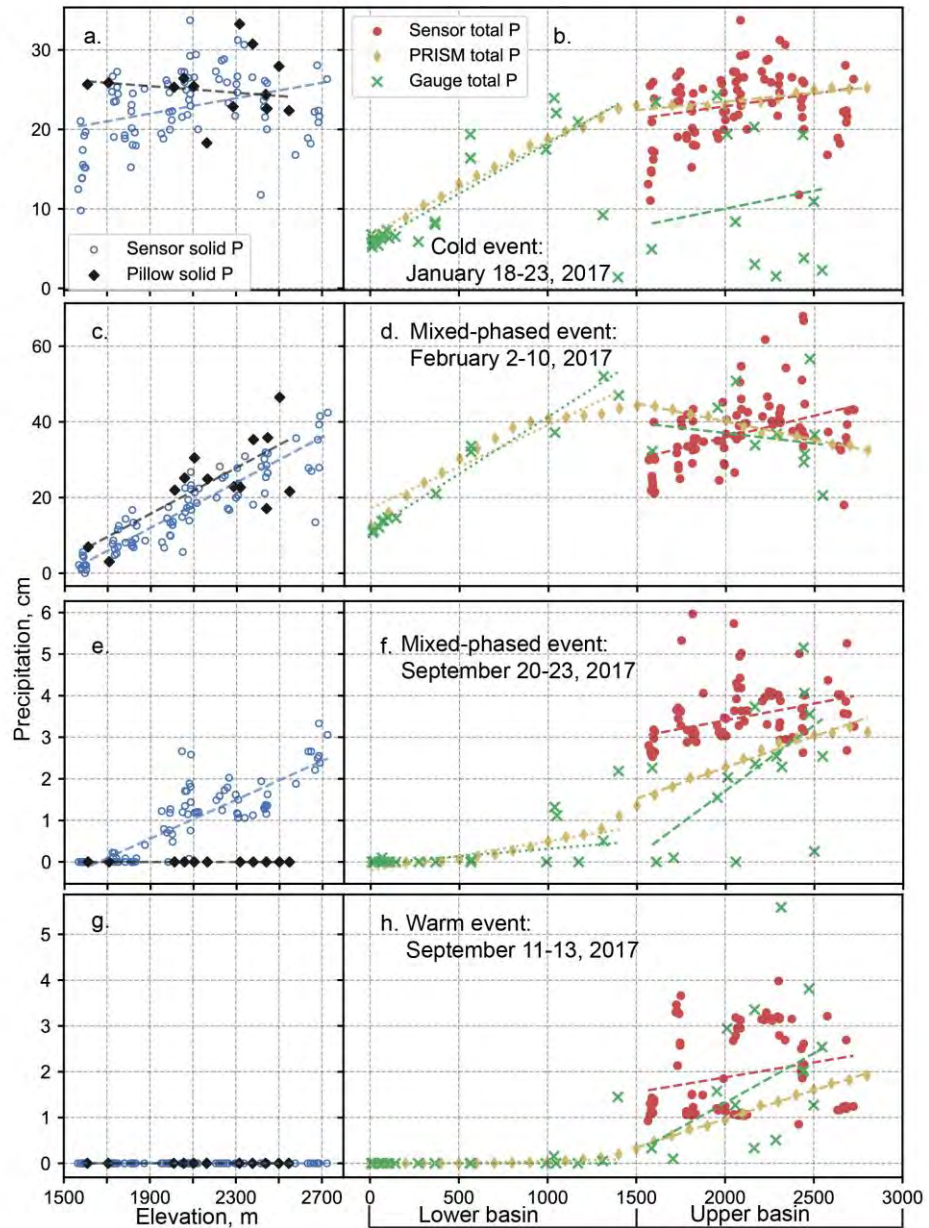
Figure 6. Comparison of solid and total precipitation estimates for four events in WY2017: (a-b) the cold event on 18-23 January, (c-d) the mixed-phased event on February 2-10, (e-f) the mixed-phased event on September 20-23, and (g-h) the warm event on September 11-13. The left panels show solid precipitation from sensor nodes and snow pillows; the right panels show total precipitation from sensor nodes, precipitation gauges, and 100-m banded PRISM data for lower and upper basins. The dashed lines are fitted lines using the Orographic Precipitation Gradients (OPGs) with the corresponding data in the same color. Note that the node-by-node total precipitation in panels (f) and (h) was estimated by the random-forest model. Gauges without precipitation records during events were removed and not plotted in the right panels. The sensor-solid precipitation in panel (e) was partitioned from sensor-total precipitation (f). The summer mixed-phased event (e-f) was confirmed by news (e.g. CBS News, https://www.cbsnews.com/news/snow-last-day-of-summer-sierra-nevada-turns-deadly/).
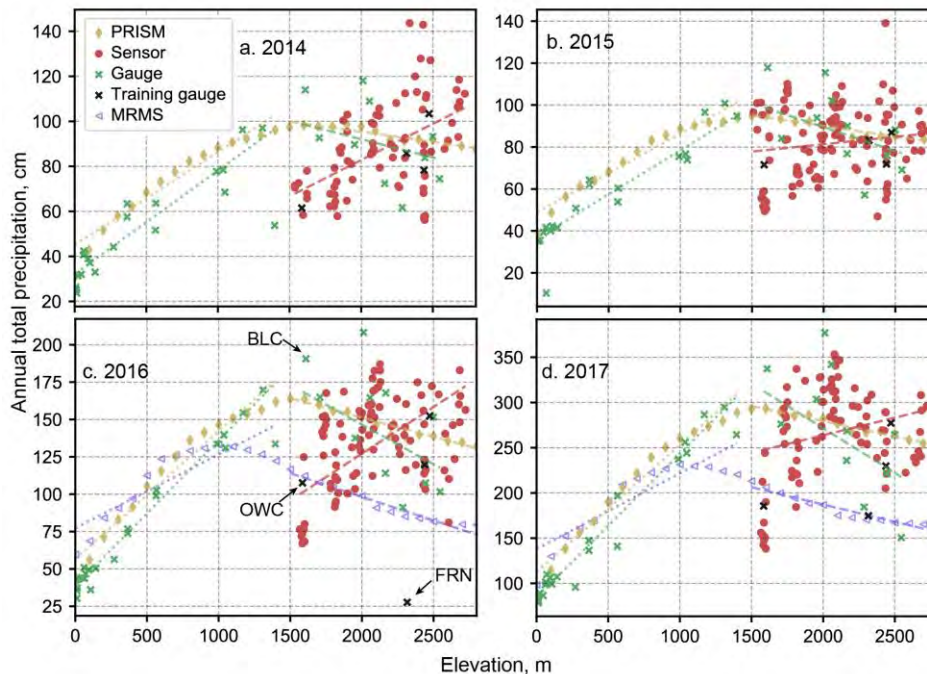
Figure 7. Annual total precipitation estimates from the wireless-sensor network using the blended approach, precipitation gauges, and 100-m banded PRISM and MRMS data: a) WY2014, b) WY2015, c) WY2016, and d) WY2017. Note that the vertical-axis scales of each panel are different. The colored, dashed lines are fitted lines using the Orographic Precipitation Gradients (OPGs) with the corresponding data in the same color, i.e. red, green, yellow, and blue lines are OPG lines for the wireless-sensor network, precipitation gauges, PRISM, and MRMS, respectively. Black cross symbols show the primary four precipitation gauges (i.e. OWC, FRN, EP5, and CAP) used in training the random-forest model. The other two training sites (BTP and DUN) are not plotted as they have limited, reliable precipitation records.
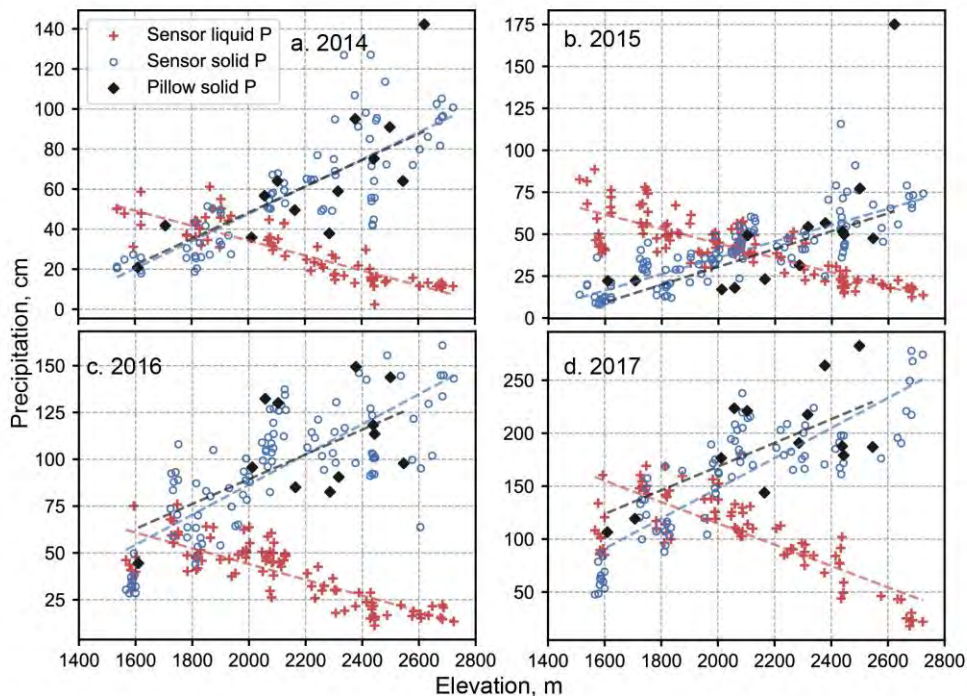
Figure 8. As in Figure 7, but for annual partitioned precipitation (i.e. solid and liquid) estimates from the wireless-sensor network, compared to solid precipitation from snow pillows: a) WY2014, b) WY2015, c) WY2016, and d) WY2017.

24
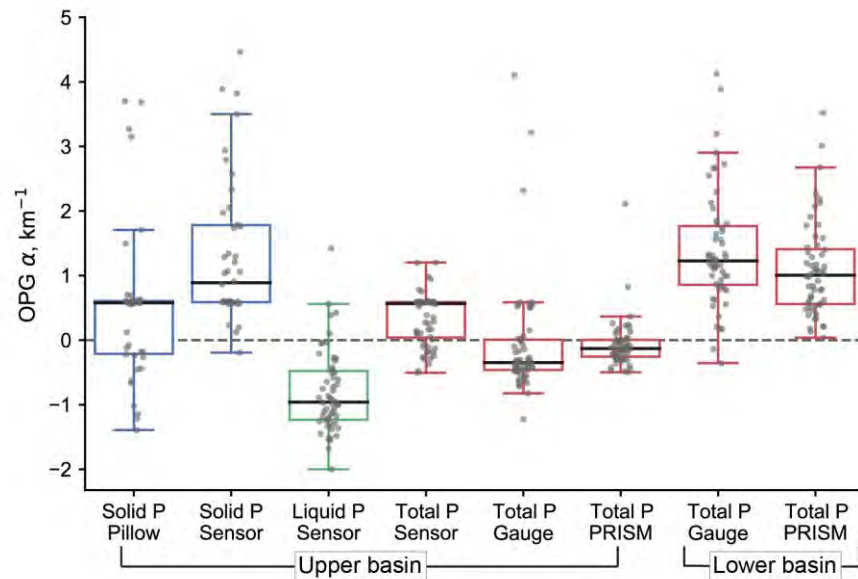
Figure 9. Orographic Precipitation Gradients (OPGs, α) for solid, liquid, and total precipitation for all precipitation events in WY2014-2017, from the wireless-sensor network, snow pillows, precipitation gauges, and PRISM dataset. The black line within the box is the median. The box denotes the interquartile range with lower and upper boundaries of 25th and 75th percentiles, respectively. Whiskers indicate 1.5 times interquartile range beyond the box boundaries. Grey dots show the values of OPG. Questionable OPG values (>5 or <–3 km^{-1}) were removed, as they may occur due to zero or abnormal precipitation data at reference elevation.
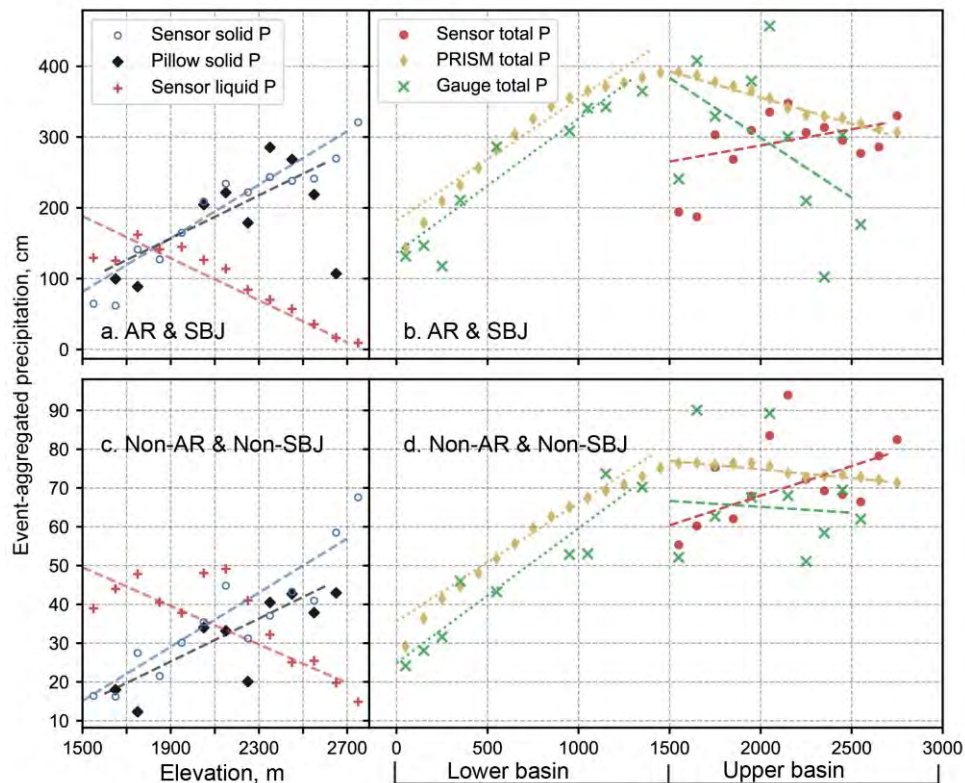
Figure 10. Event-aggregated solid and total precipitation estimates for (a-b) events related to both Atmospheric River (AR) and Sierra Barrier Jet (SBJ) and (c-d) events that are not associated with either AR or SBJ (i.e. Non-AR & Non-SBJ). Left panels show solid precipitation from the wireless-sensor network and snow pillows; right panels show total precipitation from sensor nodes, precipitation gauges, and PRISM for the lower and upper basins. All data are averaged by 100-m elevation bands. The dashed lines are fitted lines using the Orographic Precipitation Gradients (OPGs) with the corresponding data in the same color.

Supporting Information

This supporting information includes the supporting tables and figures referenced in the main text. Results for all 60 precipitation events (Table S1) and all data figures to identify events can be found at https://gitlab.com/UC_WSN/wsn_precip_results/.

Table S1. Precipitation events in WY2014-2017 and their categorizations of Atmospheric River (AR) and Sierra Barrier Jet (SBJ).

ID	Start	End	AR[a]	SBJ height[b], m	Precip. ranking[c]	Type[d]
1	10/27/2013	10/30/2013			50	Mixed
2	11/18/2013	11/21/2013	x	743	40	Mixed
3	12/6/2013	12/8/2013		874	45	Cold
4	1/29/2014	1/31/2014	x		22	Mixed
5	2/5/2014	2/10/2014	x	767	4	Mixed
6	2/26/2014	3/6/2014	x	1105	14	Mixed
7	3/25/2014	4/1/2014	x		16	Mixed
8	4/24/2014	4/25/2014			35	Mixed
9	9/25/2014	9/28/2014			39	Mixed
10	10/31/2014	11/1/2014			52	Mixed
11	11/19/2014	11/22/2014		1317	36	Mixed
12	11/28/2014	12/6/2014			11	Mixed
13	12/10/2014	12/12/2014	x	1138	29	Mixed
14	12/14/2014	12/17/2014		1351	51	Mixed
15	12/19/2014	12/21/2014	x	717	41	Mixed
16	2/6/2015	2/9/2015	x	1080	8	Mixed
17	2/27/2015	3/2/2015			44	Cold
18	4/5/2015	4/8/2015			42	Cold
19	4/21/2015	4/25/2015	x		32	Mixed
20	5/14/2015	5/26/2015			38	Mixed
21	10/1/2015	10/1/2015			58	Warm
22	10/16/2015	10/19/2015			43	Warm
23	10/31/2015	11/3/2015	x		31	Mixed
24	11/8/2015	11/10/2015			48	Cold
25	11/15/2015	11/15/2015			56	Cold
26	11/24/2015	11/26/2015			53	Cold
27	12/2/2015	12/6/2015	x		55	Mixed
28	12/9/2015	12/14/2015	x		19	Cold
29	12/18/2015	12/25/2015	x	790	9	Cold
30	1/4/2016	1/9/2016		1075	34	Cold
31	1/12/2016	1/19/2016	x	852	13	Mixed
32	1/21/2016	1/24/2016	x	900	33	Mixed
33	1/28/2016	1/31/2016	x	605	17	Mixed
34	2/16/2016	2/19/2016			30	Mixed
35	3/3/2016	3/14/2016	x	985	3	Mixed
36	3/20/2016	3/23/2016	x		26	Mixed
37	4/8/2016	4/11/2016			49	Mixed
38	4/21/2016	4/29/2016	x		23	Mixed
39	5/4/2016	5/8/2016			54	Mixed
40	5/20/2016	5/25/2016			46	Mixed
41	10/13/2016	10/17/2016	x	806	7	Mixed
42	10/27/2016	11/1/2016	x	1184	15	Warm
43	11/18/2016	11/23/2016		1001	24	Mixed

44	11/26/2016	11/28/2016	x		37	Cold
45	12/7/2016	12/10/2016	x	1268	12	Mixed
46	12/13/2016	12/16/2016	x	1333	18	Mixed
47	12/22/2016	12/24/2016		1222	47	Cold
48	1/1/2017	1/5/2017	x		10	Cold
49	1/7/2017	1/12/2017	x	971	2	Cold
50	1/18/2017	1/23/2017	x	908	6	Cold
51	2/2/2017	2/10/2017	x	893	1	Mixed
52	2/16/2017	2/22/2017	x	1138	5	Mixed
53	3/2/2017	3/7/2017	x	612	27	Cold
54	3/20/2017	3/27/2017	x	1122	20	Mixed
55	3/29/2017	3/31/2017			59	Mixed
56	4/6/2017	4/9/2017	x		21	Mixed
57	4/11/2017	4/14/2017	x		25	Mixed
58	4/16/2017	4/20/2017	x		28	Mixed
59	9/11/2017	9/13/2017	x		60	Warm
60	9/20/2017	9/23/2017	x	852	57	Mixed

[a] Marker x means that the precipitation event is atmospheric-river-related, and blank denotes a non-atmospheric-river-related event.

[b] Event-averaged SBJ heights are listed for SBJ-related events.

[c] Precipitation ranking is based on cumulative precipitation averaged in the upper basin using PRISM data. Ranking #1 means the largest precipitation event.

[d] Cold event means that more than 50% of the time during the event, rain-snow transition elevation is below 1500 m; warm event means that more than 50% of the time during the event, the transition elevation is above 2700 m; and mixed (mixed-phased) event means that more than 50% of the time during the event, the transition elevation is in between 1500 and 2700 m.

Table S2. Operational stations used for estimating daily new-snow density.

ID	Station name	River basin	Lat, °	Lon, °	Elevation, m	Operator[a]
LOS	Lake Lois	American	38.925	-120.197	2621	CA DWR
CXS	Carson Pass	American	38.692	-120.002	2546	NRCS
LLP	Lower Lassen Peak	Feather	40.467	-121.508	2515	PG&E
CAP	Caples Lake	American	38.710	-120.042	2438	USBR
BLK	Blue Lakes	Mokelumne	38.613	-119.931	2438	NRCS
FRN	Forni Ridge	American	38.805	-120.213	2316	USBR
MDW	Meadow Lake	Yuba	39.406	-120.506	2195	CA DWR
SIL	Silver Lake	American	38.678	-120.118	2164	USBR
HYS	Huysink	American	39.282	-120.527	2012	USBR
RCC	Robinson Cow Camp	Yuba	39.622	-120.680	1975	CA DWR
HRK	Harkness Flat	Feather	40.418	-121.275	1890	CA DWR
GKS	Greek Store	American	39.075	-120.558	1707	USBR
BLC	Blue Canyon	American	39.280	-120.709	1609	USBR

[a] CA DWR: the California Department of Water Resources; NRCS: the Natural Resources Conservation Service; USBR: the US Bureau of Reclamation; PG&E: the Pacific Gas and Electric Company.

Table S3. Wireless-sensor nodes and operational sites used in training the random-forest model.

Sensor cluster (node id)	Operational site	Latitude, °	Longitude, °	Elevation, m	Precipitation samples[b]
Caples Lake (3)	CAP[a]	38.712	-120.042	2440	373
Echo Peak (8)	EP5	38.852	-120.070	2379	325
Alpha (1)	FRN[a]	38.805	-120.215	2318	280
Duncan Peak (7)	DUN[a]	39.150	-120.514	2079	16
Owens Camp (7)	OWC[a]	38.736	-120.243	1566	302
Bear Trap (6)	BTP[a]	39.094	-120.581	1510	28

[a] Gauge precipitation at this site was wind-adjusted. Note that we only selected consistent precipitation data in BTP and DUN for training the model by comparing to PRISM data.
[b] Total number of daily precipitation samples used in the random-forest model.

Table S4. Orographic Precipitation Gradients (OPGs, α in the unit of km^{-1}) of annual precipitation in WY2014-2017.

WY	Upper Basin						Lower Basin	
	Sensor liquid	Sensor solid	Pillow solid	Sensor total	Gauge total	PRISM total	Gauge total	PRISM total
2014	-0.82	2.51	2.29	0.44	-0.17	-0.09	1.12	0.77
2015	-0.75	2.28	3.64	0.09	-0.24	-0.11	0.93	0.67
2016	-0.74	1.29	0.95	0.58	-0.33	-0.16	1.68	1.16
2017	-0.69	1.35	0.83	0.15	-0.33	-0.12	1.37	1.00
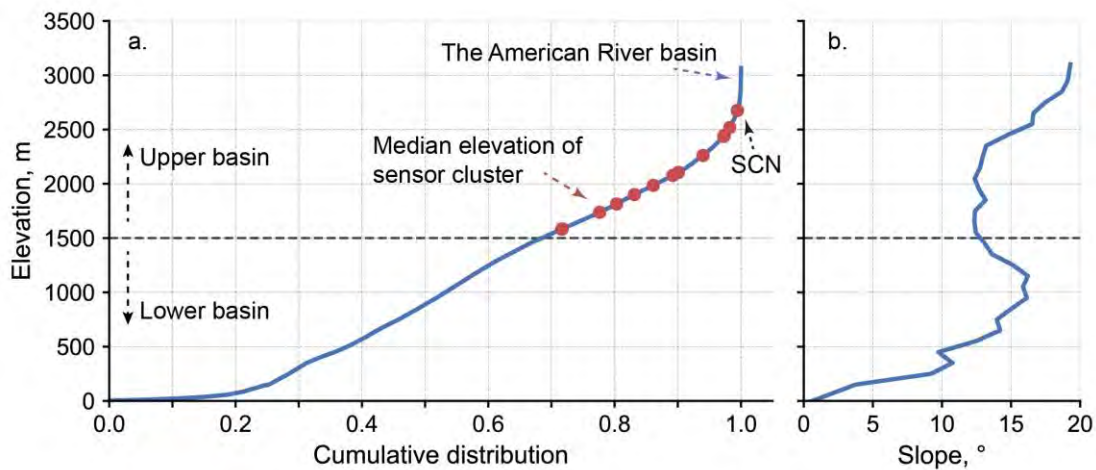
Figure S1. a) Cumulative distribution of basin elevation (blue line) and median elevation of each sensor cluster (red circle). Note that some circles are overlapped. b) Distribution of terrain slope using the average value of each 100-m elevation band. The horizontal dashed line at 1500-m elevation separates the upper and lower basins.
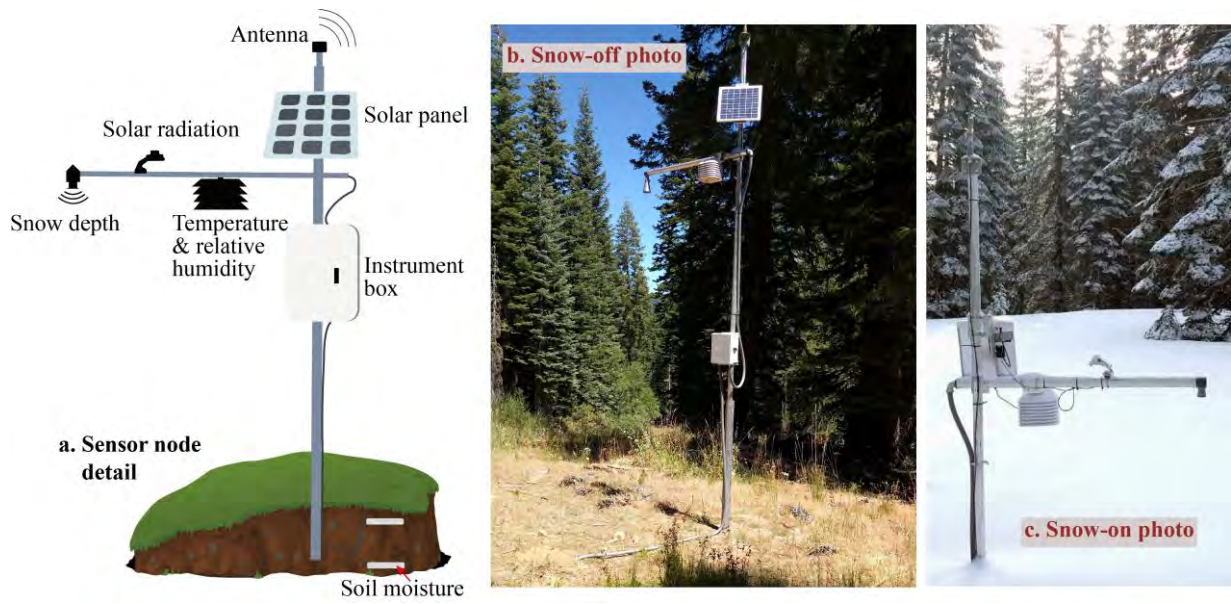
Figure S2. a) Schematic detail of sensor node; b) photo of a sensor node on a snow-off day; and c) photo of a sensor node on a snow-on day.
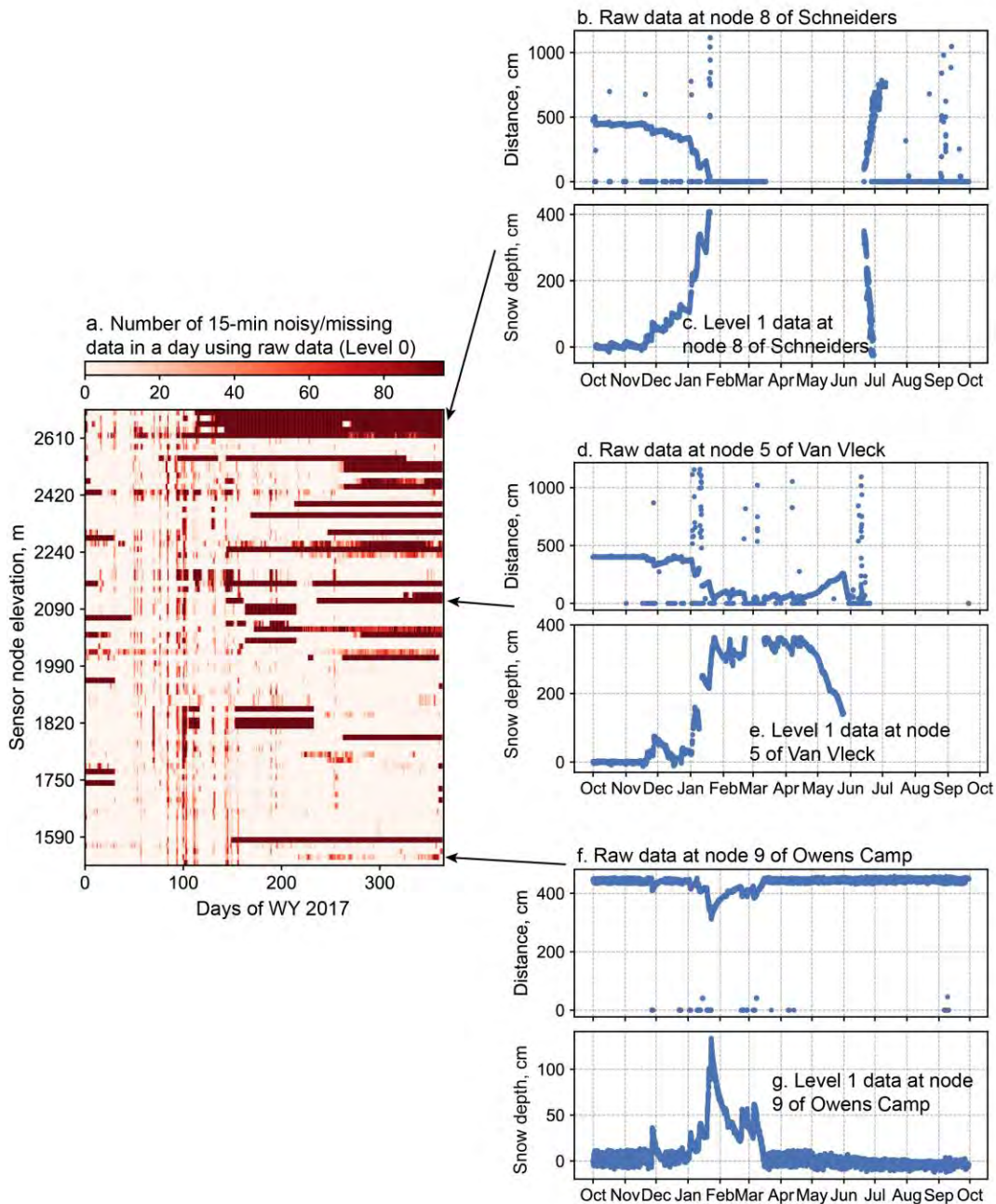
Figure S3. a) Numbers (ranging 0-96) of noisy/missing data in a day using 15-min raw data (Level 0), the panel is stacked in order of increasing elevation in a nonlinear scale (ticks labeled every 10 nodes), representing elevations of each sensor node. (b-c) plot the distance to ground (raw data) and snow depth (Level 1) at 15-min resolution for node 8 of Schneiders, respectively, with an arrow referring to its location in panel (a). Similarly, panels (d-e) and (f-g) show data for node 5 of Van Vleck and node 9 of Owens Camp, respectively.
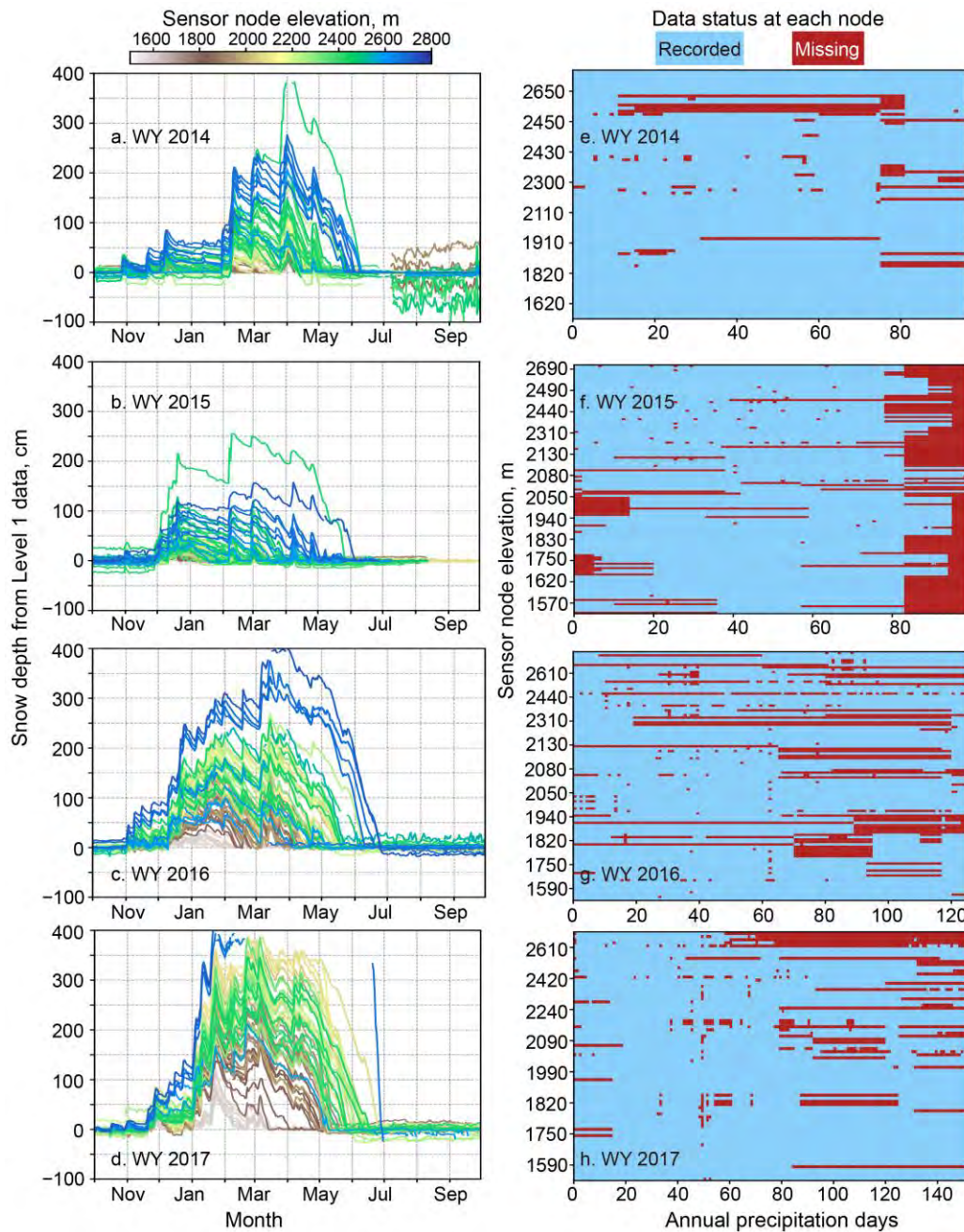
Figure S4. Snow depth and recoding status using Level 1 data in WY 2014-2017. Left panels (a-d) plot daily snow depth (Level 1) at sensor nodes (colored by its elevation) with at least 30% annual records. Right panels (e-h) plot the Level-1 data-recording status at each sensor node during all identified precipitation days (defined as days with average PRISM precipitation in the upper basin larger than 0.254 mm). Panels (e-h) are stacked in the order of increasing elevation in a nonlinear scale (ticks labeled every 10 nodes), representing elevations of active sensor nodes, for which there were small changes in the number and thus elevational range for each year. Red denotes missing data and blue for recorded data.
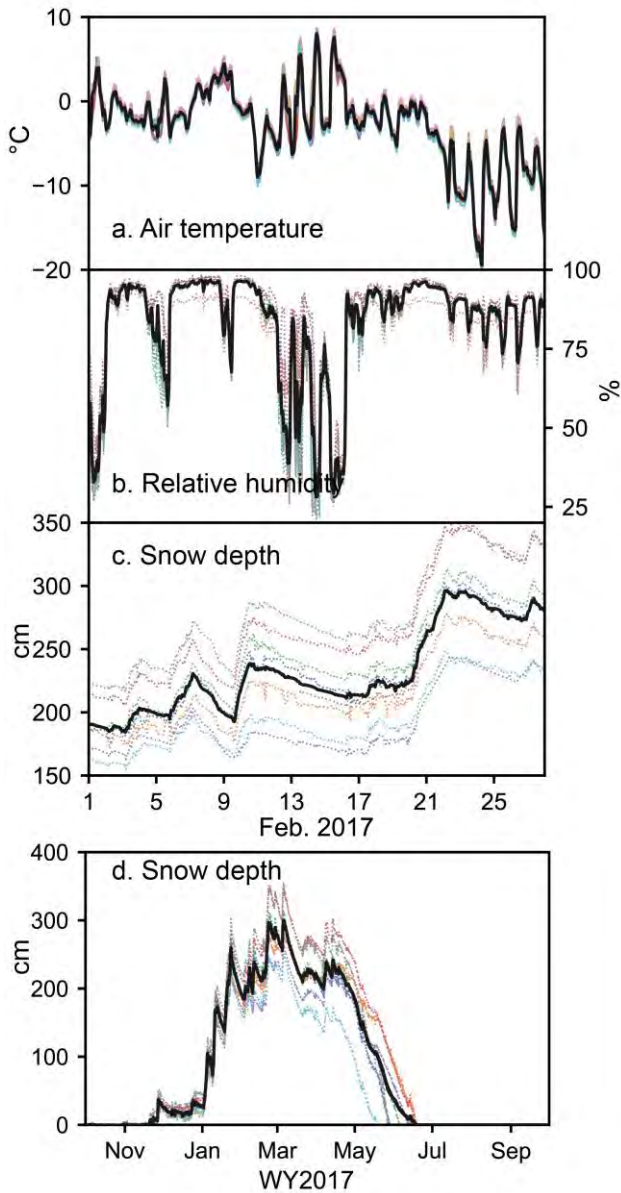
Figure S5. Hourly measurements of a) air temperature, b) relative humidity, c) snow depth from 10 sensor nodes (dashed lines with random color for each node) and cluster mean (solid black line) at CAP cluster in February 2017, and d) same as c) but for entire WY2017.
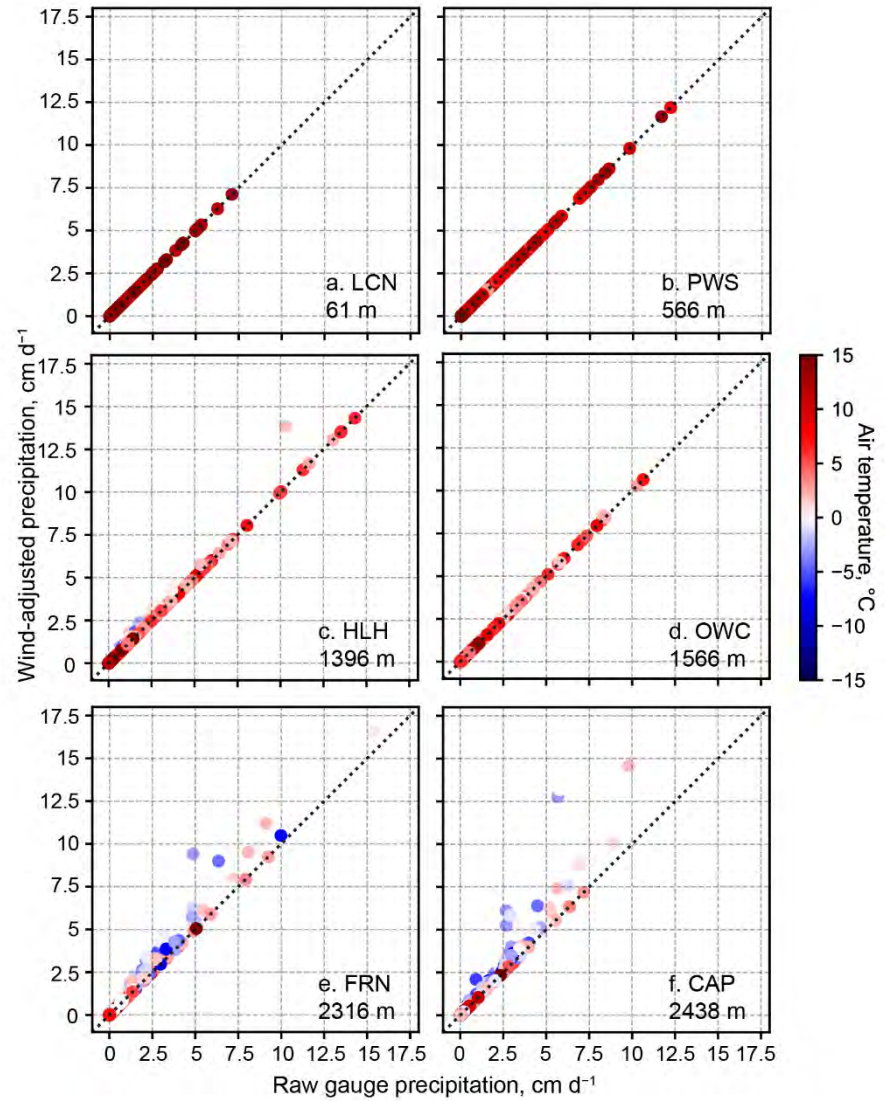
Figure S6. Wind-adjusted daily precipitation at six operational gauge sites in the American River basin in WY2014-2017: a) LCN, b) PWS, c) HLH, d) OWC, e) FRN, and f) CAP. The black dashed line is a reference 1:1 line, and point color shows mean daily temperature. See Table 2 for station information.
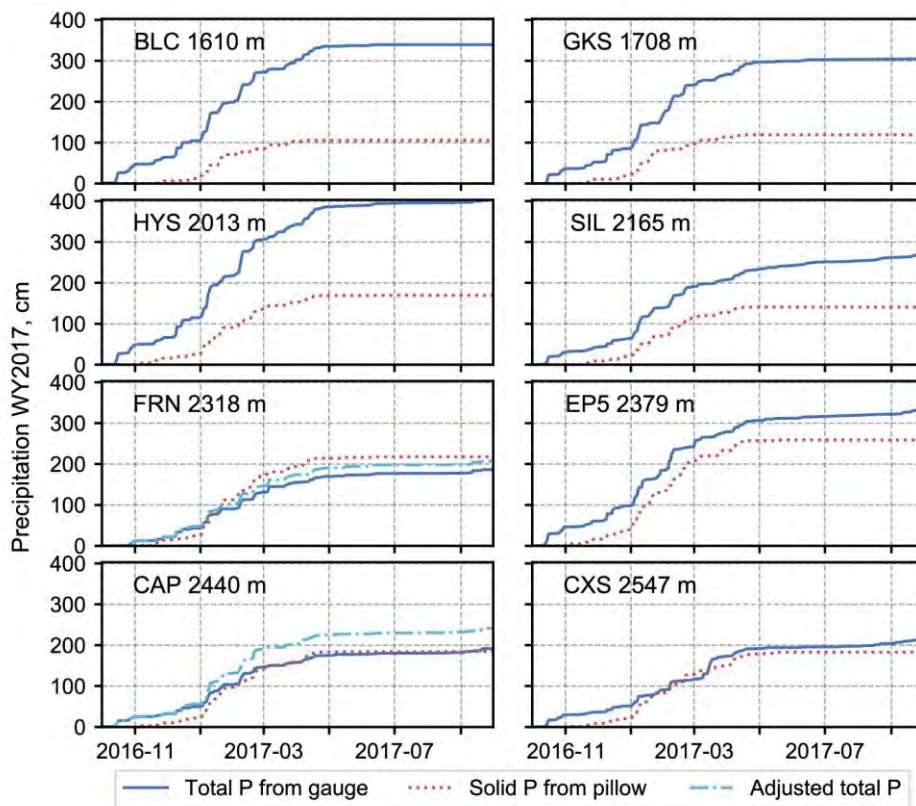
Figure S7. Cumulative total precipitation from gauges, solid precipitation from snow pillows, and wind-adjusted precipitation (at FRN and CAP) at eight operational sites for WY2017.
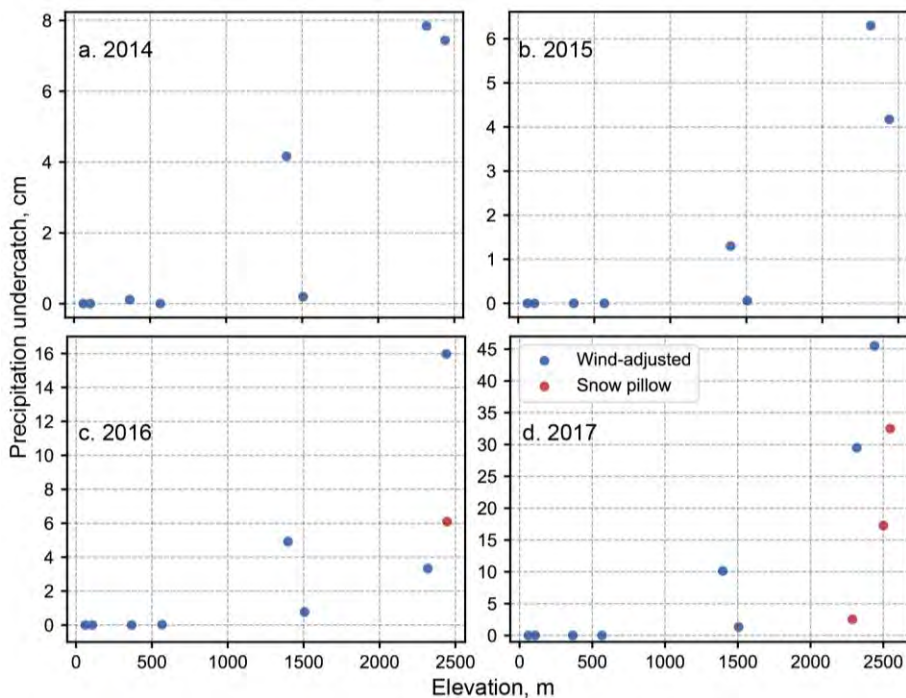
Figure S8. Annual precipitation undercatch from gauges along elevation: a) WY2014, b) WY2015, c) WY2016, and d) WY2017. Gauge-undercatch amount was estimated as the gauge-precipitation amount less than wind-adjusted precipitation (blue) or the solid precipitation from snow pillow (red). Gauge-undercatch amounts by comparing to snow pillow (red points in WY2016-2017) were plotted only when cumulative snow-pillow solid precipitation was larger than gauge total precipitation.
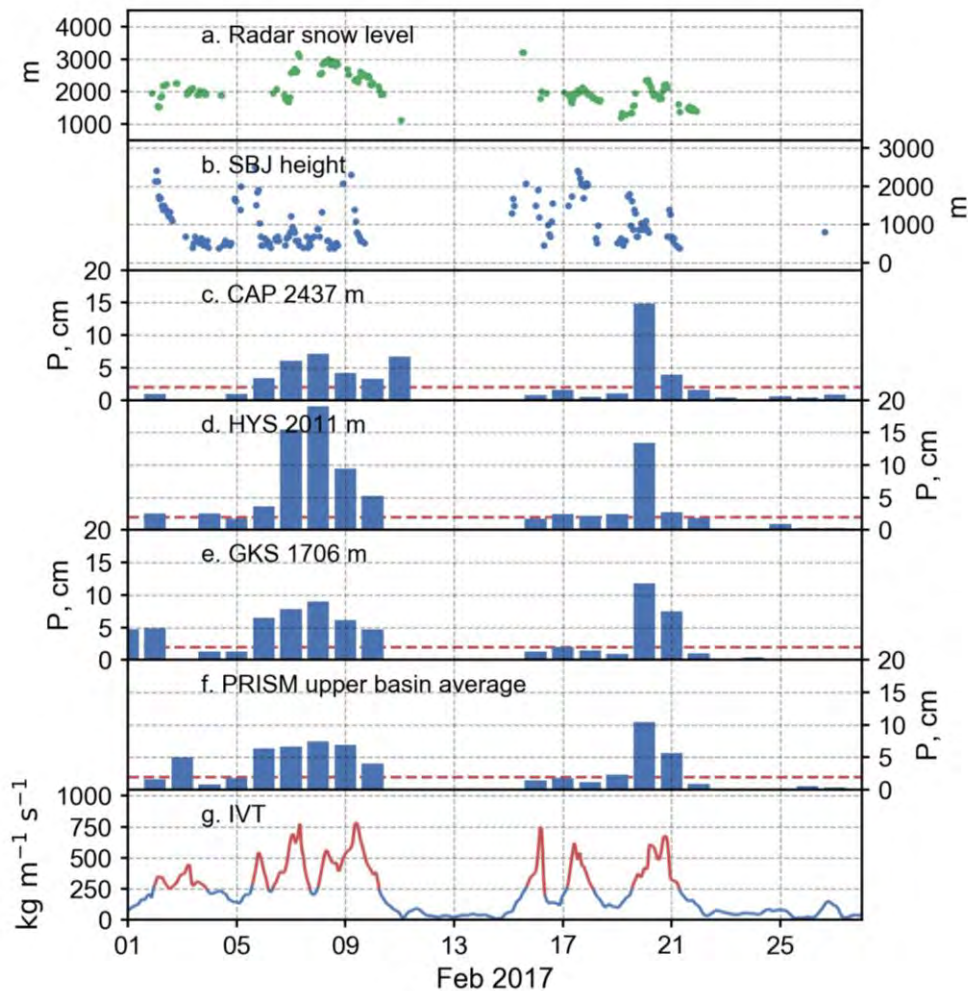
Figure S9. Example for data used to identify precipitation events in February 2017. a) Snow level from the radar at Colfax, b) Sierra barrier jet (SBJ) height using wind profile data at CCO, (c-d) daily wind-adjusted precipitation at CAP, HYS, and GKS, respectively, f) daily, averaged precipitation from PRISM dataset for the upper basin (≥ 1500-m elevation); red horizontal dashed line indicates 2-cm daily precipitation, and g) the Integrated water-Vapor Transport (IVT) at Folsom Dam, from the MERRA-2 dataset. IVT values larger than 250 kg m^{-1} s^{-1} are marked as red.
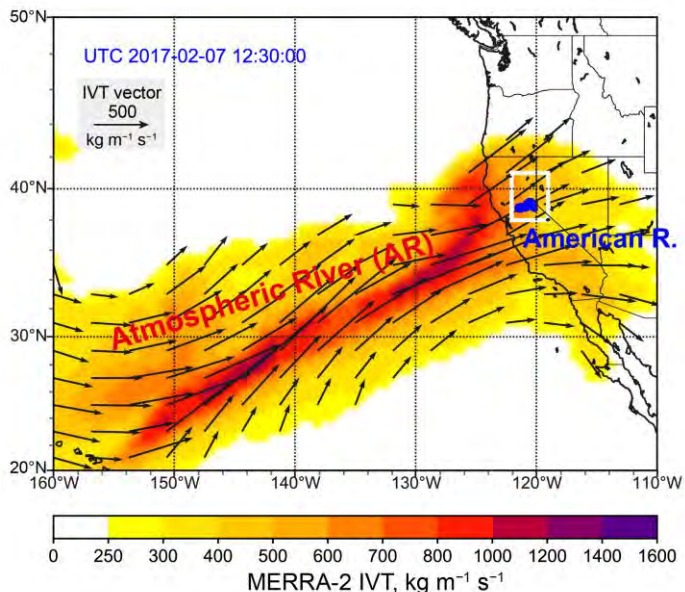
Figure S10. The Integrated water-Vapor Transport (IVT) pattern in an atmospheric-river-related precipitation event in February 2017. IVT data are based on the Modern-Era Retrospective analysis for Research and Applications, version 2 (MERRA-2) dataset. IVT vectors exceeding 250 kg m^{-1} s^{-1} are shown. The blue region denotes the American River basin, and the white-edge region denotes the northern Sierra Nevada.
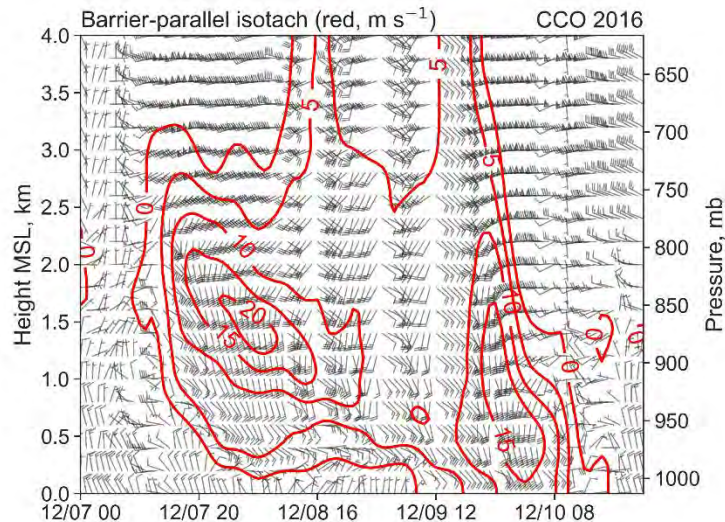
Figure S11. Time-height section of CCO wind data for an SBJ-related event in December 2016. Hourly wind barb shows wind direction and speed (flag = 25 m s^{-1}; bard = 5 m s^{-1}). Red isotach shows the Sierra barrier-parallel (directed from 160° to 340°) wind speed.
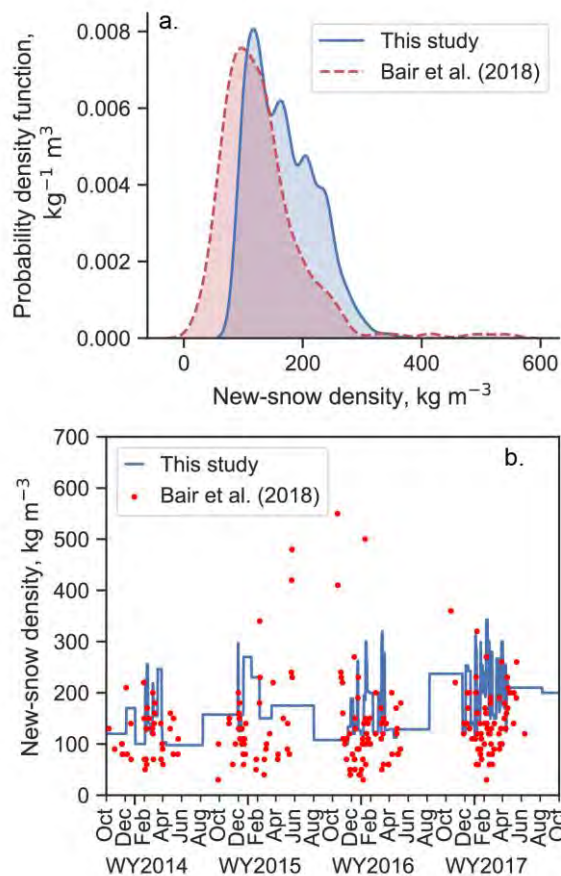
Figure S12. New-snow density used in this study (blue lines) for estimating solid precipitation during snowfall days in WY 2014-2017: a) probability density function of the new-snow density derived by SWE and snow depth from 13 co-located operational sites in this study. The red line shows the probability density of the daily manually measured new-snow density collected by Mammoth Mountain Ski Patrol at the Sesame snow study plot (not within the American River Basin, 37.650° N, 119.042° W, 2743 m elevation) for WY 2010-2017 from Bair et al. (2018); and b) the time series of new-snow density used in this study and the measured data from Bair et al. (2018). Note that one exceptionally large density of 900 kg m^{-3} during a rain-on-snow event (Oct. 19, 2015) was removed from Bair et al. (2018).
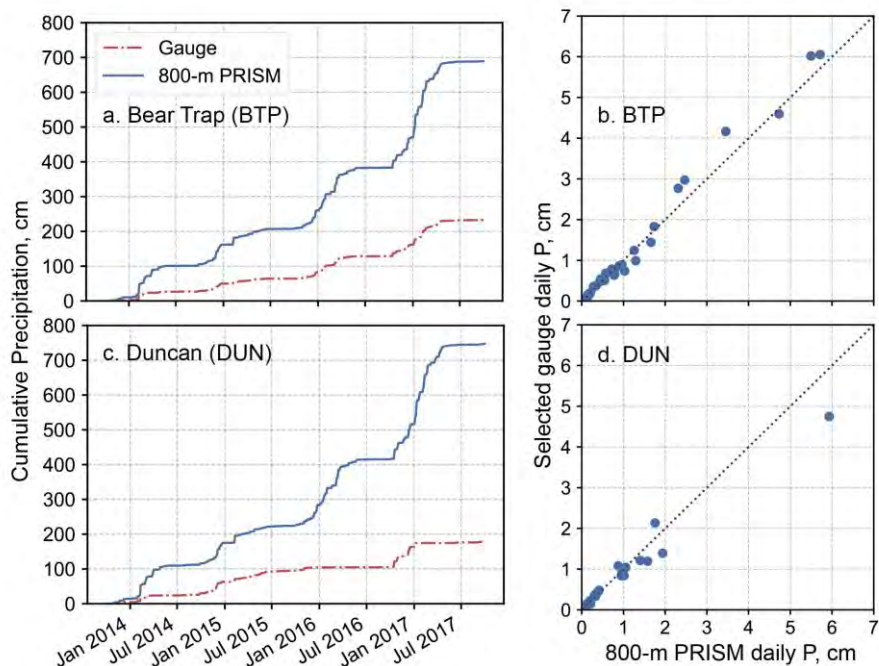
Figure S13. Cumulative precipitation obtained from precipitation gauges and 800-m PRISM data at a) Bear Trap and c) Duncan for WY 2014-2017. b) and d) show the selected daily gauge precipitation data based on their absolute and relative differences to 800-m PRISM data. These selected gauge precipitation data are included in the training dataset in the random-forest model.
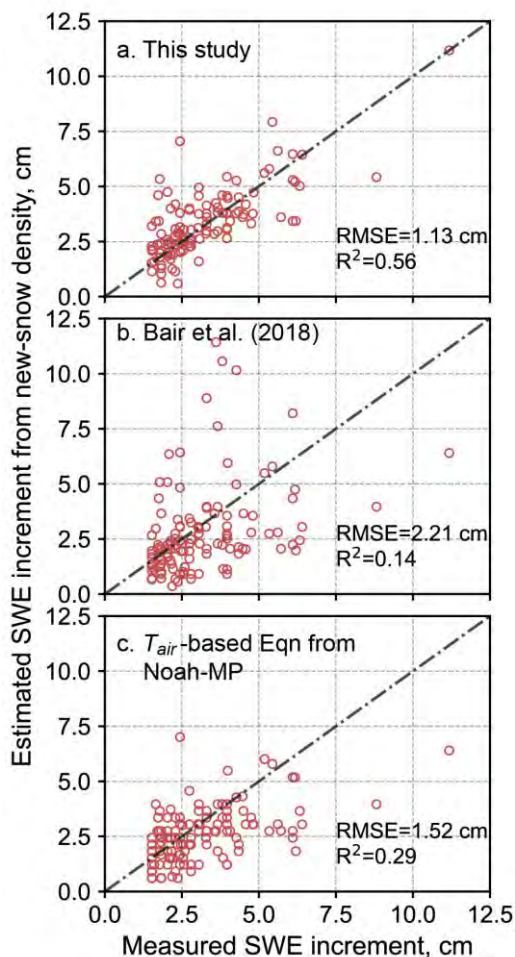
Figure S14. Comparison between measured daily SWE increments (solid precipitation on cold, snowy days) from snow pillows and the estimated SWE increments from snow-depth increment multiplied by new-snow densities from three different methods: a) averaged density from 13 operational sites used in this study, b) measured density at the Sesame snow study plot from Bair et al. (2018), and c) new-snow density (ρ_{new}, kg m^{-3}) equation based on air temperature (T_{air}, °C) from the Noah-MP land surface model (Niu et al., 2011), which is $\rho_{new} = \max[120, 67.92+51.25\times\mathrm{EXP}(T_{air}/2.59)]$. RMSE is the root mean square error, and R^2 is the coefficient of determination. Dashed lines show the 1:1 reference lines.
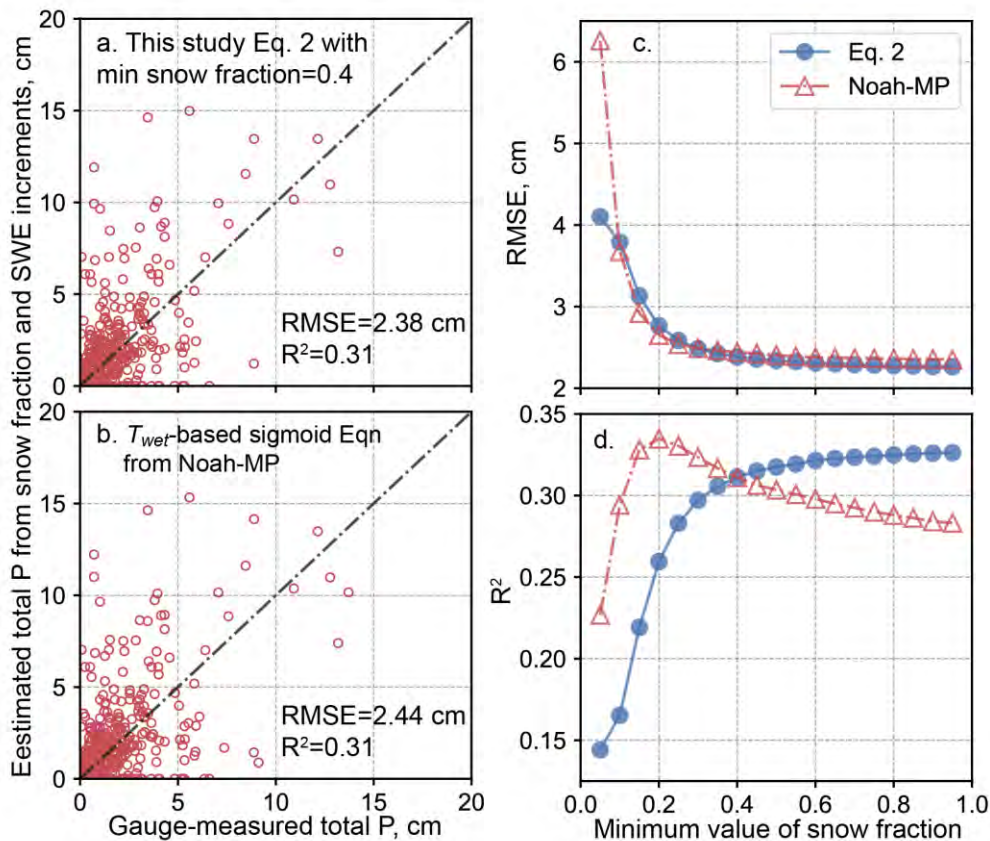
Figure S15. Comparison between gauge-measured daily total precipitation and estimated total precipitation from daily SWE increments from co-located snow pillows (FRN, EP5, and CAP) divided by snow fraction. a) snow fraction from Equation 2 in this study and b) snow fraction based on a sigmoid function using wet-bulb temperature (T_{wet}, °C) from the Noah-MP model (Wang et al., 2019), which is $snow\ fraction = \frac{1}{1+0.0000699EXP(2(T_{wet}+3.97))}$. For a) and b), a minimum value of snow fraction is set to 0.4 when rain-snow mixed phase is predicted (i.e. snow fraction > 0), to avoid potential, unreasonable large total precipitation. RMSE is the root mean square error, and R^2 is the coefficient of determination. Dashed lines show the 1:1 reference lines. Panels c) and d) plot RMSE and R^2 values as a function of the minimum value of snow fraction, respectively.
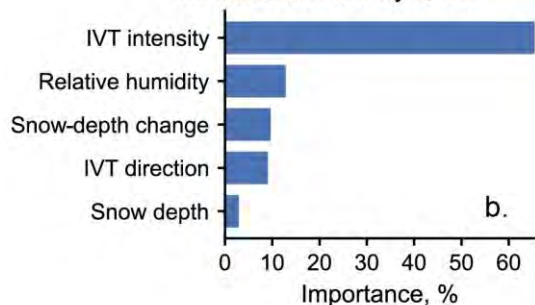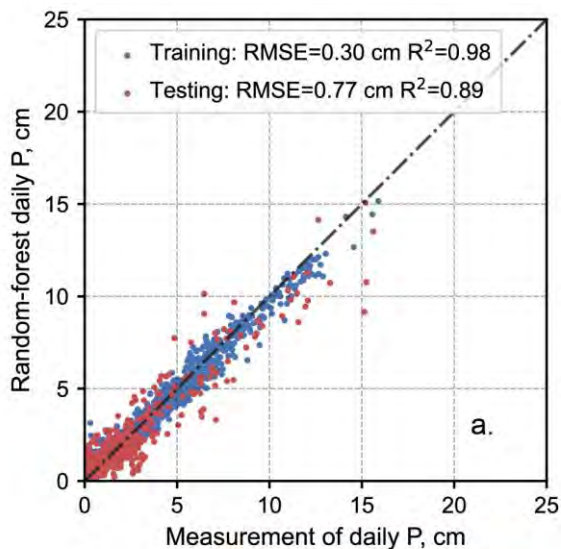
Figure S16. Results from the random-forest model using PRISM precipitation at all 13 clusters as training data. a) Predicted daily precipitation from gauges using data split into training (85%, blue) and testing data (15%, red). The RMSE (Root Mean Square Error) and R^2 (coefficient of determination) quantify the predictive performance of the model, and b) relative feature importance, i.e. normalized permutation importance from the random-forest model.
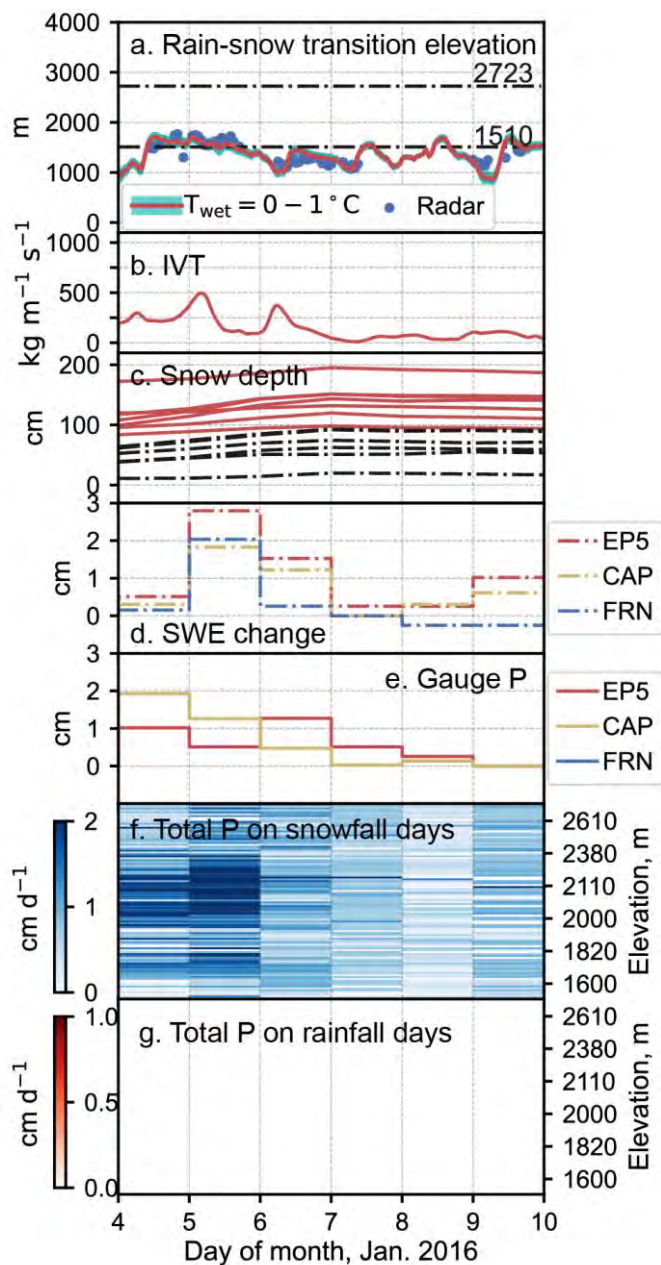
Figure S17. A cold event in January 2016 used to compare total precipitation estimates to that from SWE reanalysis data. a) rain-snow-transition zone (shaded area of wet-bulb temperature T_{wet} between 0 and 1 °C, transition elevation (red line of T_{wet} = 0.5 °C), and snow level from the radar at Colfax (blue dot). Black lines denote elevation coverage (1510-2723 m) of the wireless-sensor network, b) hourly integrated water-vapor transport (IVT) at Folsom Dam, c) daily average snow depth from the sensor clusters, solid red lines denote higher elevation clusters (> 2000 m) and black dashed lines for lower clusters, d) daily SWE change from three snow pillows at EP5, CAP, and FRN on CDEC, e) daily precipitation (P) from three precipitation gauges, f) daily total precipitation from each sensor node (each row) during snowfall days, and the panel is stacked in order of increasing elevation, and g) daily total precipitation from each sensor node during rainfall days, and the panel is stacked in order of increasing elevation in a nonlinear scale representing elevations of sensor nodes.
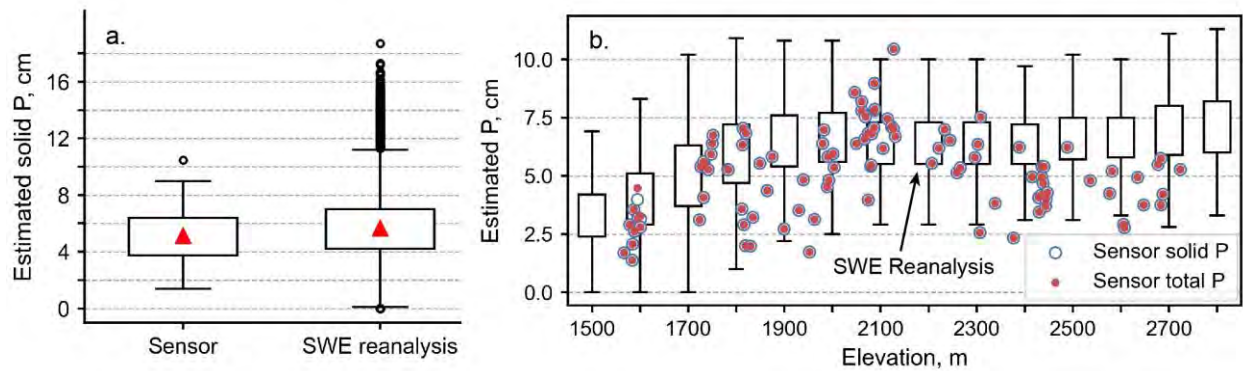
Figure S18. Precipitation estimates from the sensor network and SWE reanalysis data during a cold storm on January 4-9, 2016 (Figure S17). a) Solid precipitation comparison using boxplots. The red triangle within the box is the mean, the box denotes the interquartile range with lower and upper boundaries of 25th and 75th percentiles, respectively, and whiskers indicate 1.5 times interquartile range beyond the box boundaries. Data beyond the whiskers are plotted as individual points. b) Partitioned solid and total precipitation along elevation from the sensor network, compared to boxplots of 100-m banded solid precipitation from SWE reanalysis.
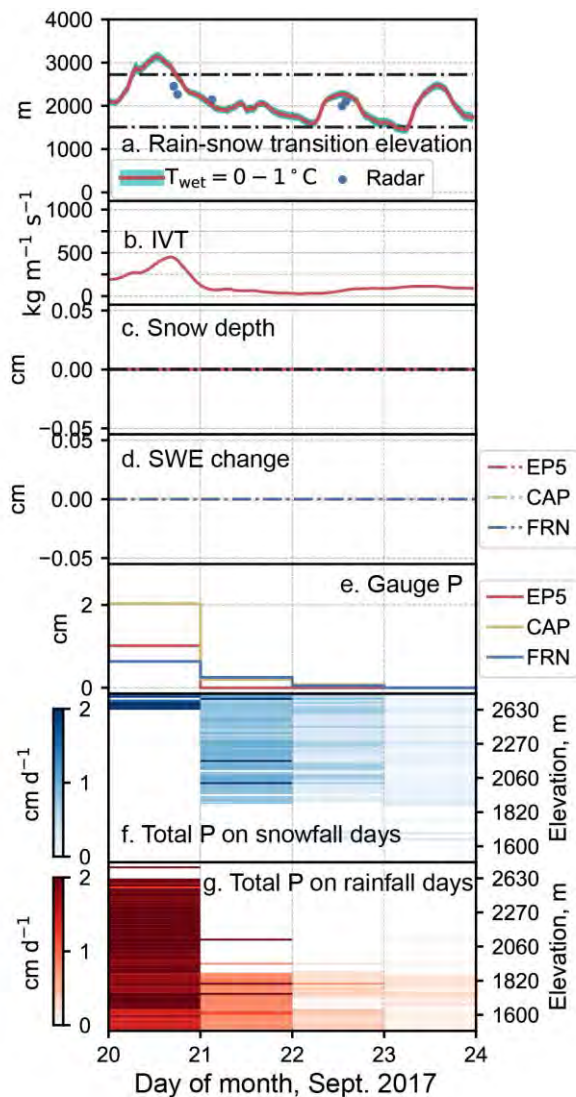
Figure S19. Same as Figure S17, but for a summer mixed-phased event on September 20-23, 2017.
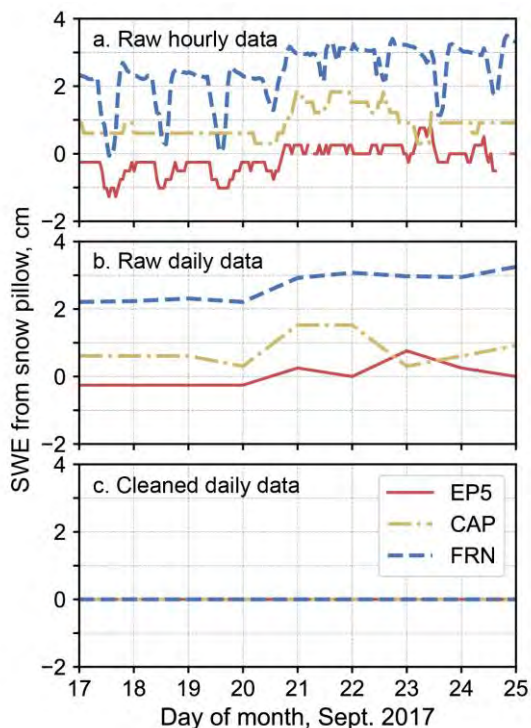
Figure S20. SWE measurements from snow pillows (EP5, CAP, and FRN from CDEC) at different data-processing levels around the summer mixed-phased event on September 20-23, 2017: a) raw hourly data, b) raw daily data, computed from hourly data, and c) cleaned daily data, i.e. the SWE data labeled as "revised" on CDEC. See https://cdec.water.ca.gov/dynamicapp/staMeta?station_id=CAP for an example of snow-pillow data at CAP: raw hourly/daily data from sensor number 3, and cleaned daily data from sensor number 82.
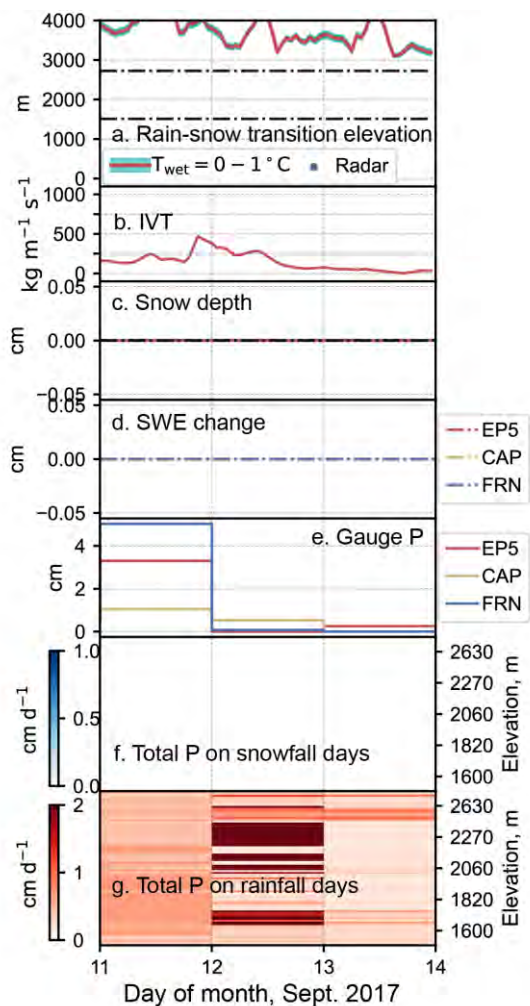
Figure S21. Same as Figure S17, but for a warm event on September 11-13, 2017.
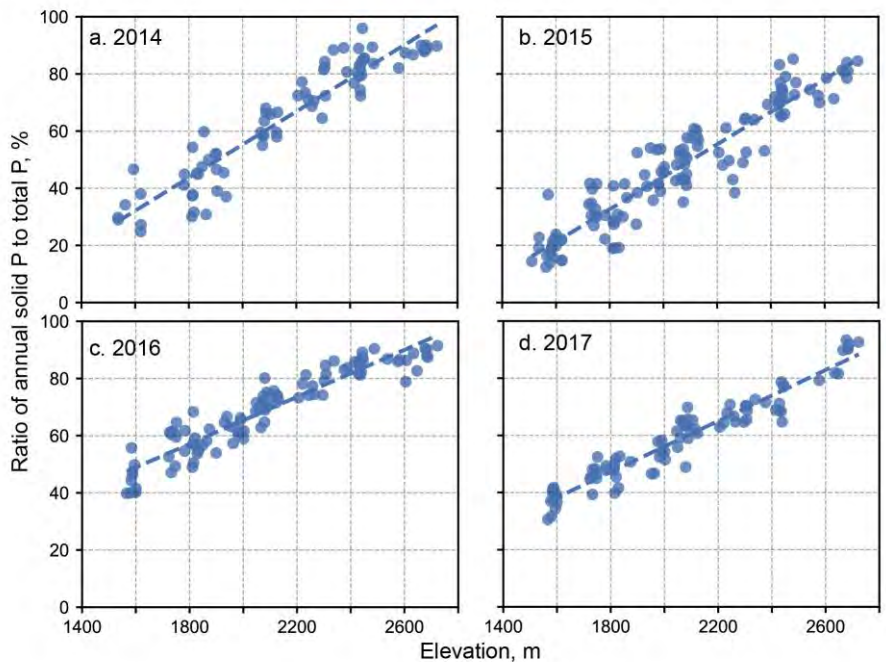
Figure S22. Ratio of annual solid precipitation over total precipitation from the wireless-sensor network: a) WY2014, b) WY2015, c) WY2016, and d) WY2017. The best linear fits of the data are plotted as dashed lines.
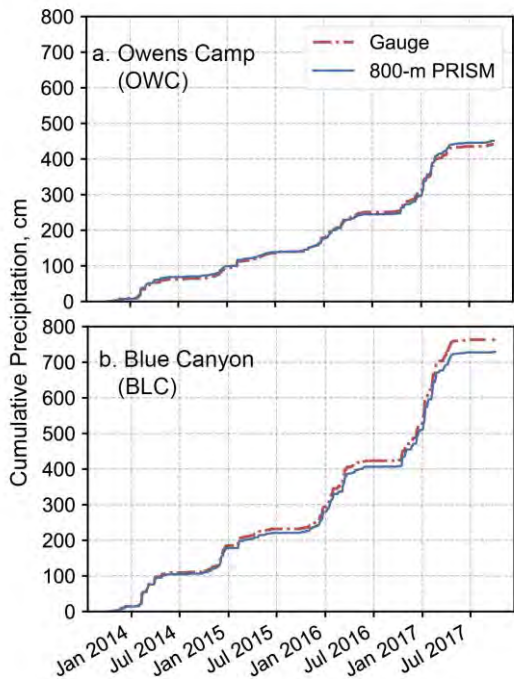
Figure S23. Cumulative precipitation for WY2014-2017 from precipitation gauges and 800-m PRISM data at a) Owens Camp in the South Fork American River and b) Blue Canyon in the North Fork American River.
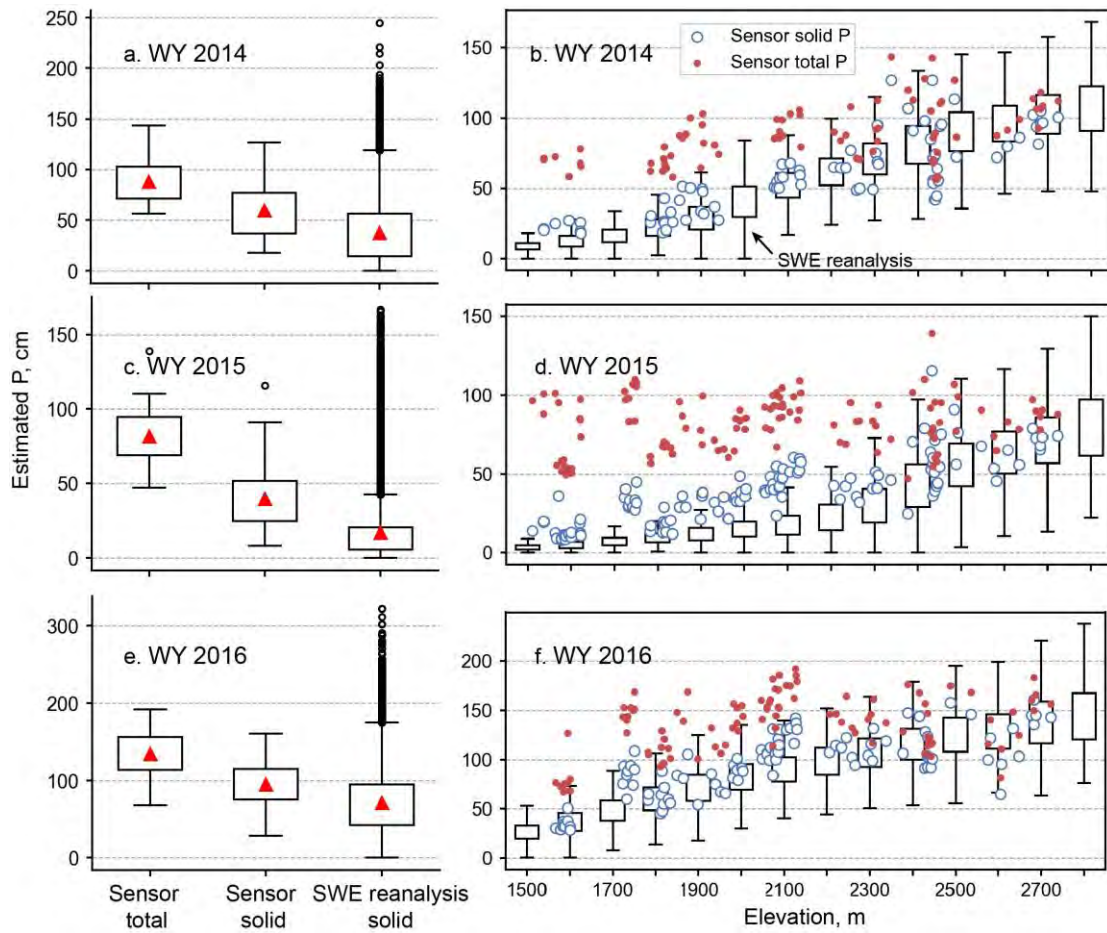
Figure S24. Comparison of precipitation estimates from the sensor network and SWE reanalysis data for WY2014-2016. Left panels (a, c, and e) show the precipitation comparison using boxplots. The red triangle within the box is the mean. The box denotes the interquartile range with lower and upper boundaries of 25th and 75th percentiles, respectively. Whiskers indicate 1.5 times interquartile range beyond the box boundaries. Data beyond the whiskers are plotted as individual points. Right panels (b, d, and f) show partitioned solid and total precipitation along elevation from the wireless sensors, compared to boxplots of 100-m banded solid precipitation from the SWE reanalysis.
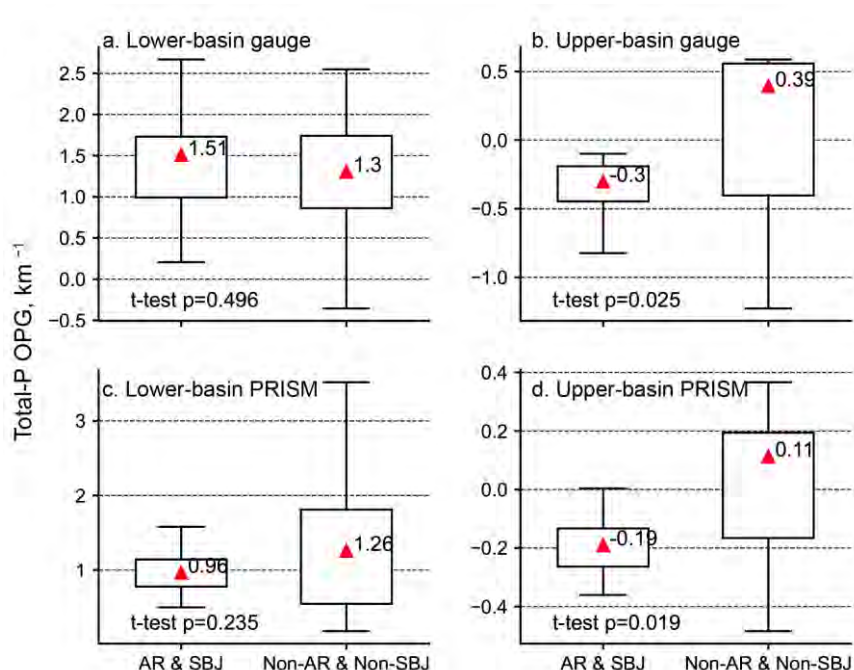
Figure S25. Comparison of the Orographic Precipitation Gradients (OPGs) between AR&SBJ events and Non-AR & Non-SBJ events: a) lower-basin and b) upper-basin total-precipitation OPGs from gauges, respectively. c) lower-basin and d) upper-basin total-precipitation OPGs from PRISM, respectively. The mean value is labeled and plotted as a red triangle. The p-values from two-tailed student's t-tests are also labeled.
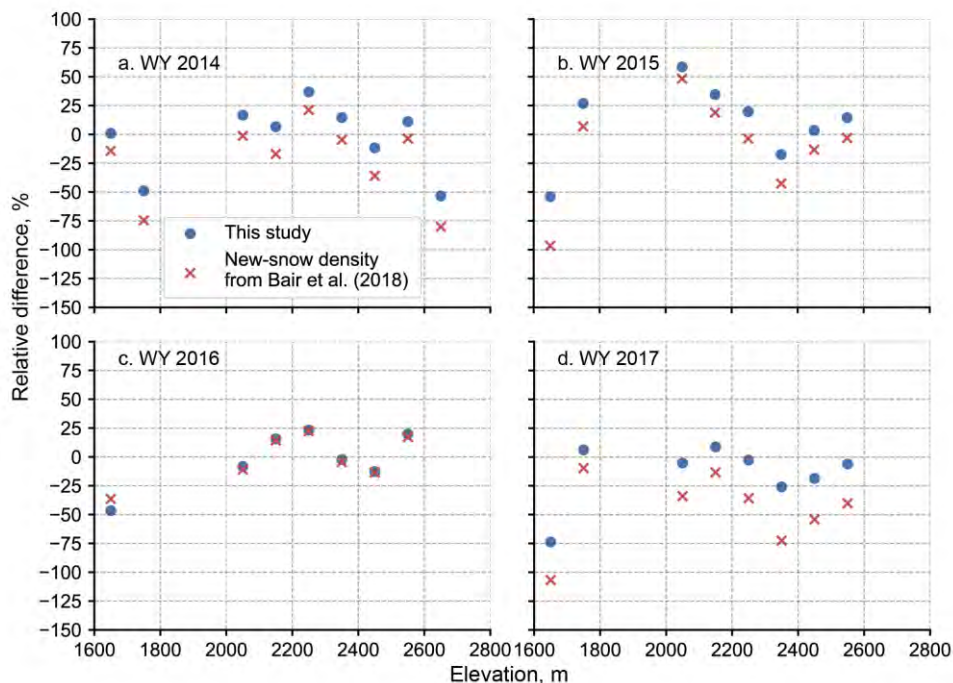

Figure S26. Relative difference of annual solid precipitation estimates from wireless sensors compared to those from snow pillows. Results using the new-snow density from this study versus Bair et al. (2018) are shown. a) WY2014, b) WY2015, c) WY2016, and d) WY2017. The relative differences of solid precipitation are plotted at 100-m elevation bands where both wireless sensors and pillows were presented. A positive difference means that sensor-network-based estimates are larger relative to those from snow pillows.
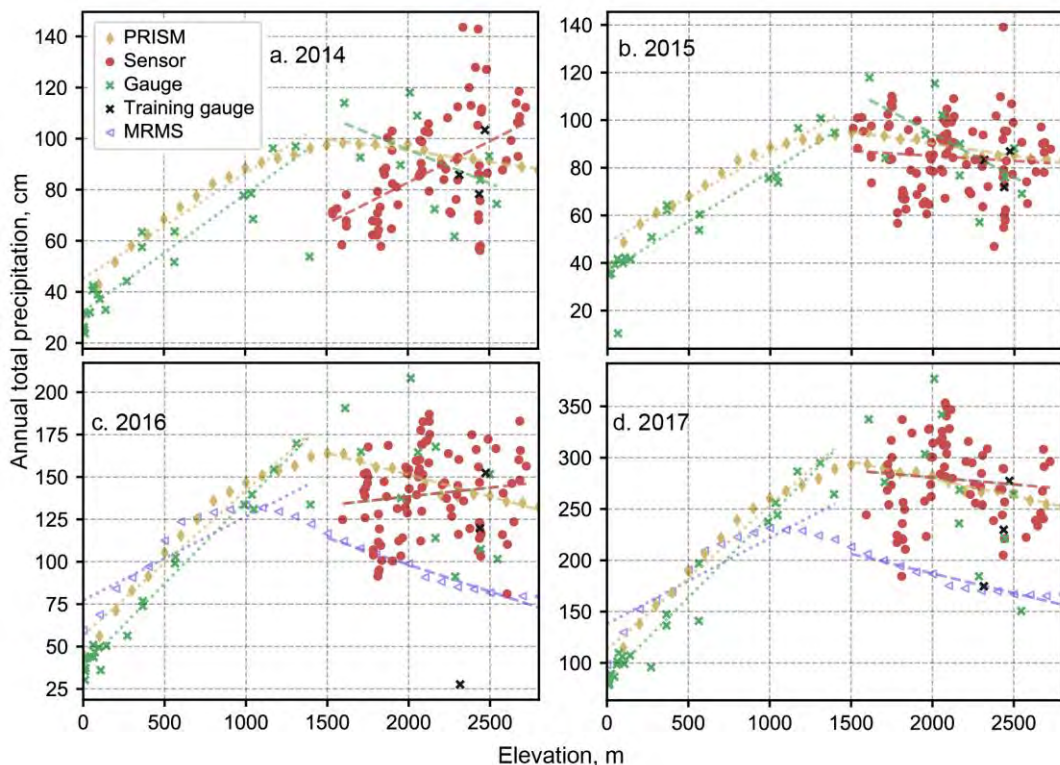
Figure S27. Similar to Figure 7, but the sensor-network and gauge data at OWC site are removed. Annual total precipitation estimates from the wireless-sensor network, precipitation gauges, and 100-m banded PRISM data: a) WY2014, b) WY2015, c) WY2016, and d) WY2017. Note that the vertical-axis scales of each panel are different. The colored, dashed lines are fitted lines using the Orographic Precipitation Gradients (OPGs) with the corresponding data in the same color, i.e. red, green, yellow, and blue lines are OPG lines for the wireless-sensor network, precipitation gauges, PRISM, and MRMS, respectively.
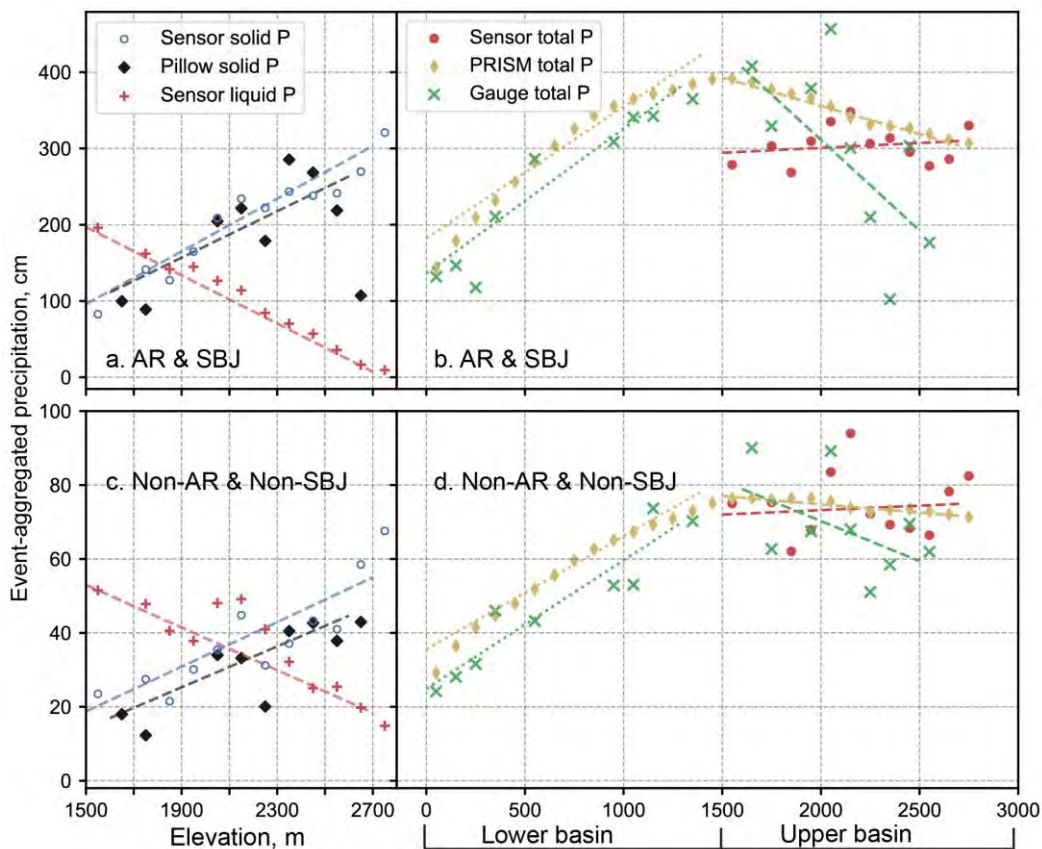

Figure S28. Similar to Figure 10, but the sensor-network and gauge data at OWC site are removed. Event-aggregated solid and total precipitation estimates for (a-b) events related to both Atmospheric River (AR) and Sierra Barrier Jet (SBJ) and (c-d) events that are not associated with either AR or SBJ (i.e. Non-AR & Non-SBJ). Left panels show solid precipitation from the wireless-sensor network and snow pillows; right panels show total precipitation from sensor nodes, precipitation gauges, and PRISM for the lower and upper basins. All data are averaged by 100-m elevation bands. The dashed lines are fitted lines using the Orographic Precipitation Gradients (OPGs) with the corresponding data in the same color.

44